University of Technology Sydney

Faculty of Science

Metal Oxide Nanostructures for Photoelectrochemical, Photocatalytic and Optoelectronic Applications

by **Amar SALIH**

Thesis submitted in fulfilment of the requirements for the degree of

Doctor of Philosophy

February 2025

Certificate of Original Authorship

I, Amar SALIH, declare that this thesis is submitted in fulfilment of the requirements for the award of Doctor of Philosophy, in the School of Mathematical and Physical Sciences at the University of Technology Sydney.

This thesis is wholly my own work unless otherwise referenced or acknowledged. In addition, I certify that all information sources and literature used are indicated in the thesis.

This document has not been submitted for qualifications at any other academic institution.

This research is supported by the Australian Government Research Training Program.

Signature: Production Note:
Signature removed prior
to publication.

Date: 28/02/2025

Thesis Including Published Works - General Declaration

Chapters 3 to **5** of this thesis consist of four published papers in peer-reviewed journals, in all of which I am the first author. My contributions to each paper have been detailed, and all co-authors have provided their signatures as consent for the inclusion of the published material in this thesis. The bibliographic details of each publication are provided below.

Paper 1: **Improved flux and anti-fouling performance of a photocatalytic ZnO membrane on porous stainless steel substrate for microalgae harvesting**. Salih, Amar K., et al. *Journal of Membrane Science* 718 (2025): 123700.

Contribution statement

My contributions to this work include fabricating the ZnO-coated stainless steel membranes, designing, testing and optimizing the filtration setup, collecting and analyzing microalgae filtration data, collecting and analyzing membranes characterization data, and writing the original manuscript.

Name of Author	Signature of Author	Date
Amar K Salih	Production Note: Signature removed prior to publication.	10/02/2025
Lisa Aditya	Production Note: Signature removed prior to publication.	10/01/2025
Fatima Matar	Production Note: Signature removed prior to publication.	06/01/2025
Long D Nghiem	Production Note: Signature removed prior to publication.	03/02/2025
Cuong Ton-That	Production Note: Signature removed prior to publication.	05/02/2025

Paper 2: **Photocatalytic Self-Cleansing ZnO-coated Ceramic Membranes for Preconcentrating Microalgae**. Salih, Amar K., et al. *Journal of Membrane Science* 694 (2024): 122405.

Contribution statement

My contributions to this work include fabricating the ZnO-coated alumina membranes, designing, testing and optimizing the filtration setup, cultivating the microalgae solution, collecting and analyzing microalgae filtration data, collecting and analyzing membrane characterization data, and writing the original draft.

Name of Author	Signature of Author	Date
Amar K Salih	Production Note: Signature removed prior to publication.	10/02/2025
Curtis P. Irvine	Production Note: Signature removed prior to publication.	07/01/2025
Fatima Matar	Production Note: Signature removed prior to publication.	06/01/2025
Lisa Aditya	Production Note: Signature removed prior to publication.	10/01/2025
Long D Nghiem	Production Note: Signature removed prior to publication.	03/02/2025
Cuong Ton-That	Production Note: Signature removed prior to publication.	05/02/2025

Paper 3: **Enhanced solar-driven water splitting performance using oxygen vacancy rich ZnO photoanodes**. Salih, Amar K., et al. *Solar Energy Materials and Solar Cells* 259 (2023): 112436.

Contribution statement

My contributions to this work include preparing the ZnO photoanode samples, performing and analyzing all the electrochemical experiments, performing and analyzing all the characterization data, and writing the original draft.

Name of Author	Signature of Author	Date
Amar K Salih	Production Note: Signature removed prior to publication.	10/02/2025
Matthew R Phillips	Production Note: Signature removed prior to publication.	03/02/2025
Cuong Ton-That	Production Note: Signature removed prior to publication.	05/02/2025

Paper 4: **Defect passivation and enhanced UV emission in β-Ga_2O_3 via remote fluorine plasma treatment**. Salih, Amar K., et al. *Applied Surface Science* 687 (2025): 162250.

Contribution statement

My contributions to this work include preparing the Ga_2O_3 nanowire samples, collecting and analyzing the structural and chemical characterization data, analyzing the cathodoluminescence data, and writing the original draft.

Name of Author	Signature of Author	Date
Amar K Salih	Production Note: Signature removed prior to publication.	10/02/2025
Saskia Fiedler	Production Note: Signature removed prior to publication.	11/02/2025
Curtis P. Irvine	Production Note: Signature removed prior to publication.	07/01/2025
Fatima Matar	Production Note: Signature removed prior to publication.	06/01/2025
Matthew R Phillips	Production Note: Signature removed prior to publication.	03/02/2025
Cuong Ton-That	Production Note: Signature removed prior to publication.	05/02/2025

Copyright notice

© Copyright by Amar SALIH 2025. All rights reserved

To M.

&

To all the good things that did not come to be

Acknowledgments

It has been years that brought their fair share of lessons, and along the way, there have been people whom I would like to acknowledge with heartfelt gratitude.

First and foremost, I would like to express my deepest appreciation to my supervisor, **A/Prof. Cuong Ton-That**, for his mentorship, guidance and support, for giving me a chance to work and collaborate with a profound scientist, for opening many opportunities, and for making burdens feel lighter throughout my PhD journey.

I am also grateful to **Prof. Long D. Nghiem** for opening a new research area for me and guiding me through it, for his generous support, and for welcoming me to his team at the Centre for Technology in Water and Wastewater (CTWW) lab at UTS.

My thanks also go to **EM/Prof. Matthew R. Phillips** for generously sharing his knowledge and providing invaluable support throughout this work. I would like to thank the School of Mathematical and Physical Sciences (MaPS) at UTS for offering the resources necessary for my PhD journey. I am thankful to UTS for the scholarships that funded my PhD study.

To my family and friends, I am deeply grateful for your persistent encouragement and firm support.

Contents

List of Figures

List of Tables

List of Abbreviations

AFM – Atomic Force Microscopy

ALD – Atomic Layer Deposition

AOP – Advanced Oxidation Process

BL – Blue Luminescence

CB – Conduction Band

CL – Cathodoluminescence

CVD – Chemical Vapor Deposition

DAP – Donor-Acceptor Pairs

DLE – Deep-Level Emission

DUV – Deep-Ultraviolet

EDS – Energy Dispersive Spectrometer

EDX – Energy Dispersive X-ray

EIS – Electrochemical Impedance Spectroscopy

FRR – Flux Recovery Rate

FTO – Fluorine Tin Oxide

FWHM – Full Width Half Maximum

GL – Green Luminescence

HER – Hydrogen Evolution Reaction

ICP – Inductively Coupled Plasma

ITO – Indium Tin Oxide

LED – Light Emitting Diode

LSV – Linear Sweep Voltammetry

MF – Microfiltration

NBE – Near Band Edge

NW – Nanowire

OER – Oxygen Evolution Reaction

PEC – Photoelectrochemical Cell

PLD – Pulsed Laser Deposition

PVD – Physical Vapor Deposition

RHE – Reversible Hydrogen Electrode

RL – Red Luminescence

ROS – Reactive Oxygen Species

SCE – Saturated Calomel Electrode

SEM – Scanning Electron Microscope

SST – Stainless Steel

STH – Self-Trapped Holes

TMP – Transmembrane Pressure

UF – Ultrafiltration

VB – Valence Band

VLS – Vapor–Liquid–Solid

XPS – X-Ray Photoemission Spectroscopy

XRD – X-ray Diffraction

Abstract

The urgent need for sustainable technological solutions to environmental and energy challenges is driving extensive research into innovative nanomaterials. This work investigates the synthesis, modification, and application of metal oxide nanostructures in sustainable green technologies such as microalgae biomass harvesting for fuel production, hydrogen evolution, and enhancement of the electronic properties of environmental optoelectronic devices.

In this work, photocatalytic ZnO-coated membranes are developed for microalgae harvesting from a pre-concentrating solution. The fabrication involves ZnO deposition via reactive magnetron sputtering onto two types of membrane substrates: porous stainless-steel and alumina membranes. The deposition produces crystalline, hydrophilic ZnO coatings on both membrane substrates. In the case of the stainless-steel substrate, the ZnO-coated membranes exhibit enhanced water permeability, achieving a two-fold increase in water flux after ZnO coating. Additionally, their photocatalytic cleaning properties enable 60% permeability recovery within 30 minutes of UV exposure after complete fouling. For alumina membranes, the ZnO coating significantly enhances membrane hydrophilicity, reducing water contact angles by approximately 50% and limiting flux decline to 5% over three filtration cycles, compared with 32% decline for uncoated membranes. Furthermore, 100% flux recovery is achieved within 30 minutes of exposure to a solar simulator. These studies demonstrate that incorporating ZnO coatings into membrane filtration systems offers a robust, cost-effective solution for microalgae harvesting processes.

For hydrogen evolution, a novel method is developed to fabricate high-performance ZnO photoanodes for PEC water splitting. The post-growth oxidation of metallic Zn films produces a randomly oriented, nanorod-like ZnO film enriched with oxygen vacancies. Characterization via cathodoluminescence (CL) spectroscopy, X-ray photoemission spectroscopy (XPS), and

electrochemical analysis reveals the role of oxygen vacancies in enhancing PEC performance by improving light absorption and charge transfer. These photoanodes achieve a remarkable photocurrent density of 1.14 mA/cm^2 at 1.23 V_{RHE} under simulated sunlight, representing one of the highest performances reported for ZnO-based electrodes.

Finally, the thesis investigates the incorporation of fluorene (F) donors in β-Ga_2O_3 nanowires (NWs) and their effects on luminescence, defect structure, and carrier dynamics. F doping is achieved using remote SF_6 plasma treatment, which introduces F atoms at oxygen sites while preserving the monoclinic crystal structure. CL mapping and time-resolved spectroscopy reveal the emergence of an additional UV emission peak, attributed to shallow F donor–deep acceptor pair recombination, accompanied by the suppression of visible defect-related emissions. F doping also increases the carrier lifetime from 9.2 ns to 17.0 ns, demonstrating the role of F dopants in passivating intrinsic point defects and enhancing the optical properties of β-Ga_2O_3 for deep UV optoelectronic applications.

Chapter 1. Introduction and thesis overview

Metal oxides play a crucial role in advancing green environmental technologies, mainly due to their unique electronic and optical properties [1, 2]. These materials exhibit a wide range of semiconducting behaviors that enable their interaction with light, governed by their respective bandgaps. Semiconductor oxides, such as titanium oxide (TiO_2), tungsten oxide (WO_3), zinc oxide (ZnO), and gallium oxide (Ga_2O_3), offer distinctive advantages due to their exceptional chemical stability, high breakdown electric field and high electron mobility [3]. These properties make them highly suitable for applications in environmental technologies.

ZnO is a wide bandgap semiconductor with a bandgap of 3.4 eV [4]. It is known for its high conductivity, and biocompatibility, which makes it essential in a wide range of applications, including photocatalytic electrodes for water splitting, photodegradation, solar cells, thin-film transistors and piezoelectric devices [4, 5]. Similarly, monoclinic β-Ga_2O_3, an emerging ultra-wide bandgap semiconductor with a bandgap of 4.9 eV, exhibits an exceptionally high breakdown field of 8 MV/cm. In addition, β- Ga_2O_3 demonstrates high electron mobility, and excellent chemical and thermal stability [6]. These characteristics make it a strong candidate for developing next-generation power electronic devices including solar-blind photodetectors, field-effect transistors and deep UV emitters [6-8].

This thesis aims to explore the potential applications of ZnO and β-Ga_2O_3 in addressing challenges associated with microalgae biomass harvesting for fuel production, hydrogen evolution, and enhancement of the electronic properties of environmental optoelectronic devices. Each chapter investigates the fabrication, characterization, and application of these materials, providing insights into their electronic structure, morphology, chemical composition, and optical properties. The findings highlight the significant potential of ZnO and β-Ga_2O_3 to drive innovations in green and sustainable environmental applications. The structure of this thesis is organized as follows:

Chapter 1. Introduction and thesis overview: This chapter provides a general overview of the research scope and the structure of this thesis.

Chapter 2. Literature review: This chapter focuses on the applications of metal oxides in environmental technologies. It highlights the photodegradation properties of ZnO in antifouling and self-cleaning membranes, its role as a photoanode for hydrogen evolution through photoelectrochemical cell (PEC), and the utilization of Ga_2O_3 nanostructures in optoelectronic devices.

Chapter 3. Photocatalytic oxide-based membranes for microalgae harvesting: This chapter investigates the photocatalytic degradation performance of ZnO coatings integrated with two types of membranes, stainless steel and ceramic, and their application in microalgae biomass harvesting. The outcome of this chapter is published in “Improved flux and anti-fouling performance of a photocatalytic ZnO membrane on porous stainless steel substrate for microalgae harvesting. Salih, Amar K., et al. *Journal of Membrane Science* 718 (2025): 123700.” and “Photocatalytic Self-Cleansing ZnO-coated Ceramic Membranes for Preconcentrating Microalgae. Salih, Amar K., et al. *Journal of Membrane Science* 694 (2024): 122405”

Chapter 4. Enhanced solar-driven water splitting performance using oxygen vacancy rich ZnO photoanodes: This chapter introduces a straightforward and economical approach for fabricating ZnO photoanodes enriched with oxygen vacancies (V_O) for enhanced solar-driven hydrogen evolution via PEC water splitting. The outcome of this work is published in “Enhanced solar-driven water splitting performance using oxygen vacancy rich ZnO photoanodes. Salih, Amar K., et al. *Solar Energy Materials and Solar Cells* 259 (2023): 112436"

Chapter 5. Defect passivation and enhanced UV emission in β-Ga_2O_3 via remote fluorine plasma treatment: This chapter investigates the impact of fluorine doping, achieved via SF_6 plasma treatment, on native defects in β-Ga_2O_3 nanowires, and its role in improving the electronic and optical properties of Ga_2O_3 crystals. The outcome of this chapter is published in "Defect passivation and enhanced UV emission in β-Ga_2O_3 via remote fluorine plasma treatment. Salih, Amar K., et al. *Applied Surface Science* 687 (2025): 162250"

Chapter 6. Conclusion: This chapter summarizes the key findings from all the studies presented in this thesis and offers recommendations for future research to further enhance the material performance and address remaining challenges.

1.2. References

[1] M. Ikram, M. Rashid, A. Haider, S. Naz, J. Haider, A. Raza, M. Ansar, M.K. Uddin, N.M. Ali, S.S. Ahmed, A review of photocatalytic characterization, and environmental cleaning, of metal oxide nanostructured materials, Sustainable Materials and Technologies 30 (2021) e00343.

[2] B. Alhalaili, R.J. Bunk, H. Mao, H. Cansizoglu, R. Vidu, J. Woodall, M.S. Islam, Gallium oxide nanowires for UV detection with enhanced growth and material properties, Scientific reports 10 (2020) 21434.

[3] J. Shi, J. Zhang, L. Yang, M. Qu, D.C. Qi, K.H. Zhang, Wide bandgap oxide semiconductors: from materials physics to optoelectronic devices, Advanced materials 33 (2021) 2006230.

[4] A. Janotti, C.G. Van de Walle, Fundamentals of zinc oxide as a semiconductor, Reports on progress in physics 72 (2009) 126501.

[5] K.M. Lee, C.W. Lai, K.S. Ngai, J.C. Juan, Recent developments of zinc oxide based photocatalyst in water treatment technology: a review, Water research 88 (2016) 428-448.

[6] D. Guo, Q. Guo, Z. Chen, Z. Wu, P. Li, W. Tang, Review of Ga_2O_3-based optoelectronic devices, Materials Today Physics 11 (2019) 100157.

[7] R. Singh, T. Lenka, D. Panda, R. Velpula, B. Jain, H. Bui, H. Nguyen, The dawn of Ga_2O_3 HEMTs for high power electronics-A review, Materials Science in Semiconductor Processing 119 (2020) 105216.

[8] S. Pearton, J. Yang, P.H. Cary, F. Ren, J. Kim, M.J. Tadjer, M.A. Mastro, A review of Ga_2O_3 materials, processing, and devices, Applied Physics Reviews 5 (2018) e00343.

Chapter 2. Literature review

Metal oxides play a key role in environmental remediation through various applications, including photocatalytic pollution degradation and green fuel production [1]. Their functional properties are highly diverse and strongly influenced by factors such as crystal structure, morphology, composition, intrinsic defects, and doping. These factors collectively determine their optical, electrical, chemical, and catalytic properties [2].

2.1. Metal oxides for photocatalytic degradation

Metal oxides such as TiO_2, ZnO, Fe_2O_3, WO_3 have been investigated as effective photocatalysts for degrading organic pollutants in water and air. When exposed to light with energy exceeding their bandgap, electron-hole pairs are generated, which can trigger the formation of reactive oxygen species (ROS) such as hydroxyl radicals (•OH) and superoxide anions ($•O_2^-$) [3]. These ROS oxidize complex organic pollutants into simpler compounds or mineralize them into CO_2 and H_2O [4], as illustrated in Fig.2.1.

[Production note: This figure is not included in this digital copy due to copyright restrictions.]

Figure 2.1. Metal oxide photocatalysts for organic pollutant degradation. This figure is taken from [5].

A major advantage of metal oxide-based photocatalysts is their ability to target a wide spectrum of pollutants, including synthetic dyes [6], antibiotics [7], hydrocarbons [8], nitroaromatic compounds and refinery oils [9] due to their low valence band position, which increases the oxidation potential of ROS. These pollutants pose serious environmental risks due to their toxicity, persistence, and potential to bioaccumulate. The effectiveness of these photocatalysts can be further enhanced through modifications such as introducing mid-gap electronic states or doping with metal or non-metal elements, which improve light absorption into the visible spectrum and suppress electron-hole recombination [10]. Additionally, factors like pH, pollutant concentration, catalyst loading, and light intensity are crucial in optimizing degradation efficiency [11].

2.1.1. ZnO for photocatalytic degradation

ZnO is a widely studied semiconductor for pollutant degradation via photocatalysis, owing to its outstanding optical, electronic, and catalytic properties, alongside its resistance to fouling and bacterial growth [12]. ZnO also offers advantages, including broader solar spectrum absorption and lower production costs, approximately 75% cheaper than Al_2O_3 and TiO_2 [13]. Moreover, ZnO has proven to be a competitive alternative to TiO_2 for wastewater treatment, showing superior photocatalytic activity, especially in degrading dye pollutants [14, 15]. Additionally, ZnO possesses electron mobility two orders of magnitude higher than TiO_2, allowing for more efficient charge transport. Its tunable film structures enable control over nanostructure size and morphology, while its intrinsic high oxygen vacancy density further enhances photocatalytic efficiency by promoting hydroxyl ion generation and accelerating reaction kinetics [16]. These properties make ZnO a promising alternative to TiO_2 for wastewater treatment and other environmental applications.

The degradation process begins with pollutant adsorption on the ZnO surface, followed by oxidation-reduction reactions and the subsequent desorption of reaction products. When ZnO is illuminated with light energy equal to or greater than its band gap, electrons are excited from the valence band to the conduction band, creating electron-hole pairs that migrate to the surface to drive redox reactions. Scavengers like oxygen and hydroperoxyl radicals inhibit recombination, enabling conduction band electrons to react with oxygen to produce superoxide ($O_2^{\cdot -}$), hydroperoxyl ($HO_2^{\cdot}$), and eventually hydroxyl ($\cdot OH$) radicals via a series of reactions, Eqs. (2.1 – 2.7) [17]:

$$ZnO + hv \rightarrow e^- + h^+ \tag{2.1}$$

$$O_2 + e^- \rightarrow O_2^{\cdot -} \tag{2.2}$$

$$O_2^{\cdot -} + H^+ \rightarrow HO_2^{\cdot} \tag{2.3}$$

$$2HO_2^{\cdot} \rightarrow H_2O_2 + O_2 \tag{2.4}$$

$$H_2O_2 + O_2^{\cdot -} \rightarrow \cdot OH + OH^- + O_2 \tag{2.5}$$

$$H_2O_2 + hv \rightarrow 2 \cdot OH \tag{2.6}$$

$$H_2O_2 + e^- \rightarrow \cdot OH + OH^- \tag{2.7}$$

In the valence band, holes react with water and hydroxyl ions to generate additional hydroxyl radicals, Eqs. (2.8 – 2.9) [17]:

$$H_2O + h^+ \rightarrow \cdot OH + H^+ \tag{2.8}$$

$$OH^- + h^+ \rightarrow \cdot OH \tag{2.9}$$

These hydroxyl radicals are potent oxidizing agents that degrade pollutants into intermediates, which are further mineralized into harmless end products such as water and carbon dioxide, Eq. (2.10) [17]:

$$\cdot OH + Pollutant \rightarrow Intermediates \rightarrow CO_2 + H_2O \tag{2.10}$$

This series of reactions highlights the efficiency of ZnO in transforming contaminants into non-toxic substances under photocatalytic conditions. Figure 2.2 summarized the proposed photocatalytic degradation reactions.

[Production note: This figure is not included in this digital copy due to copyright restrictions.]

Figure 2.2. Schematic diagram illustrating the photoactivation process in metal oxides and the primary surface reactions involved in photocatalytic degradation. This figure is adapted from [17].

While ZnO is a powerful photocatalyst, it faces several limitations that hinder its practical applications. A primary challenge is the rapid recombination of photogenerated electron-hole pairs [18], which reduces quantum efficiency by releasing energy as heat. Additionally, ZnO's wide band gap restricts its light absorption to the UV region, making it inefficient under visible light [18]. The tendency of ZnO nanoparticles to aggregate further diminishes their photocatalytic efficiency by reducing the available surface area for light exposure and active site generation [19]. This aggregation can also lead to shielding effects that lower the photon flux in slurry systems and encourage the recombination of charge carriers. Additionally, prolonged UV exposure induces photo-corrosion, leading to ZnO dissolution and reduced photoactivity and stability, with reusability compromized under extreme pH conditions [18]. These limitations necessitate modifications to enhance ZnO's photocatalytic properties, such as reducing recombination rates, extending light absorption into the visible spectrum, and improving the stability and recovery of the photocatalyst.

Immobilizing ZnO on substrates such as clay, glass, silica, polymeric, or ceramic porous materials, Fig. 2.3, offers a promising solution. Ideal supports provide high surface area, strong catalyst adherence, effective pollutant adsorption, and maintain reactivity, thereby reducing agglomeration, enhancing contact time, and preventing catalyst loss in water treatment applications [20-23].

[Production note: This figure is not included in this digital copy due to copyright restrictions.]

Figure 2.3. Immobilization of ZnO-based photocatalyst on various supporting substrates. This figure is taken from [24].

2.1.2. ZnO based membranes for waste-water treatment

Membranes for water treatment are semipermeable barriers (porous materials) designed to selectively remove contaminants, such as dissolved salts, microorganisms, organic compounds, and suspended solids, from water. These membranes operate through physical, chemical, or pressure-driven processes, including microfiltration (MF), ultrafiltration (UF), nanofiltration (NF), and reverse osmosis (RO), to produce water suitable for drinking, industrial use, or environmental discharge [25]. ZnO-based membranes, incorporating ZnO nanoparticles or nanostructured thin-film coatings, are developed to enhance water treatment performance. These membranes function by reducing nanoparticle agglomeration, increasing pollutant contact time, and preventing catalyst loss. Incorporating ZnO into membrane systems offers key advantages, such as enhanced hydrophilicity, improved resistance to fouling, and higher efficiency in contaminant removal [23].

2.1.2.1. ZnO-based polymeric membranes

Polymeric membranes with embedded ZnO nanostructures enhance membrane performance by addressing fouling, durability, and permeability issues. ZnO improves hydrophilicity, UV resistance, and antimicrobial activity, thereby extending membrane lifespan [26]. The integration of ZnO into polymeric membranes is typically achieved using two main approaches: blending and surface coating. In the blending method, ZnO nanoparticles are mixed with polymers such as polyvinylidene fluoride (PVDF) to ensures the uniform dispersion of ZnO throughout the membrane matrix, reducing the risk of blockages in surface pores compared to coated membranes [27]. In contrast, surface coating involves applying ZnO onto pre-formed membranes, which modifies surface characteristics without altering the bulk properties [26]. This method mainly enhances the hydrophilicity of the membrane surface and reduces the adhesion of foulants, which results in a significant increase in the permeate water flux compared to the ZnO-based membrane prepared by blending method [28, 29]. Figure 2.4 displays examples of ZnO-based polymer membrane preparation by blending and surface coating. Although ZnO-based polymer membranes offer enhanced hydrophilicity, low fabrication cost and greater flexibility for surface and bulk modification, they suffer from lower thermal and chemical stability, and reduced mechanical strength compared to ceramic-based membranes [30].

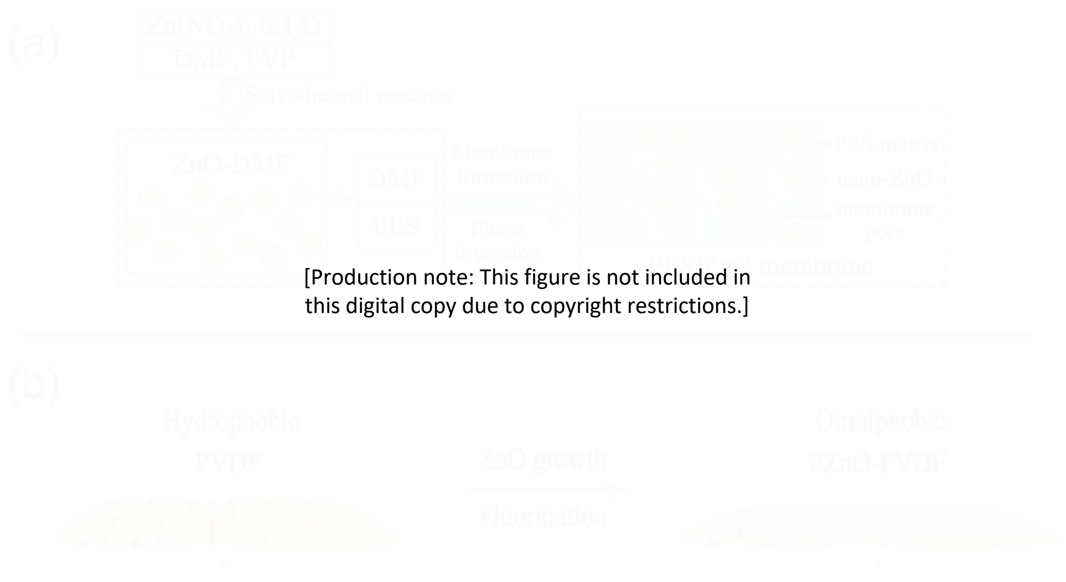

[Production note: This figure is not included in this digital copy due to copyright restrictions.]

Figure 2.4. Schematic illustration of ZnO-based polymer membrane fabrication via (a) blending and (b) surface coating. This figure is adapted from [27, 31].

2.1.2.2. ZnO-based ceramic membranes

Ceramic membranes with ZnO deliver exceptional performance for high thermal and chemical stability applications, such as treating industrial effluents and high-temperature processes [32]. Compared to polymeric membranes, ceramic membranes, such as TiO_2, Al_2O_3 and SiO_2 are more resistant to chemical degradation and mechanical stress, making them ideal for harsh environments [32, 33]. While ceramic membranes offer superior durability, chemical stability, and high-temperature resistance compared to polymeric alternatives, their production is energy-intensive, relies on expensive raw materials, and their brittle nature increases the risk of mechanical failure under stress, all of which contribute to higher overall operational costs [34]. Efforts are ongoing to reduce manufacturing expenses and develop cost-effective ceramic materials. Some of the common methods for preparation of ZnO-containing ceramic membranes involves immersing ceramic supports into ZnO precursor solutions (such as zinc(II) nitrate), sol–gel, atomic layer deposition (ALD), slip-casting, and chemical vapour deposition (CVD) [35-37]. These techniques produce films with compact structures and controlled thickness, ensuring stability and durability under harsh conditions. Figure 2.5 shows an SEM images of the ZnO-based membrane deposited on alumina membrane.

[Production note: This figure is not included in this digital copy due to copyright restrictions.]

Figure 2.5. SEM images: (a) cross-sectional view and (b) surface view of the ZnO-based membrane deposited on a 200-nm pore-sized alumina membrane. This figure is taken from [37].

2.1.3. Purification of Water Contaminants Using ZnO Photocatalysts

ZnO is an efficient photocatalyst for water purification, degrading various pollutants via reactive oxygen species (ROS) generated under light. Its versatility spans multiple contaminant classes. For example, dyes used in the textile industry significantly contribute to environmental pollution due to their synthetic, non-biodegradable nature, which stems from complex aromatic structures [38]. Their persistence in water systems poses carcinogenic and mutagenic risks to humans and aquatic organisms [39]. For example, Yulizar et al. [40] reported 91% removal of malachite green (MG) within two hours under visible light. ZnO nanomaterials have also been effective against a wide range of dyes, including methylene blue, methyl orange, and reactive dyes, and have shown promise in treating dye mixtures in real wastewater applications [41, 42].

The presence of pharmaceutical endocrine-disrupting compounds (EDCs) in water has raised significant concern due to their ability to interfere with hormonal functions in humans and other organisms, causing adverse health effects [43]. ZnO based photocatalysts utilized ROS to completely mineralized the EDCs into carbon dioxide and water. For instance, Selvakumar et al. [44] demonstrated the effectiveness of a Gd_2WO_6-loaded ZnO/bentonite nanocomposite, achieving 97.9% degradation of ciprofloxacin within 60 minutes under visible light.

Agriculture plays a pivotal role in meeting the global demand for food, but the extensive use of agrochemicals, particularly pesticides, has led to serious environmental challenges. These chemicals are persistent, bio-accumulative, and pose significant risks to ecosystems and human health [45]. Photocatalysis has emerged as an efficient and sustainable technology, capable of transforming these toxic compounds into harmless substances through advanced oxidation processes. For instance, Yadav et al. [46] demonstrated the successful degradation of the herbicide triclopyr using ZnO/SnO_2 nanocomposites.

The removal of heavy metals from water is a critical environmental challenge due to their extreme toxicity and persistence even at trace levels. Heavy metals such as cadmium, arsenic, lead, mercury, and chromium are commonly found in industrial wastewater and surface water, primarily due to industrial discharges and anthropogenic activities like fossil fuel combustion [47]. Their toxicity is associated with severe health risks, including chronic fatigue, gastrointestinal disorders, mental impairments, and degenerative diseases [47]. Traditional methods such as ion exchange and adsorption are limited as they only transfer contaminants between phases without eliminating their toxicity [48]. ZnO-based photocatalysts are used to convert heavy metals into less harmful states or reducing them to their elemental forms. For instance, Bao et al. [49] reported the successful reduction of toxic $Cr_{(VI)}$ to the less harmful $Cr_{(III)}$ using surface-hybridized PANI/ZnO nanosheets under UV light. The hybrid material's enhanced photocatalytic performance was attributed to efficient charge separation and the interaction of ZnO's hydroxyl groups with PANI's amine groups. Le et al. [50] compared heavy metal ion removal efficiencies using ZnO under UV and visible light. ZnO particles effectively removed $Cu_{(II)}$, $Pb_{(II)}$, and $Cr_{(VI)}$ ions, achieving 100%, ~60%, and ~40% removal, respectively, under visible light, but showed lower efficiency for $Cd_{(II)}$, $Mn_{(II)}$, and $Ni_{(II)}$.

Petroleum refinery wastewater (PRW) is also a major environmental concern due to its complex composition, including aliphatic and aromatic hydrocarbons, halogenated aromatic substances, and ammonia, which contribute significantly to ammonia nitrogen levels and chemical oxygen demand (COD), making PRW harmful to humans and ecosystems [51, 52]. ZnO-based photocatalysts has been successfully integrated into combined systems to enhance PRW remediation. Keramati and Ayati [53] demonstrated a combined electrocoagulation and photocatalytic process using ZnO nanoparticles immobilized on a concrete surface. This approach optimized both processes, reducing COD by 95.8% after 180 minutes.

Microalgae have emerged as a promising feedstock for bioenergy production, offering solutions for sustainable energy development [54]. These microorganisms, which include both eukaryotic and prokaryotic species, offer diverse advantages, such as nutrient recycling, wastewater treatment, and applications in biotechnology and economic sectors [55]. Additionally, microalgae produce high-value bioproducts (e.g., biodiesel, bioethanol, biogas, biohydrogen) and can absorb nitrogen and phosphorus from wastewater while reducing atmospheric carbon dioxide levels from industrial emissions [56]. Their rapid growth and high lipid content position them as a viable alternative to conventional energy crops and fossil fuels. Figure 2.6 summarizes the use of microalgae biomass in several environmental and sustainable energy applications.

[Production note: This figure is not included in this digital copy due to copyright restrictions.]

Figure 2.6. Application of microalgae feedstock in environmental, medical, and energy applications. This figure is taken from [57].

The efficient harvesting of microalgal biomass remains a critical bottleneck due to the small cell size (a few micrometers) and the dilute nature of cultures, typically below 1 g/L [58]. Conventional methods such as coagulation, flocculation, flotation, and centrifugation are widely used to concentrate biomass [59-61]. However, these techniques often require high energy inputs or substantial chemical usage, leading to significant operational costs. Dewatering alone accounts for 90% of equipment expenses and 20–30% of total production costs [62], posing a major obstacle to large-scale commercialization. On the other hand, membrane filtration has gained increasing attention for microalgal harvesting due to its high performance, scalability, and energy efficiency, as well as the elimination of chemical additives [63]. Compared to centrifugation, flotation, and flocculation, membrane-based separations offer distinct advantages, including ease of operation and the potential to streamline downstream processes such as lipid, protein, and carbohydrate extraction [55, 64]. The absence of chemical inputs simplifies subsequent processes such as refining and conversion while allowing the effective utilization of residual biomass [64].

2.2. Metal Oxides for Photoelectrochemical Water Splitting

The quest for clean and sustainable energy sources has driven extensive research into alternative energy technologies to address the ever-increasing global energy demand and mitigate the impacts of climate change. Among these, hydrogen stands out as a promising candidate due to its exceptional energy-to-mass efficiency (~ 140 MJ kg^{-1}) and its potential for zero-carbon energy production [65]. Hydrogen can be produced through various methods; however, generating hydrogen via PEC is regarded as one of the most environmentally friendly and economically viable approaches [66]. PEC cells utilize solar radiation to convert water into hydrogen and oxygen. A typical PEC consists of at least one photoelectrode designated for sunlight absorption and a metallic counter electrode, both connected by an external circuit and submerged in an electrolyte. Figure 2.7 depicts the fundamental components of a PEC system, where an n-type semiconductor serves as the photoanode for water oxidation and a metallic cathode facilitates water reduction.

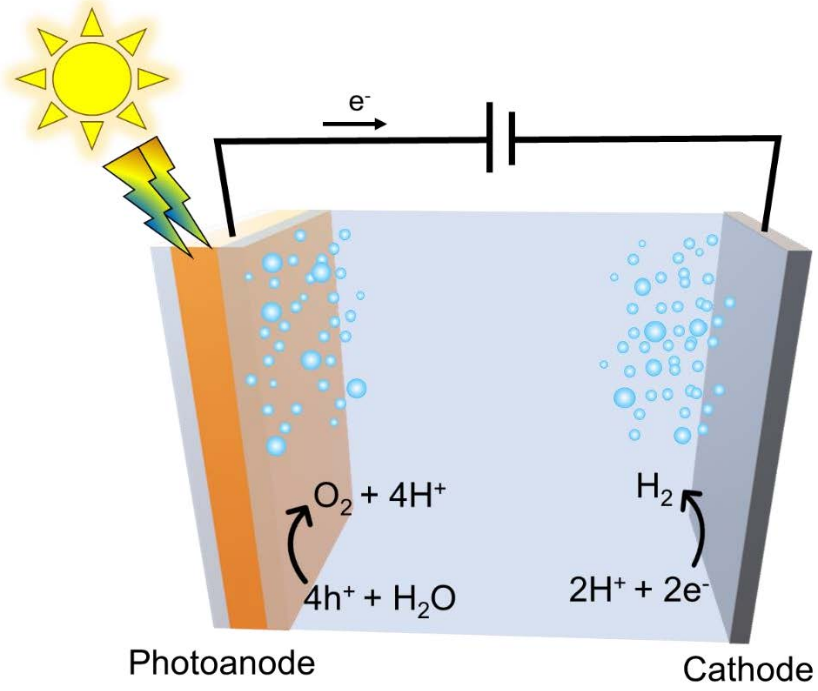

Figure 2.7. Schematic diagram illustrating the basic components of a PEC system for water splitting.

When exposed to sunlight, electrons in the semiconductor photoelectrode (photoanode) can be excited from the valence band (VB) to the conduction band (CB). Although a large portion of the photoinduced electron-hole pairs recombine almost immediately, some electrons successfully migrate to the cathode, where they participate in the reduction of water to generate hydrogen gas (H_2). Concurrently, photogenerated holes can travel to the photoanode surface, where they drive the oxidation of water into oxygen gas (O_2) [67]. The charge transfer at the interface between the photoelectrode and the electrolyte induces upward band bending [68]. This band bending is crucial as it enhances the separation of photoinduced electrons and holes, thereby mitigating their undesired recombination. This unique characteristic of band bending makes n-type semiconductors (with electrons as majority carriers) and p-type semiconductors (with holes as majority carriers) well-suited for use as photoanode and photocathode materials, respectively. The redox reactions occurring at each PEC electrode are described in the following equations [68]:

$$\text{Cathode: } 2H^{+} + 2e^{-} \rightarrow H_2 \qquad E^{o}_{red} = 0\ V \tag{2.11}$$

$$\text{Photoanode: } 2H_2O + 4h^{+} \rightarrow O_2 + 4H^{+} \quad E^{o}_{ox} = +1.23 \tag{2.12}$$

Where E^{o}_{red} and E^{o}_{ox} are the minimum energy required for water reduction and oxidation, respectively, relative to the normal hydrogen electrode (NHE). These equations indicate that a minimum voltage of 1.23 V is necessary for water splitting. Therefore, photoelectrodes must be capable of absorbing photons with an energy of at least 1.23 eV to meet this condition. Typically, the photon energy required exceeds this theoretical minimum due to various energy losses, such as voltage drops at electrode/wire interfaces. Consequently, selecting suitable semiconductor materials for light absorption is crucial for the development of efficient PEC systems for solar-driven water splitting [69].

The process of PEC water splitting consists of three main steps: light absorption, which affects the efficiency of sunlight utilization and the generation of electron-hole pairs; charge separation, where losses occur due to electron-hole recombination; and charge injection into the electrolyte to facilitate water oxidation or reduction [69]. For optimal performance, the photoelectrode's CB edge potential should be below the hydrogen evolution potential (0 V vs. NHE), and its VB edge above the oxygen evolution potential (1.23 V vs NHE) [68]. Additionally, photoelectrodes need to effectively absorb solar spectrum to produce significant numbers of photo-excited pairs, but materials with large band gaps, which might possess appropriate band edges, are less effective due to poor visible light absorption. Efficient charge transport and separation within the semiconductor are crucial to minimize recombination and enhance water splitting efficiency [70]. Finally, the chosen materials should be cost-effective and durable under the oxidative and reductive conditions of PEC operations [71].

As previously mentioned, the water-splitting process consists of two reactions: the hydrogen evolution reaction (HER), which occurs at the cathode, and the oxygen evolution reaction (OER), which takes place at the anode (photoanode) of the PEC. According to Equations (2.11) and (2.12), four equivalents of holes are required for each mole of O_2, making this half-reaction kinetically sluggish [72]. Consequently, oxygen evolution is often considered the kinetic bottleneck of the entire water-splitting process, and enhancing the kinetics of this reaction remains a significant challenge [72]. A range of metal oxides, including Fe_2O_3, CdO, TiO_2, WO_3, $BiVO_4$, and ZnO [73], have been explored as potential photoanodes for PEC water splitting due to their low production costs and superior stability in aqueous environments compared to conventional semiconductors. Despite these advantages, most metal oxide photoanodes have demonstrated limited suitability for PEC applications. For example, hematite (α-Fe_2O_3) suffers from inefficient charge separation within its surface depletion layer, primarily due to low hole drift mobility and short hole diffusion lengths [74]. CdO is considered unsuitable because of the high toxicity associated with cadmium [75], while TiO_2 exhibits poor solar radiation absorption and suboptimal hole transport properties resulting from its wide bandgap [75]. Figure 2.8 illustrates the bandgaps and band edge positions of common metal oxides relative to the redox potentials necessary for water splitting.

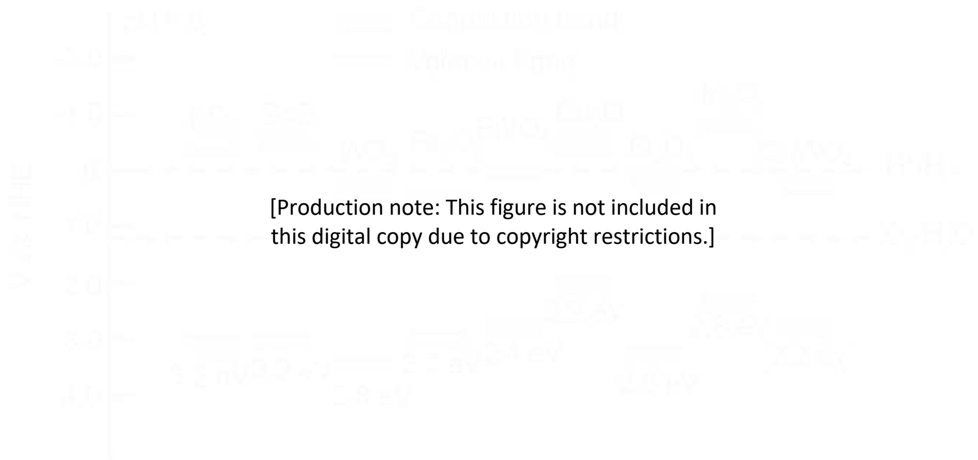

[Production note: This figure is not included in this digital copy due to copyright restrictions.]

Figure 2.8. Bandgaps and band-edge positions of common metal oxides relative to the redox potentials necessary for water splitting (pH 0) [76].

2.2.1. ZnO for Photoelectrochemical Water Splitting

ZnO is an n-type, direct wide-bandgap semiconductor with a bandgap energy of around 3.3 eV. Its CB is derived from the 4s state of Zn^{2+}, while the VB originates from the 2p orbital of O^{2-} [77]. ZnO exists in three crystal phases: hexagonal wurtzite, zinc blende, and the rare rock salt structure. Among these, the hexagonal wurtzite phase is the most stable and commonly observed [78] . Additionally, ZnO nanomaterials are abundant, eco-friendly, easy to synthesize, and exhibit high biocompatibility, making them ideal for several green technology applications [78]. ZnO is a promising photoanode material for PEC water splitting due to its unique properties, such as low reflectivity, which enhances light absorption, while its abundant surface states facilitate O_2 adsorption, aiding in the trapping of photogenerated holes. This process extends the lifetime of photogenerated electrons and improves the efficiency of electron-hole pair separation. Furthermore, its band structure imparts strong oxidation capabilities to photogenerated holes, ensuring high efficiency in PEC water-splitting [78].

However, ZnO exhibits limited visible light absorption due to its wide bandgap (~3.3 eV) [77]. To addresses this limitation and enhance its visible light response, various strategies have been employed, including bandgap modification through metal doping with elements like Co, Ag, Cr, Al, Ga, and Ni [79, 80]. Another approach involves introducing oxygen vacancies into the ZnO lattice. These intrinsic defects modify the bandgap, influence the surface chemical and electrical properties, and act as active sites for water oxidation [81].

2.2.2. Synthesis methods of nanostructured ZnO photoanodes

The synthesis of nanostructured ZnO for PEC applications involves diverse techniques, each imparting material properties that influence the performance of ZnO-based photoelectrodes. Commonly employed methods include chemical vapor deposition, hydrothermal, sol-gel, and sputtering deposition, each yielding ZnO photoanodes with specific structural and electronic advantages that can enhance PEC efficiency.

2.2.2.1. Chemical Vapor deposition

Chemical Vapor Deposition (CVD) is a versatile vapor-phase technique for synthesizing high-quality ZnO thin films. It employs gaseous precursors like zinc acetate or diethylzinc, with carrier gases such as nitrogen or oxygen. The chemical reactions on heated substrates produce ZnO films with precise control over thickness, uniformity, and crystal orientation [82]. Parameters such as precursor flow rates, temperature, and pressure are adjustable, enabling the production of films with high crystallinity and low defect density. Swathi et al. [83], for instance, applied CVD to fabricate ZnO nanorods on ITO substrates, achieving well-ordered, hexagonal-phase nanorods with excellent crystallinity and light absorption. The branched nanorods demonstrated high PEC photocurrent density, showcasing their suitability for PEC and energy storage technologies. Despite these advantages, CVD faces challenges such as high costs, slow deposition rates, and environmental concerns related to precursor gases [84]. These limitations highlight the need for more sustainable, efficient, and cost-effective alternatives to meet industrial demands for ZnO-based materials.

2.2.2.2. Hydrothermal

Hydrothermal synthesis is a solution-based technique using elevated temperature and pressure to fabricate ZnO nanostructures with varies morphologies, such as nanowires, nanorods, and nanosheets [85]. This process involves immersing substrates or precursor solutions in an autoclave containing aqueous zinc salts or complexes, where controlled temperature and pressure regulate nucleation and growth. As example, Worasawat et al [86]. developed ZnO nanorods using hydrothermal approach combined with dip-coating for seed layer formation and subsequent annealing. This method resulted in a controlled hexagonal ZnO nanorods by adjusting seed layer solvent concentrations and synthesis temperatures. However, hydrothermal synthesis is constrained by high-temperature and high-pressure conditions and extended reaction times [87], which limits is suitability for large scale production at industrial levels.

2.2.2.3. Sol-gel

The sol-gel method is a feasible technique for synthesizing ZnO photoanodes by dissolving precursors like zinc acetate or zinc nitrate in solvents such as ethanol or water [88]. The process involves hydrolysis and condensation reactions to form a gel-like intermediate, which undergoes thermal treatment to eliminate solvents and organics, resulting in formation of ZnO thin films. sol-gel fabrication method enables good control of ZnO structures such as nanospheres, nanorods, nanowires, or thin films with customized thickness and orientation, which affect the light absorption, charge separation, and transport properties of ZnO photoanodes [88]. Ghorbani et al. [89] employed sol-gel method to fabricate hierarchical porous ZnO films. By modifying parameters such as solvent type, sol concentration, and withdrawal speed, they achieved highly crystalline porous ZnO films with enhanced optical properties suitable for PEC applications. On the other hand, sol-gel method has also shown some chemical synthesis complexity and fabrication time demands [90], which lead to lower material quality and higher fabrication costs.

2.2.2.4. Sputtering

Sputtering is a physical vapor deposition technique used to fabricate high-quality ZnO thin films with precise thickness and uniformity [91]. The process involves bombarding a Zn or ZnO target with high-energy ions, ejecting atoms that deposit onto a substrate, allowing fine control over film properties. Sputtering techniques are categorized into Direct Current (DC) and Radio Frequency (RF) sputtering [92]. While DC sputtering is unsuitable for non-conductive targets due to charge build-up, RF sputtering overcomes this limitation by using an alternating voltage at 13.56 MHz, enabling the deposition of conductive, semi-conductive, and insulating coatings [92]. Compared to methods like chemical vapor deposition, sputtering offers advantages such as high reproducibility, stoichiometric compound deposition, strong film adhesion due to energetic atom deposition, and uniform thickness [93]. As example, Cruz et al. [94] demonstrated the effectiveness of ZnO thin films fabricated via RF sputtering for photocatalytic hydrogen production. In their study, annealing the ZnO films in air and nitrogen atmospheres led to variations in PEC activity due to differences in oxygen deficiencies, which acted as active sites for the reaction. Furthermore, they showed that controlling ZnO film thickness significantly affects conductivity and light absorption, directly influencing photocatalytic performance. However, sputtering deposition often falls short in creating the complex nanostructures necessary to enhance photoanode performance for PEC [95]. The lack of nanostructures in sputtered films can reduce surface area and light absorption efficiency, which are critical for efficient photoanodes. To address this limitation, researchers frequently modify sputtering parameters or integrate post-deposition treatments to induce nanostructure features and improve the material's photoelectrochemical properties [96].

2.2.3. Intrinsic defects in ZnO photoanodes

Non-stoichiometric ZnO exhibits structural imperfections, including vacancies such as missing Zn atom (V_{Zn}) or missing O atom (V_O), or additional atoms in interstitial lattice positions (O_i and Zn_i), or anti-sites where Zn and O atoms occupy each other's lattice sites (Zn_O and O_{Zn}). Among these, V_O and O_{Zn} are particularly significant due to their low formation energy, making them highly probable during ZnO synthesis process [97].

[Production note: This figure is not included in this digital copy due to copyright restrictions.]

Figure 2.9. Thermodynamic transition levels for native point defects in ZnO. This figure is reprinted from [98].

As shown in Fig. 2.9, Zn_i, Zn_O, and V_O exhibit donor-like behaviour, shifting the Fermi level toward the conduction band and enhancing n-type conductivity by introducing extra electrons. On the other hand, O_i, O_{Zn}, and O_{Zn} display acceptor-like characteristics, reducing electron availability and opposing n-type conductivity. These defects may exist independently or combine into defect complexes. Depending on their nature, they can either restore stoichiometry and electrical neutrality or increase defect density, affecting charge carrier dominance [98].

2.2.3.1. Oxygen Vacancies

Oxygen vacancies are the most energetically favourable donor-type defects in ZnO [99]. These vacancies exist in three charge states: the neutral vacancy (V_O^0), singly ionized vacancy (V_O^+), and doubly ionized vacancy (V_O^{+2}). Theoretical studies indicate that V_O^0 and V_O^{+2} are thermodynamically stable, whereas V_O^+ is unstable with an extremely short lifetime [100]. Consequently, V_O^+ formation requires highly metastable conditions. The charge state of oxygen vacancies depends on the Fermi level (E_F) position within the band gap. When E_F is near the conduction band, V_O^0 dominates. Conversely, when E_F is closer to the valence band, V_O^{+2} becomes predominant. Oxygen vacancies significantly influence ZnO's lattice structure and chemical bonding. For V_O^0, the four nearest Zn atoms shift inward by ~12% relative to the equilibrium Zn-O bond length. In contrast, the formation of V_O^{+2}causes lattice expansion, with the nearest Zn atoms displacing outward by ~23% [98], as shown in Fig. 2.10 below.

[Production note: This figure is not included in this digital copy due to copyright restrictions.]

Figure 2.10. Local atomic relaxations around oxygen vacancies exhibit distinct behaviours depending on the charge state: (a) In V_O^0, the four nearest Zn atoms are displaced inward by **12%** of the equilibrium Zn–O bond length. (b) In V_O^{+2}, the Zn atoms are displaced outward by **23%**. This figure is reprinted from [98].

Multiple physical and chemical methods have been used to fabricate ZnO with oxygen vacancies. For example, high-energy ball milling generates localized high temperatures (>1000 °C) through friction and collision, leading to the ejection of oxygen atoms from the ZnO lattice.

The concentration of V_O in this method can be tuned by controlling parameters such as milling time, temperature, and rotation speed [101]. Chemical reduction is another method for creating V_O [102]. In this approach, a reducing agent, which can be a gas-based agent such as H_2 or Ar/H_2 or a solution-based agent such as sodium borohydride ($NaBH_4$) [103], reacts chemically with the oxygen atoms from ZnO, resulting in the formation of V_O by extracting lattice oxygen. Another method involves growing ZnO in oxygen-deficient environments [104]. This technique is suitable for CVD and PVD fabrication methods, which allow fine control over the synthesis environment, such as regulating the oxygen partial pressure required for fabricating ZnO, or by introducing inert gases like Ar and N_2 as a post-treatment step, which facilitate the deoxidation process.

2.3. Gallium Oxide Synthesis, Properties and Applications

Gallium oxide (Ga_2O_3) is a semiconductor with an ultra-wide band gap of 4.8 eV, surpassing materials such as silicon (1.1 eV), silicon carbide (3.26 eV), and gallium nitride (3.4 eV). Its high electrical conductivity, attributed to intrinsic point defects, positions it as a superior material for low-resistance electrical contacts compared to GaN and SiC [105, 106]. Additionally, its classification as a Transparent Conductive Oxide (TCO) enhances its suitability for optoelectronic applications, particularly in solar cells.

Gallium, though discovered in the 19th century, gained significant attention in the 1960s for its various oxide structures, and by 2000, arc discharge methods were widely used to synthesize monoclinic β-Ga_2O_3 nanowires [107]. While silicon has dominated power electronics since the 1950s due to its abundance, its narrow band gap limits its use in high-voltage and high-power applications [108]. Materials such as SiC and GaN, with wider band gaps, have partially addressed these limitations; however, gallium oxide provides even greater potential due to its lower power losses [109]. The synthesis of gallium oxide nanostructures allows for further enhancement of its properties, making it essential to optimize fabrication methods. The structural and functional characteristics of the material are highly dependent on the techniques and parameters used during synthesis [110].

2.3.1. Gallium oxide crystal structures

Ga_2O_3 exhibits multiple polymorphic forms, including α-Ga_2O_3 (rhombohedral), β-Ga_2O_3 (monoclinic), γ-Ga_2O_3 (defective spinel), δ-Ga_2O_3 (cubic), and ε-Ga_2O_3 (orthorhombic) [111]. These polymorphs arise from variations in lattice parameters and atomic arrangements, with β-Ga_2O_3 being the most thermodynamically stable form. In contrast, α-Ga_2O_3 is metastable, and other phases typically transform to β-Ga_2O_3 at temperatures exceeding 600 °C [112]. High-pressure conditions can induce irreversible transformations, such as the conversion of β-Ga_2O_3 to α-Ga_2O_3, which becomes stable under such conditions. The ε-phase, known for its ferroelectric properties, transitions to β-Ga_2O_3 above 870 °C, offering potential for high-temperature and high-power applications [112]. Notably, γ-Ga_2O_3 demonstrates advantageous properties over β-Ga_2O_3 in certain contexts. García-Carrión et al. [113] observed that γ-Ga_2O_3 enhances the carrier lifetime of poly(3,4-ethylenedioxythiophene) polystyrene sulfonate (PEDOT:PSS) in hybrid solar cells. This phase also exhibits inter-band luminescence, a property absents in β-Ga_2O_3, enabling real-time monitoring of band gap variations under photon energy [113]. Such characteristics expand the scope of applications for gallium oxide in optoelectronics and photovoltaic devices. Figure 2.11 shows the transformations between the polymorphs of gallium oxide.

[Production note: This figure is not included in this digital copy due to copyright restrictions.]

Figure 2.11. Transformation conditions between different Ga_2O_3 crystal phases. This figure is reprinted from [114].

2.3.2. Gallium oxide crystal growth

Numerous techniques have been developed for the synthesis of Ga_2O_3, each offering specific advantages based on process requirements and material properties. For example, the sol-gel method is a straightforward and cost-effective approach that operates efficiently at low fabrication temperatures. This method involves preparing a gallium precursor solution (sol), depositing it onto a substrate via dip- or spin-coating, and subsequently curing through heat treatment [115]. Magnetron sputtering is another widely used technique for Ga_2O_3 thin film deposition, where noble gas ions bombard a Ga_2O_3 or Ga target material in a controlled chamber, releasing particles that deposit onto a substrate. This method offers precise control over deposition parameters, enabling efficient material synthesis [116]. Moreover, CVD is an adaptable method that facilitates controlled deposition of Ga_2O_3 thin films in a vacuum environment. In particular, Metallo-organic CVD (MOCVD) is particularly effective for gallium oxide, as it provides precise control over growth parameters, enabling the formation of high-quality Ga_2O_3 nanostructures [117]. Pulsed Laser Deposition (PLD) is another efficient technique for synthesizing Ga_2O_3 thin films. In this method, a high-energy laser ablates the gallium based target material, and the ejected particles deposit onto a substrate within a gas-filled chamber [118]. Molecular Beam Epitaxy (MBE) is a high-precision technique commonly employed for producing high-quality Ga_2O_3 films. This process involves heating metal sources in effusion cells under ultra-high vacuum, allowing atom-by-atom deposition onto a substrate. Surface morphology is monitored in real-time using Reflection High-Energy Electron Diffraction (RHEED). While MBE delivers superior film quality, its high cost and complexity make it a resource-intensive process [119].

2.3.3. Defects in Gallium oxide

Despite advancements in fabrication techniques, Ga_2O_3 invariably contains defects, including vacancies and deep-level imperfections, which profoundly influence its material properties and device performance [120]. These defects act as scattering centres, reducing carrier mobility and degrading device output and responsiveness [120]. Additionally, they serve as trapping centres, compromising photodetector sensitivity [121]. Surface and interface defects further exacerbate device instabilities, contributing to threshold voltage shifts, reduced channel mobility, and diminished reliability. Hence, a detailed understanding of vacancies, interstitials, and related defects in β-Ga_2O_3 is critical. Metal oxides are typically insulators when they maintain a stoichiometric ratio, but their growth is highly influenced by the surrounding atmospheric composition. Deviations in the number of oxygen atoms lead to oxygen vacancies (V_o) or interstitial oxygen atoms (O_i). These defects act as donors or acceptors, respectively, altering the material's conductivity in response to oxygen levels at room temperature [122]. Other defects such as gallium vacancies (V_{Ga}) or interstitial gallium atoms (Ga_i) and complex defects can also form depending on growth conditions, such as oxygen- or gallium-rich environments

[123]. Controlling doping in β-Ga_2O_3 is challenging due to issues like self-compensation and defect formation, particularly point defects [124]. Luminescence studies have provided insight into defect-related mechanisms, as the light-emitting properties of β-Ga_2O_3 are closely linked to the behaviour of intrinsic and extrinsic defects [124]. Research shows that β-Ga_2O_3 lacks emission peaks near its band edge but exhibits luminescence in the ultraviolet (UVL, 3.2–3.6 eV), blue (BL, 2.8–3.0 eV), and green (GL, 2.4 eV) regions [124]. As illustrated in Fig. 2.12, these emissions arise from different mechanisms. The UVL band is attributed to recombination between electrons and holes, the BL band to self-trapped holes (STH) or electrons associated with oxygen vacancies, and the GL band to interactions between self-trapped holes and electrons trapped at clusters of oxygen vacancies [125].

[Production note: This figure is not included in this digital copy due to copyright restrictions.]

Figure 2.12. Schematic diagram describing the luminance mechanism in β-Ga_2O_3. This figure is reprinted from [125].

The luminance spectra are also influenced by factors such as temperature. For instance, for undoped β-Ga_2O_3, at lower temperatures (below 200 K), the UVL band is more pronounced. As the temperature rises, the intensities of the GL and BL bands increase, while the UVL band diminishes. This behaviour is likely due to enhanced recombination at deep-level defects at elevated temperatures [125].

2.3.4. Environmental Applications of Gallium Oxide

2.3.4.1. Solar-blind detectors

Ga_2O_3 possesses a wide bandgap, high breakdown voltage, optical transparency, and tuneable conductivity, making it an ideal candidate for environmental applications such as deep-ultraviolet photodetectors (DUV-PDs) [126]. Natural UV radiation from sunlight encompasses various wavelengths; UVA (315-400 nm), UVB (280-315 nm), UVC (100-280 nm), and extreme UV (EUV) (10–120 nm) [126]. UVC radiation is completely absorbed by atmospheric diatomic oxygen and ozone [110], Consequently, the UV range between 200 and 280 nm, referred to as the "solar-blind" region, as it has low background level on earth surface. Solar-blind photodetectors are designed with a cut-off wavelength below 280 nm, ensuring sensitivity exclusively to shorter wavelengths that do not penetrate the atmosphere. These detectors are immune to interference from typical outdoor lighting, making them suitable for applications such as ozone monitoring, flame detection, communications, military application, biochemistry, and UV leakage detection, due to their reliability and thermal stability [127]. To meet the requirements for solar-blind photodetectors, a bandgap of ~4.42 eV is needed. Ga_2O_3, particularly its monoclinic β-phase, is highly suitable as it exhibits a wide bandgap of 4.4–4.8 eV, corresponding to the solar-blind wavelength range of 258–280 nm. This property enables β-Ga_2O_3 to achieve high sensitivity across the entire solar-blind spectrum [127]. Ye et al. [128] fabricated solar-blind deep-ultraviolet photodetectors based on β-Ga_2O_3 thin films deposited on mica substrates. The schematic diagram and photocurrent response of this UV photodetector is shown in Fig. 2.13 below.

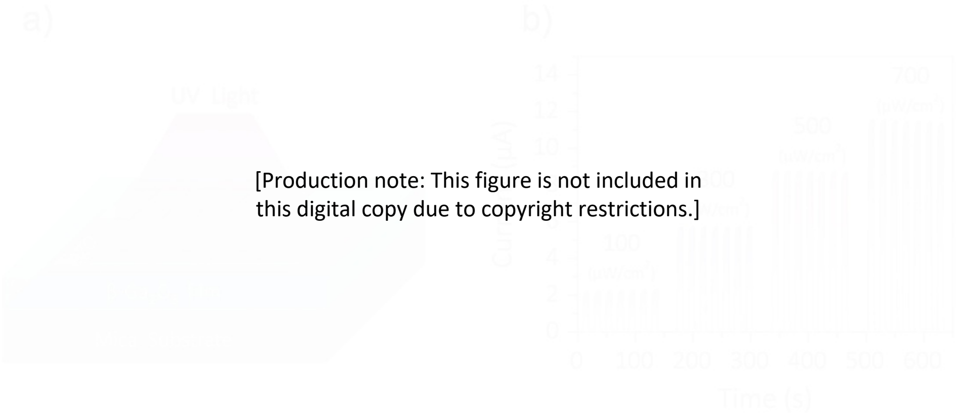

[Production note: This figure is not included in this digital copy due to copyright restrictions.]

Figure 2.13. (a) Schematic diagram of a β-Ga_2O_3-based photodetector. (b) Photocurrent response under different UV (254 nm) intensities. This figure is taken from [128].

2.3.4.2. Gas sensors

Ga_2O_3 emerged as a key material for high-temperature gas sensing due to its exceptional melting point (~1800 °C). Pearton et al. [129] highlighted the fabrication and applications of gallium oxide-based devices, emphasizing its versatility in detecting oxygen at temperatures above 900 °C and reducing gases at lower temperatures. Among the various phases of Ga_2O_3, the monoclinic β-phase is particularly advantageous due to its superior thermal stability and ease of preparation at annealing temperatures between 800 °C and 900 °C [129]. In high-temperature environments, such as internal combustion engines and furnaces, Ga_2O_3-based gas sensors play a critical role in monitoring exhaust gas composition by detecting changes in resistivity proportional to oxygen concentration. The conductance of Ga_2O_3 is influenced by its carrier concentration and electron mobility, both of which vary with temperature. During gas sensing, at elevated temperatures, changes in conductance are primarily driven by fluctuations in free electron density [130]. Bartic et al. [131] developed resistive oxygen sensors optimized for high-temperature applications, specifically for detecting oxygen at 1000 °C. These sensors utilized single-crystal gallium oxide with a platinum interdigital electrode configuration using

RF sputtering and chemical deposition methods. The results showed that the choice of technique significantly influenced the sensor performance. In addition to oxygen gas, Ga_2O_3 is capable of detecting various other gases, including hydrogen (H_2) [132], carbon oxides (CO, CO_2) [133], nitrogen oxides (NO_x, NO_2) [134], and ammonia (NH_3) [135].

2.3.4.3. Photocatalytic Degradation

The photocatalytic degradation efficiency of a semiconductor is determined by the energy of its charge carriers, which depend on the positions of its CB and VB. Consequently, a suitable band gap and efficient charge carrier separation are crucial criteria for selecting photocatalysts. Among metal oxide semiconductors, Ga_2O_3 stands out due to its wide band gap and strong redox properties (CB at −1.55 eV vs. NHE, VB at 3.25 eV vs. NHE) [136] . For example, Yoo et al. [137] compared the photocatalytic degradation performance of Ga_2O_3 and TiO_2 nanostructures for volatile organic compounds (VOCs) such as formaldehyde, acetaldehyde, toluene, and styrene. Their findings revealed that Ga_2O_3 exhibited significantly higher degradation rate compared to TiO_2 by a factor of 7 times higher for toluene, 8 times for styrene, 3 times for formaldehyde, and 2 times for acetaldehyde. The enhanced performance of Ga_2O_3, particularly for aromatic VOCs, is attributed to the highly energetic photo-generated carriers at its band edges, which enable efficient bond dissociation for compounds with high bond energies. The photocatalytic performance of Ga_2O_3 can be further enhanced by incorporating other metals or metal oxides. For example, Li et al. [138] studied the effects of adding Ag, Pt, Pd, and their oxides on the photodegradation performance of Ga_2O_3 for contaminants such as ciprofloxacin (CIP) and ronidazole (RNZ), as shown in Fig. 2.14 below.

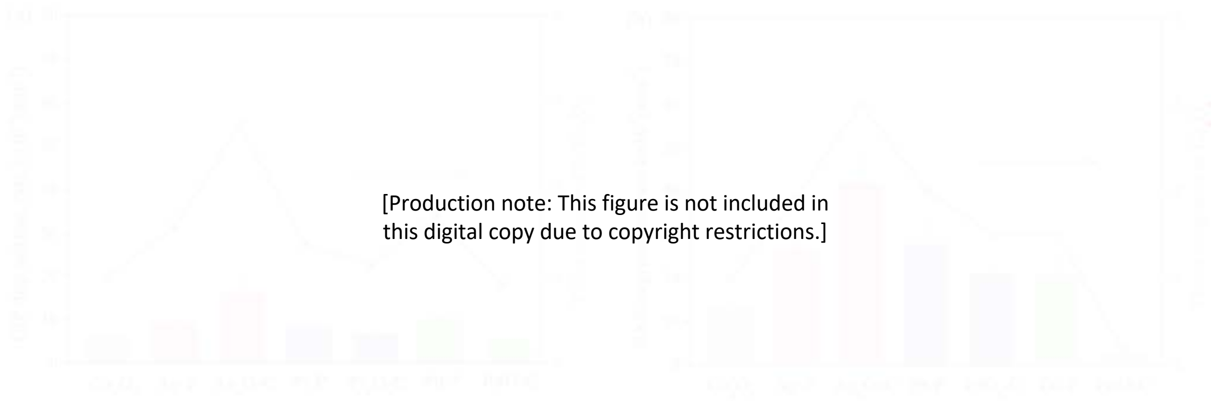

[Production note: This figure is not included in this digital copy due to copyright restrictions.]

Figure 2.14. Photocatalytic degradation performance of Ga_2O_3-based film for (a) CIP and (b) RNZ contaminants. This figure is replotted from [138].

However, due to its wide band gap, pure Ga_2O_3 is primarily active in the UV region. Efforts to extend its activity to the visible light spectrum include strategies such as introducing trap states during synthesis or doping with elements like rhodium (Rh) [139, 140].

2.4. Characterization of metal oxides in environmental applications

The use of metal oxides in environmental applications, such as pollutant degradation and water splitting, is governed by the complex interplay of their surface chemistry, crystal structure, morphology, and optical properties. A thorough understanding and precise control of these features are essential for the rational design and optimization of functional metal oxide-based materials. For example, examining the surface chemistry of metal oxides using X-ray photoelectron spectroscopy (XPS) can reveal the presence of surface functional groups (e.g., hydroxyls) and oxygen vacancies, both of which play critical roles in catalytic cycles and redox reactions [93]. Moreover, the optical properties of metal oxides, such as bandgap energy and light absorption capability, directly influence their ability to harness solar energy for photocatalytic applications. UV–Vis spectroscopy is commonly employed to estimate bandgap energies via Tauc plots [141], while techniques such as cathodoluminescence (CL) provide valuable insights into charge carrier recombination dynamics [142], which are crucial for understanding photocatalytic performance. Morphological features, including size, shape, surface roughness, and porosity, typically analyzed using scanning electron microscopy (SEM) and atomic force microscopy (AFM), influence the accessible surface area and the distribution of active sites, often resulting in improved photocatalytic activity [24]. Furthermore, the crystallographic phase and structural order of metal oxides, usually characterized by X-ray diffraction (XRD), significantly affect their electronic structure, stability, and charge transport properties of the photocatalytic systems [142].

This thesis presents a comprehensive investigation of ZnO and Ga_2O_3 photoactive materials, establishing correlations between their physicochemical properties and their performance in photodegradation and water splitting. The findings contributetothe rational design of metal oxides for sustainable environmental remediation.

2.5. References

[1] M.S.S. Danish, L.L. Estrella, I.M.A. Alemaida, A. Lisin, N. Moiseev, M. Ahmadi, M. Nazari, M. Wali, H. Zaheb, T. Senjyu, Photocatalytic applications of metal oxides for sustainable environmental remediation, Metals 11(1) (2021) 80.

[2] M. Ikram, M. Rashid, A. Haider, S. Naz, J. Haider, A. Raza, M. Ansar, M.K. Uddin, N.M. Ali, S.S. Ahmed, A review of photocatalytic characterization, and environmental cleaning, of metal oxide nanostructured materials, Sustainable Materials and Technologies 30 (2021) e00343.

[3] Y. Nosaka, A.Y. Nosaka, Generation and detection of reactive oxygen species in photocatalysis, Chemical reviews 117(17) (2017) 11302-11336.

[4] S. Swetha, B. Janani, S.S. Khan, A critical review on the development of metal-organic frameworks for boosting photocatalysis in the fields of energy and environment, Journal of Cleaner Production 333 (2022) 130164.

[5] T. Velempini, E. Prabakaran, K. Pillay, Recent developments in the use of metal oxides for photocatalytic degradation of pharmaceutical pollutants in water—a review, Materials Today Chemistry 19 (2021) 100380.

[6] S. Benkhaya, S. M'rabet, H. Lgaz, A. El Bachiri, A. El Harfi, Dyes: classification, pollution, and environmental effects, Dye biodegradation, mechanisms and techniques: Recent advances (2022) 1-50.

[7] X. Hu, X. Hu, Q. Peng, L. Zhou, X. Tan, L. Jiang, C. Tang, H. Wang, S. Liu, Y. Wang, Mechanisms underlying the photocatalytic degradation pathway of ciprofloxacin with heterogeneous TiO_2, Chemical Engineering Journal 380 (2020) 122366.

[8] I. Ul Haq, W. Ahmad, I. Ahmad, M. Yaseen, Photocatalytic oxidative degradation of hydrocarbon pollutants in refinery wastewater using TiO_2 as catalyst, Water Environment Research 92(12) (2020) 2086-2094.

[9] I. Nitoi, P. Oancea, M. Raileanu, M. Crisan, L. Constantin, I. Cristea, UV–VIS photocatalytic degradation of nitrobenzene from water using heavy metal doped titania, Journal of Industrial and Engineering Chemistry 21 (2015) 677-682.

[10] P. Raizada, V. Soni, A. Kumar, P. Singh, A.A.P. Khan, A.M. Asiri, V.K. Thakur, V.-H. Nguyen, Surface defect engineering of metal oxides photocatalyst for energy application and water treatment, Journal of Materiomics 7(2) (2021) 388-418.

[11] K.M. Reza, A. Kurny, F. Gulshan, Parameters affecting the photocatalytic degradation of dyes using TiO_2: a review, Applied Water Science 7 (2017) 1569-1578.

[12] A. Sirelkhatim, S. Mahmud, A. Seeni, N.H.M. Kaus, L.C. Ann, S.K.M. Bakhori, H. Hasan, D. Mohamad, Review on zinc oxide nanoparticles: antibacterial activity and toxicity mechanism, Nano-micro letters 7 (2015) 219-242.

[13] S. Liang, K. Xiao, Y. Mo, X. Huang, A novel ZnO nanoparticle blended polyvinylidene fluoride membrane for anti-irreversible fouling, Journal of membrane science 394 (2012) 184-192.

[14] A.N.C.O. Cambrussi, A.Í.S. Morais, A.d.M. Neris, J.A. Osajima, E.C.d. Silva Filho, A.B. Ribeiro, Photodegradation study of TiO_2 and ZnO in suspension using miniaturized tests, Matéria (Rio de Janeiro) 24(4) (2019) e12482.

[15] M. Kouhail, K. Elberouhi, Z. Elahmadi, A. Benayada, S. Gmouh, A Comparative study between TiO_2 and ZnO photocatalysis: Photocatalytic degradation of textile dye, IOP Conference Series: Materials Science and Engineering, IOP Publishing, 2020, p. 012009.

[16] D. Štrbac, C.A. Aggelopoulos, G. Štrbac, M. Dimitropoulos, M. Novaković, T. Ivetić, S.N. Yannopoulos, Photocatalytic degradation of Naproxen and methylene blue: Comparison between ZnO, TiO_2 and their mixture, Process Safety and Environmental Protection 113 (2018) 174-183.

[17] F. Abdullah, N.A. Bakar, M.A. Bakar, Comparative study of chemically synthesized and low temperature bio-inspired Musa acuminata peel extract mediated zinc oxide nanoparticles for enhanced visible-photocatalytic degradation of organic contaminants in wastewater treatment, Journal of hazardous materials 406 (2021) 124779.

[18] A.N. Tuama, L.H. Alzubaidi, M.H. Jameel, K.H. Abass, M.Z.H. bin Mayzan, Z.N. Salman, Impact of electron–hole recombination mechanism on the photocatalytic performance of ZnO in water treatment: A review, Journal of Sol-Gel Science and Technology (2024) 1-15.

[19] D. Jassby, J. Farner Budarz, M. Wiesner, Impact of aggregate size and structure on the photocatalytic properties of TiO_2 and ZnO nanoparticles, Environmental science & technology 46(13) (2012) 6934-6941.

[20] A.J. Jafari, R.R. Kalantari, M. Kermani, M.H. Firooz, Photocatalytic degradation data of benzene and toluene by ZnO coated on glass plates under simulated sunlight, Data in brief 20 (2018) 490-495.

[21] J.B. Zhong, J.Z. Li, X.Y. He, J. Zeng, Y. Lu, J.J. He, F. Zhong, Fabrication and catalytic performance of SiO_2-ZnO composite photocatalyst, Synthesis and Reactivity in Inorganic, Metal-Organic, and Nano-Metal Chemistry 44(8) (2014) 1203-1207.

[22] M.R. Abukhadra, A. Helmy, M.F. Sharaf, M.A. El-Meligy, A.T.A. Soliman, Instantaneous oxidation of levofloxacin as toxic pharmaceutical residuals in water using clay nanotubes decorated by ZnO (ZnO/KNTs) as a novel photocatalyst under visible light source, Journal of Environmental Management 271 (2020) 111019.

[23] L. Shen, Z. Huang, Y. Liu, R. Li, Y. Xu, G. Jakaj, H. Lin, Polymeric membranes incorporated with ZnO nanoparticles for membrane fouling mitigation: A brief review, Frontiers in chemistry 8 (2020) 224.

[24] A.T. Le, T.D.H. Le, K.-Y. Cheong, S.-Y. Pung, Immobilization of zinc oxide-based photocatalysts for organic pollutant degradation: A review, Journal of Environmental Chemical Engineering 10(5) (2022) 108505.

[25] T. Peters, Membrane technology for water treatment, Chemical engineering & technology 33(8) (2010) 1233-1240.

[26] R. Gayatri, E. Yuliwati, J. Jaafar, A.N.S. Fizal, M.S. Hossain, M. Zulkifli, A.N.A. Yahaya, W. Taweepreda, Polymer-Based Nanocomposite Membranes for Industrial Wastewater Treatment: A Review, Journal of Environmental Chemical Engineering (2024) 113276.

[27] S. Zhao, W. Yan, M. Shi, Z. Wang, J. Wang, S. Wang, Improving permeability and antifouling performance of polyethersulfone ultrafiltration membrane by incorporation of ZnO-DMF dispersion containing nano-ZnO and polyvinylpyrrolidone, Journal of Membrane Science 478 (2015) 105-116.

[28] A. Moezzi, A.M. McDonagh, M.B. Cortie, Zinc oxide particles: Synthesis, properties and applications, Chemical engineering journal 185 (2012) 1-22.

[29] A. Ahmad, A. Abdulkarim, S. Ismail, B. Ooi, Preparation and characterisation of PES-ZnO mixed matrix membranes for humic acid removal, Desalination and Water Treatment 54(12) (2015) 3257-3268.

[30] M. Sheikh, M. Pazirofteh, M. Dehghani, M. Asghari, M. Rezakazemi, C. Valderrama, J.-L. Cortina, Application of ZnO nanostructures in ceramic and polymeric membranes for water and wastewater technologies: a review, Chemical Engineering Journal 391 (2020) 123475.

[31] J. Li, L.-F. Ren, M. Huang, J. Yang, J. Shao, Y. He, Facile preparation of omniphobic PDTS-ZnO-PVDF membrane with excellent anti-wetting property in direct contact membrane distillation (DCMD), Journal of Membrane Science 650 (2022) 120404.

[32] S.K. Hubadillah, M.R. Jamalludin, M.H.D. Othman, Y. Iwamoto, Recent progress on low-cost ceramic membrane for water and wastewater treatment, Ceramics International 48(17) (2022) 24157-24191.

[33] W.A. Meulenberg, J. Mertens, M. Bram, H.-P. Buchkremer, D. Stöver, Graded porous TiO_2 membranes for microfiltration, Journal of the European Ceramic Society 26(4-5) (2006) 449-454.

[34] A. Abdullayev, M.F. Bekheet, D.A. Hanaor, A. Gurlo, Materials and applications for low-cost ceramic membranes, Membranes 9(9) (2019) 105.

[35] H. Lim, Y. Gu, S.T. Oyama, Reaction of primary and secondary products in a membrane reactor: studies of ethanol steam reforming with a silica–alumina composite membrane, Journal of Membrane Science 351(1-2) (2010) 149-159.

[36] S. Yue, Z. Yan, Y. Shi, G. Ran, Synthesis of zinc oxide nanotubes within ultrathin anodic aluminum oxide membrane by sol–gel method, Materials Letters 98 (2013) 246-249.

[37] L. Naszályi, F. Bosc, A. El Mansouri, A. van Der Lee, D. Cot, Z. Hórvölgyi, A. Ayral, Sol–gel-derived mesoporous SiO_2/ZnO active coating and development of multifunctional ceramic membranes, Separation and purification technology 59(3) (2008) 304-309.

[38] A. Sinha, S. Lulu, S. Vino, S. Banerjee, S. Acharjee, W.J. Osborne, Degradation of reactive green dye and textile effluent by Candida sp. VITJASS isolated from wetland paddy rhizosphere soil, Journal of environmental chemical engineering 6(4) (2018) 5150-5159.

[39] S.R. Manippady, A. Singh, B.M. Basavaraja, A.K. Samal, S. Srivastava, M. Saxena, Iron–carbon hybrid magnetic nanosheets for adsorption-removal of organic dyes and 4-nitrophenol from aqueous solution, ACS Applied Nano Materials 3(2) (2020) 1571-1582.

[40] Y. Yulizar, D.O.B. Apriandanu, R.I. Ashna, La_2CuO_4-decorated ZnO nanoparticles with improved photocatalytic activity for malachite green degradation, Chemical Physics Letters 755 (2020) 137749.

[41] J. Rodrigues, T. Hatami, J.M. Rosa, E.B. Tambourgi, L.H.I. Mei, Photocatalytic degradation using ZnO for the treatment of RB19 and RB21 dyes in industrial effluents and mathematical modeling of the process, Chemical Engineering Research and Design 153 (2020) 294-305.

[42] Q.T.H. Ta, E. Cho, A. Sreedhar, J.-S. Noh, Mixed-dimensional, three-level hierarchical nanostructures of silver and zinc oxide for fast photocatalytic degradation of multiple dyes, Journal of Catalysis 371 (2019) 1-9.

[43] F. Abdullah, N.A. Bakar, M.A. Bakar, Current advancements on the fabrication, modification, and industrial application of zinc oxide as photocatalyst in the removal of organic and inorganic contaminants in aquatic systems, Journal of hazardous materials 424 (2022) 127416.

[44] K. Selvakumar, A. Raja, M. Arunpandian, K. Stalindurai, P. Rajasekaran, P. Sami, E. Nagarajan, M. Swaminathan, Efficient photocatalytic degradation of ciprofloxacin and bisphenol A under visible light using Gd_2WO_6 loaded ZnO/bentonite nanocomposite, Applied Surface Science 481 (2019) 1109-1119.

[45] S.H. Khan, B. Pathak, Zinc oxide based photocatalytic degradation of persistent pesticides: A comprehensive review, Environmental nanotechnology, monitoring & management 13 (2020) 100290.

[46] S. Yadav, N. Kumar, V. Kumari, A. Mittal, S. Sharma, Photocatalytic degradation of Triclopyr, a persistent pesticide by ZnO/SnO_2 nano-composities, Materials Today: Proceedings 19 (2019) 642-645.

[47] K. Kabra, R. Chaudhary, R.L. Sawhney, Treatment of hazardous organic and inorganic compounds through aqueous-phase photocatalysis: a review, Industrial & engineering chemistry research 43(24) (2004) 7683-7696.

[48] S.A.A. Shukor, R. Hamzah, M.A. Bakar, N. Noriman, A.A. Al-Rashdi, Z. Razlan, A. Shahriman, I. Zunaidi, W. Khairunizam, Metal oxide and activated carbon as photocatalyst for waste water treatment, IOP conference series: Materials science and engineering, IOP Publishing, 2019, p. 012066.

[49] C. Bao, M. Chen, X. Jin, D. Hu, Q. Huang, Efficient and stable photocatalytic reduction of aqueous hexavalent chromium ions by polyaniline surface-hybridized ZnO nanosheets, Journal of Molecular Liquids 279 (2019) 133-145.

[50] A.T. Le, S.-Y. Pung, S. Sreekantan, A. Matsuda, Mechanisms of removal of heavy metal ions by ZnO particles, Heliyon 5(4) (2019).

[51] H. Wake, Oil refineries: a review of their ecological impacts on the aquatic environment, Estuarine, Coastal and Shelf Science 62(1-2) (2005) 131-140.

[52] L. Yan, Y. Wang, J. Li, H. Ma, H. Liu, T. Li, Y. Zhang, Comparative study of different electrochemical methods for petroleum refinery wastewater treatment, Desalination 341 (2014) 87-93.

[53] M. Keramati, B. Ayati, Petroleum wastewater treatment using a combination of electrocoagulation and photocatalytic process with immobilized ZnO nanoparticles on concrete surface, Process Safety and Environmental Protection 126 (2019) 356-365.

[54] A. Agarwalla, S. Mishra, K. Mohanty, Treatment and recycle of harvested microalgal effluent using powdered activated carbon for reducing water footprint and enhancing biofuel production under a biorefinery model, Bioresource Technology 360 (2022) 127598.

[55] V.O. Mkpuma, N.R. Moheimani, H. Ennaceri, Microalgal dewatering with focus on filtration and antifouling strategies: A review, Algal Research 61 (2022) 102588.

[56] P.J.l.B. Williams, L.M. Laurens, Microalgae as biodiesel & biomass feedstocks: Review & analysis of the biochemistry, energetics & economics, Energy & environmental science 3(5) (2010) 554-590.

[57] S. Kandasamy, B. Zhang, Z. He, N. Bhuvanendran, A.I. EL-Seesy, Q. Wang, M. Narayanan, P. Thangavel, M.A. Dar, Microalgae as a multipotential role in commercial applications: current scenario and future perspectives, Fuel 308 (2022) 122053.

[58] I.L. Drexler, D.H. Yeh, Membrane applications for microalgae cultivation and harvesting: a review, Reviews in Environmental Science and Bio/Technology 13 (2014) 487-504.

[59] M. Roy, K. Mohanty, A comprehensive review on microalgal harvesting strategies: Current status and future prospects, Algal Research 44 (2019) 101683.

[60] N. Kumar, C. Banerjee, S. Negi, P. Shukla, Microalgae harvesting techniques: updates and recent technological interventions, Critical Reviews in Biotechnology 43(3) (2023) 342-368.

[61] N. Laraib, A. Hussain, A. Javid, T. Noor, Q.-u.-A. Ahmad, A. Chaudhary, M. Manzoor, M. Akmal, S.M. Bukhari, W. Ali, Recent trends in microalgal harvesting: an overview, Environment, Development and Sustainability (2021) 1-31.

[62] F. Fasaei, J. Bitter, P. Slegers, A. Van Boxtel, Techno-economic evaluation of microalgae harvesting and dewatering systems, Algal research 31 (2018) 347-362.

[63] E. Deng, X. Chen, D. Rub, H. Lin, Modeling and mitigating fouling of microfiltration membranes for microalgae dewatering, Separation and Purification Technology 315 (2023) 123707.

[64] Z. Zhao, K. Muylaert, I.F. Vankelecom, Applying membrane technology in microalgae industry: A comprehensive review, Renewable and Sustainable Energy Reviews 172 (2023) 113041.

[65] A. Boretti, There are hydrogen production pathways with better than green hydrogen economic and environmental costs, International Journal of Hydrogen Energy 46(46) (2021) 23988-23995.

[66] L. Clarizia, M.N. Nadagouda, D.D. Dionysiou, Recent advances and challenges of photoelectrochemical cells for hydrogen production, Current Opinion in Green and Sustainable Chemistry 41 (2023) 100825.

[67] M. Kumar, B. Meena, P. Subramanyam, D. Suryakala, C. Subrahmanyam, Recent trends in photoelectrochemical water splitting: the role of cocatalysts, NPG Asia Materials 14(1) (2022) 88.

[68] M. Grätzel, Photoelectrochemical cells, nature 414(6861) (2001) 338-344.

[69] M.G. Walter, E.L. Warren, J.R. McKone, S.W. Boettcher, Q. Mi, E.A. Santori, N.S. Lewis, Solar water splitting cells, Chemical reviews 110(11) (2010) 6446-6473.

[70] J.B. Sambur, T.-Y. Chen, E. Choudhary, G. Chen, E.J. Nissen, E.M. Thomas, N. Zou, P. Chen, Sub-particle reaction and photocurrent mapping to optimize catalyst-modified photoanodes, Nature 530(7588) (2016) 77-80.

[71] A. Thakur, D. Ghosh, P. Devi, K.-H. Kim, P. Kumar, Current progress and challenges in photoelectrode materials for the production of hydrogen, Chemical Engineering Journal 397 (2020) 125415.

[72] S. Lin, H. Huang, T. Ma, Y. Zhang, Photocatalytic oxygen evolution from water splitting, Advanced Science 8(1) (2021) 2002458.

[73] J. Augustynski, B. Alexander, R. Solarska, Metal oxide photoanodes for water splitting, Top. Curr. Chem 303 (2011) 1-38.

[74] Y. Qiu, S.-F. Leung, Q. Zhang, B. Hua, Q. Lin, Z. Wei, K.-H. Tsui, Y. Zhang, S. Yang, Z. Fan, Efficient photoelectrochemical water splitting with ultrathin films of hematite on three-dimensional nanophotonic structures, Nano letters 14(4) (2014) 2123-2129.

[75] R. Pessoa, M. Fraga, L. Santos, M. Massi, H. Maciel, Nanostructured thin films based on TiO_2 and/or SiC for use in photoelectrochemical cells: A review of the material characteristics, synthesis and recent applications, Materials Science in Semiconductor Processing 29 (2015) 56-68.

[76] Y. Chen, X. Feng, Y. Liu, X. Guan, C. Burda, L. Guo, Metal oxide-based tandem cells for self-biased photoelectrochemical water splitting, ACS Energy Letters 5(3) (2020) 844-866.

[77] P. Xu, Y. Sun, C. Shi, F. Xu, H. Pan, The electronic structure and spectral properties of ZnO and its defects, Nuclear Instruments and Methods in Physics Research Section B: Beam Interactions with Materials and Atoms 199 (2003) 286-290.

[78] J. Theerthagiri, S. Salla, R. Senthil, P. Nithyadharseni, A. Madankumar, P. Arunachalam, T. Maiyalagan, H.-S. Kim, A review on ZnO nanostructured materials: energy, environmental and biological applications, Nanotechnology 30(39) (2019) 392001.

[79] A.Y. Faid, N.K. Allam, Stable solar-driven water splitting by anodic ZnO nanotubular semiconducting photoanodes, RSC Advances 6(83) (2016) 80221-80225.

[80] S.-S. Li, Y.-K. Su, Improvement of the performance in Cr-doped ZnO memory devices via control of oxygen defects, RSC advances 9(6) (2019) 2941-2947.

[81] J. Bao, X. Zhang, B. Fan, J. Zhang, M. Zhou, W. Yang, X. Hu, H. Wang, B. Pan, Y. Xie, Ultrathin spinel-structured nanosheets rich in oxygen deficiencies for enhanced electrocatalytic water oxidation, Angewandte Chemie 127(25) (2015) 7507-7512.

[82] B. Amudhavalli, R. Mariappan, M. Prasath, Synthesis chemical methods for deposition of ZnO, CdO and CdZnO thin films to facilitate further research, Journal of Alloys and Compounds 925 (2022) 166511.

[83] S. Swathi, E.S. Babu, R. Yuvakkumar, G. Ravi, A. Chinnathambi, S.A. Alharbi, D. Velauthapillai, Branched and unbranched ZnO nanorods grown via chemical vapor deposition for photoelectrochemical water-splitting applications, Ceramics International 47(7) (2021) 9785-9790.

[84] Z. Cai, B. Liu, X. Zou, H.-M. Cheng, Chemical vapor deposition growth and applications of two-dimensional materials and their heterostructures, Chemical reviews 118(13) (2018) 6091-6133.

[85] P. Basnet, S. Chatterjee, Structure-directing property and growth mechanism induced by capping agents in nanostructured ZnO during hydrothermal synthesis—A systematic review, Nano-structures & Nano-objects 22 (2020) 100426.

[86] S. Worasawat, T. Masuzawa, Y. Hatanaka, Y. Neo, H. Mimura, W. Pecharapa, Synthesis and characterization of ZnO nanorods by hydrothermal method, Materials Today: Proceedings 5(5) (2018) 10964-10969.

[87] A. Singh, K. Yadav, P. Thakur, F. Wan, B. Ravelo, A. Thakur, Review on the amelioration of ZnO and its composites: synthesis and applications, Indian Journal of Physics (2024) 1-22.

[88] K. Harun, F. Hussain, A. Purwanto, B. Sahraoui, A. Zawadzka, A.A. Mohamad, Sol–gel synthesized ZnO for optoelectronics applications: a characterization review, Materials research express 4(12) (2017) 122001.

[89] M. Ghorbani, H. Abdizadeh, M.R. Golobostanfard, Hierarchical porous ZnO films synthesized by sol–gel method using triethylenetetramine stabilizer, SN Applied Sciences 1(3) (2019) 267.

[90] D. Bokov, A. Turki Jalil, S. Chupradit, W. Suksatan, M. Javed Ansari, I.H. Shewael, G.H. Valiev, E. Kianfar, Nanomaterial by sol-gel method: synthesis and application, Advances in materials science and engineering 2021(1) (2021) 5102014.

[91] W. Gao, Z. Li, ZnO thin films produced by magnetron sputtering, Ceramics International 30(7) (2004) 1155-1159.

[92] J.T. Gudmundsson, Physics and technology of magnetron sputtering discharges, Plasma Sources Science and Technology 29(11) (2020) 113001.

[93] R. Garg, S. Gonuguntla, S. Sk, M.S. Iqbal, A.O. Dada, U. Pal, M. Ahmadipour, Sputtering thin films: Materials, applications, challenges and future directions, Advances in Colloid and Interface Science (2024) 103203.

[94] M.A. Cruz, O. Ceballos-Sanchez, E. Luévano-Hipólito, L. Torres-Martínez, ZnO thin films deposited by RF magnetron sputtering: Effects of the annealing and atmosphere conditions on the photocatalytic hydrogen production, International Journal of Hydrogen Energy 43(22) (2018) 10301-10310.

[95] R. Tang, S. Zhou, Z. Zhang, R. Zheng, J. Huang, Engineering nanostructure–interface of photoanode materials toward photoelectrochemical water oxidation, Advanced Materials 33(17) (2021) 2005389.

[96] H.S. Al-Salman, M. Abdullah, RF sputtering enhanced the morphology and photoluminescence of multi-oriented ZnO nanostructure produced by chemical vapor deposition, Journal of alloys and compounds 547 (2013) 132-137.

[97] A. Janotti, C.G. Van de Walle, New insights into the role of native point defects in ZnO, Journal of Crystal Growth 287(1) (2006) 58-65.

[98] A. Janotti, C.G. Van de Walle, Native point defects in ZnO, Physical Review B—Condensed Matter and Materials Physics 76(16) (2007) 165202.

[99] F. Oba, S.R. Nishitani, S. Isotani, H. Adachi, I. Tanaka, Energetics of native defects in ZnO, Journal of Applied Physics 90(2) (2001) 824-828.

[100] A. Janotti, C.G. Van de Walle, Fundamentals of zinc oxide as a semiconductor, Reports on progress in physics 72(12) (2009) 126501.

[101] C.A. Aggelopoulos, M. Dimitropoulos, A. Govatsi, L. Sygellou, C.D. Tsakiroglou, S.N. Yannopoulos, Influence of the surface-to-bulk defects ratio of ZnO and TiO_2 on their UV-mediated photocatalytic activity, Applied Catalysis B: Environmental 205 (2017) 292-301.

[102] J. Kim, M.-c. Kim, J. Yu, K. Park, H_2/Ar and vacuum annealing effect of ZnO thin films deposited by RF magnetron sputtering system, Current Applied Physics 10(3) (2010) S495-S498.

[103] X.-F. Su, J.-B. Chen, R.-M. He, Y. Li, J. Wang, C.-W. Wang, The preparation of oxygen-deficient ZnO nanorod arrays and their enhanced field emission, Materials Science in Semiconductor Processing 67 (2017) 55-61.

[104] Y. Qiu, S. Yang, ZnO nanotetrapods: controlled vapor-phase synthesis and application for humidity sensing, Advanced Functional Materials 17(8) (2007) 1345-1352.

[105] M. Higashiwaki, K. Sasaki, A. Kuramata, T. Masui, S. Yamakoshi, Gallium oxide (Ga_2O_3) metal-semiconductor field-effect transistors on single-crystal β-Ga_2O_3 (010) substrates, Applied Physics Letters 100(1) (2012).

[106] M. Higashiwaki, K. Sasaki, A. Kuramata, T. Masui, S. Yamakoshi, Development of gallium oxide power devices, physica status solidi (a) 211(1) (2014) 21-26.

[107] G.-S. Park, W.-B. Choi, J.-M. Kim, Y.C. Choi, Y.H. Lee, C.-B. Lim, Structural investigation of gallium oxide (β-Ga_2O_3) nanowires grown by arc-discharge, Journal of crystal growth 220(4) (2000) 494-500.

[108] B.J. Baliga, Gallium nitride devices for power electronic applications, Semiconductor Science and Technology 28(7) (2013) 074011.

[109] Y. Yuan, W. Hao, W. Mu, Z. Wang, X. Chen, Q. Liu, G. Xu, C. Wang, H. Zhou, Y. Zou, Toward emerging gallium oxide semiconductors: A roadmap, Fundamental Research 1(6) (2021) 697-716.

[110] X. Chen, F. Ren, S. Gu, J. Ye, Review of gallium-oxide-based solar-blind ultraviolet photodetectors, Photonics Research 7(4) (2019) 381-415.

[111] S. Stepanov, V. Nikolaev, V. Bougrov, A. Romanov, Gallium OXIDE: Properties and applica 498 a review, Rev. Adv. Mater. Sci 44 (2016) 63-86.

[112] R. Roy, V. Hill, E. Osborn, Polymorphism of Ga2O3 and the system Ga_2O_3—H2O, Journal of the American Chemical Society 74(3) (1952) 719-722.

[113] M. García-Carrión, J. Ramírez-Castellanos, E. Nogales, B. Méndez, C.C. You, S. Karazhanov, E.S. Marstein, Hybrid solar cells with β-and γ-gallium oxide nanoparticles, Materials Letters 261 (2020) 127088.

[114] B.R. Tak, S. Kumar, A.K. Kapoor, D. Wang, X. Li, H. Sun, R. Singh, Recent advances in the growth of gallium oxide thin films employing various growth techniques—a review, Journal of Physics D: Applied Physics 54(45) (2021) 453002.

[115] Y. Zhu, X. Xiu, F. Cheng, Y. Li, Z. Xie, T. Tao, P. Chen, B. Liu, R. Zhang, Y.-D. Zheng, Growth and nitridation of β-Ga_2O_3 thin films by Sol-Gel spin-coating epitaxy with post-annealing process, Journal of Sol-Gel Science and Technology 100 (2021) 183-191.

[116] S. Mobtakeri, E.S. Tuzemen, Ö. Ali, G. Emre, Characterization of Gallium Oxide/glass thin films grown by RF magnetron sputtering, Cumhuriyet Science Journal 41(4) (2020) 929-937.

[117] J.-H. Park, R. McClintock, M. Razeghi, Ga_2O_3 metal-oxide-semiconductor field effect transistors on sapphire substrate by MOCVD, Semiconductor Science and Technology 34(8) (2019) 08LT01.

[118] Q. Feng, F. Li, B. Dai, Z. Jia, W. Xie, T. Xu, X. Lu, X. Tao, J. Zhang, Y. Hao, The properties of gallium oxide thin film grown by pulsed laser deposition, Applied Surface Science 359 (2015) 847-852.

[119] W. Nunn, T.K. Truttmann, B. Jalan, A review of molecular-beam epitaxy of wide bandgap complex oxide semiconductors, Journal of materials research (2021) 1-19.

[120] A. Kuramata, K. Koshi, S. Watanabe, Y. Yamaoka, T. Masui, S. Yamakoshi, High-quality β-Ga_2O_3 single crystals grown by edge-defined film-fed growth, Japanese Journal of Applied Physics 55(12) (2016) 1202A2.

[121] J. Wang, X. Ji, Z. Yan, S. Qi, A. Zhong, P. Li, The role of oxygen vacancies in Ga_2O_3-based solar-blind photodetectors, Journal of Alloys and Compounds 970 (2024) 172448.

[122] J. Yao, T. Liu, B. Wang, Optical properties for the oxygen vacancies in β-Ga_2O_3 based on first-principles calculations, Materials Research Express 6(7) (2019) 075913.

[123] H.-L. Huang, C. Chae, J. Hwang, Perspective on atomic scale investigation of point and extended defects in gallium oxide, Journal of Applied Physics 131(19) (2022).

[124] H. Gao, S. Muralidharan, N. Pronin, M.R. Karim, S.M. White, T. Asel, G. Foster, S. Krishnamoorthy, S. Rajan, L.R. Cao, Optical signatures of deep level defects in Ga_2O_3, Applied Physics Letters 112(24) (2018).

[125] T. Onuma, Y. Nakata, K. Sasaki, T. Masui, T. Yamaguchi, T. Honda, A. Kuramata, S. Yamakoshi, M. Higashiwaki, Modeling and interpretation of UV and blue luminescence intensity in β-Ga_2O_3 by silicon and nitrogen doping, Journal of Applied Physics 124(7) (2018).

[126] D. Kaur, M. Kumar, A strategic review on gallium oxide based deep-ultraviolet photodetectors: recent progress and future prospects, Advanced optical materials 9(9) (2021) 2002160.

[127] U. Varshney, N. Aggarwal, G. Gupta, Current advances in solar-blind photodetection technology: Using Ga_2O_3 and AlGaN, Journal of Materials Chemistry C 10(5) (2022) 1573-1593.

[128] L. Ye, J. Yu, Y. Mao, X. Xuan, D. Pang, Y. Tang, H. Li, H. Zhang, W. Li, Mica-based β-Ga_2O_3 photodetector: Enabling solar-blind deep-ultraviolet detection with flexibility and transparency, Materials Today Communications 40 (2024) 109665.

[129] S. Pearton, J. Yang, P.H. Cary, F. Ren, J. Kim, M.J. Tadjer, M.A. Mastro, A review of Ga_2O_3 materials, processing, and devices, Applied Physics Reviews 5(1) (2018).

[130] A. Afzal, β-Ga_2O_3 nanowires and thin films for metal oxide semiconductor gas sensors: Sensing mechanisms and performance enhancement strategies, Journal of Materiomics 5(4) (2019) 542-557.

[131] P.R. Jubu, F. Yam, Influence of growth duration and nitrogen-ambient on the morphological and structural properties of beta-gallium oxide micro-and nanostructures, Materials Chemistry and Physics 239 (2020) 122043.

[132] Z. Liu, W. Qiu, X. Kuang, B. Li, C. Sun, R. Tu, S. Zhang, Enhanced H2 sensing mechanisms of β-Ga_2O_3: Electrical sensitivity and surface Reactivity, Applied Surface Science (2024) 162261.

[133] H. Zhai, Z. Wu, Z. Fang, Recent progress of Ga_2O_3-based gas sensors, Ceramics International 48(17) (2022) 24213-24233.

[134] J. Wang, S. Jiang, H. Liu, S. Wang, Q. Pan, Y. Yin, G. Zhang, P-type gas-sensing behavior of Ga_2O_3/Al_2O_3 nanocomposite with high sensitivity to NO_x at room temperature, Journal of Alloys and Compounds 814 (2020) 152284.

[135] R. Pilliadugula, N.G. Krishnan, Effect of pH dependent morphology on room temperature NH3 sensing performances of β-Ga_2O_3, Materials Science in Semiconductor Processing 112 (2020) 105007.

[136] J. Yang, T. Kang, P. Han, W. Chen, Z. Chen, Z. Wan, Z. Liu, F. Teng, P. Hu, H. Fan, Enhanced photocatalytic performance of Ga_2O_3 hollow spheres prepared by hard template technique, Materials Science in Semiconductor Processing 178 (2024) 108466.

[137] T.H. Yoo, H. Ryou, I.G. Lee, J. Cho, B.J. Cho, W.S. Hwang, Comparison of Ga_2O_3 and TiO_2 nanostructures for photocatalytic degradation of volatile organic compounds, Catalysts 10(5) (2020) 545.

[138] M. Li, Z. Yu, Y. Hou, Q. Liu, L. Qian, C. Lian, X. Rao, X. Yang, Charge trapping and transfer mechanisms of noble metals and metal oxides deposited Ga_2O_3 toward typical contaminant degradation, Chemical Engineering Journal 370 (2019) 1119-1127.

[139] N. Syed, A. Zavabeti, M. Mohiuddin, B. Zhang, Y. Wang, R.S. Datta, P. Atkin, B.J. Carey, C. Tan, J. Van Embden, Sonication-assisted synthesis of gallium oxide suspensions featuring trap state absorption: test of photochemistry, Advanced Functional Materials 27(43) (2017) 1702295.

[140] S. Kikkawa, K. Teramura, H. Asakura, S. Hosokawa, T. Tanaka, Development of Rh-Doped Ga_2O_3 Photocatalysts for Reduction of CO_2 by H_2O as an Electron Donor at a More than 300 nm Wavelength, The Journal of Physical Chemistry C 122(37) (2018) 21132-21139.

[141] P. Makuła, M. Pacia, W. Macyk, How to correctly determine the band gap energy of modified semiconductor photocatalysts based on UV–Vis spectra, ACS Publications, 2018, pp. 6814-6817.

[142] M. Ebaid, J.-H. Kang, S.-H. Lim, Y.-H. Cho, S.-W. Ryu, Towards highly efficient photoanodes: the role of carrier dynamics on the photoelectrochemical performance of InGaN/GaN multiple quantum well coaxial nanowires, RSC Advances 5(30) (2015) 23303-23310.

Chapter 3. Photocatalytic oxide-based membranes for microalgae harvesting

This chapter investigates the photocatalytic degradation performance of ZnO coatings integrated with membrane technology for microalgae harvesting. The chapter is divided into two main sections:

Section 3.1 focusses on the development of ZnO-coated stainless-steel membranes with self-cleaning properties. A ZnO coating layer was applied to porous stainless-steel substrates to enhance microalgae harvesting efficiency in a cross-flow filtration system. The coated membranes demonstrated significant improvements in water permeate flux and self-cleaning capabilities after microalgae harvesting, which is essential for sustainable biofuel production. However, despite the initial improvement in antifouling properties due to the ZnO coating, the large pore size of the stainless steel substrate led to rapid clogging of the filtration module, limiting its filtration performance to a short period of time.

Section 3.2 addresses the limitations of the stainless-steel membrane system by presenting a significant improvement in the ZnO photocatalytic filtration system. This enhancement was achieved by incorporating the ZnO coating layer into ceramic membranes with smaller pore sizes. These ceramic membranes were used into a submerged filtration setup with an integrated backwashing cleaning process. This approach demonstrated superior performance compared to the previously reported stainless-steel membrane system.

3.1. Improved flux and anti-fouling performance of a photocatalytic ZnO membrane on porous stainless steel substrate for microalgae harvesting

Abstract

Photocatalytic self-cleansing ZnO membranes were developed and used for pre-concentrating microalgae solution prior to harvesting. The inorganic membranes were fabricated via two different methods: (i) direct deposition of ZnO onto a porous stainless steel substrate and (ii) post-growth oxidation of a deposited metallic Zn layer. Systematic surface characterisation revealed a thin layer of homogeneous, crystalline ZnO on the porous membrane. Direct ZnO deposition resulted in a thicker layer with higher UV light absorption capability compared with the post-growth oxidization method. The ZnO coating made the membrane surface highly hydrophilic, resulting in two-fold increase in water permeability compared to the base stainless steel substrate. The high hydrophilicity of the ZnO-coated membrane also led to an increase in the permeate flux of the microalgae solution by up 100%, making it suitable for microalgae pre-concentration. Upon UV light irradiation, the ZnO membrane demonstrated self-cleansing capability due to the photocatalytic activity of the ZnO coating layer. After 30 minutes of UV irradiation, the ZnO membrane could achieve 60% permeability recovery after complete fouling. No recovery was observed with the base stainless steel membrane, which was used as the control.

Keywords: ZnO coating; inorganic microfiltration; photocatalysis; membrane cleaning; self-cleansing; algae harvesting.

3.1.1. Introduction

New and improved technologies are required to address the climate change and global warming challenge. This is also evidenced in the field of membrane separation by many dedicated works to explore new and functional materials that can be used for unconventional separation applications such as resource recovery and the production of renewable fuel [1, 2]. A notable example is the current research and development effort to commercialize microalgae-based biofuel to support hard to abate sectors such as aviation and marine time-freight [3, 4], where electrification has not proven to be viable. Microalgae-based biodiesel production has been demonstrated at pilot scale [5], however, this approach cannot currently compete with petroleum-based fuel due to the high cost of microalgae harvesting. Thus, new technique to cost-effectively separate and harvest microalgae at scale for subsequent lipid extraction and biodiesel production is urgently needed.

Microalgae-based biofuel has been identified as the most suitable option to complement with renewable energy (e.g. solar and wind) to sustainably support the transition of the global economy toward net zero emission [6]. There are several added advantages from microalgae production including the removal of nutrients (e.g. nitrogen and phosphorous) from wastewater and carbon dioxide from the atmosphere [7-9]. If left untreated, nutrients in wastewater can lead to eutrophication and other environmental consequence. Microalgae are fast-growing photosynthetic microorganisms, ubiquitous in all surface waters. They can photosynthesize 40 times faster than terrestrial plants and can provide a direct and viable route toward a net-zero economy [10]. Microalgae are more commercially competitive for biofuel production than any other crops. Biofuel yield per hectare from microalgae is 13 times higher than palm oil and five times higher than land-based energy crop [11]. However, high harvesting and extraction costs remain a major key hurdle to large-scale microalgae-based biofuel production. Harvesting alone can account for up to 60% of the total cost of biofuel production. Conventional processes for microalgae harvesting including centrifugation and polymer flocculation to separate microalgal biomass from water. These processes are expensive because at maturity, biomass content of the microalgae culture is only about 1 kg/m^3. Recent works have shown the potential of preconcentrating microalgae using membrane separation prior to harvesting to lower the cost [8, 12, 13].

Innovative techniques such as membrane vibration and frequent aerated-backwashing have been developed to address the challenge of membrane fouling due to the high biomass content [8, 13]. While these techniques are effective in recovering the membrane flux, highly viscous extracellular polymeric materials from microalgae cells can cause a gradual process deterioration over time [8]. Moreover, acid cleaning can degrade membrane components and alter its surface properties, as well as raise additional concerns regarding the safe handling and disposal of acidic waste [14]. Thus, functionalized membrane materials with self-cleansing capability are needed to overcome this additional challenge. Several strategies have been explored, for example, Zheng *et al.* has recently developed a microporous carbon-based electro-Fenton membrane for microalgae harvesting [12]. Their results showed that the membrane could effectively prevent irreversible fouling during microalgae harvesting. There have been few studies using stainless steel (SST) membranes for microalgal filtration. Xu *et al.* [15] found the highest pure water flux recovery of 39.92% using chemical free backwashing method for the harvesting of cyanobacteria microalgae. Ahmed *et al.* [16] reported 68% flux recovery with NaOH cleaning at ambient temperature and 98% flux recovery when the cleaning solution temperature increased to 60 °C.

The potential of developing photoactive membrane materials to produce reactive oxygen species (ROS) such as superoxide (O_2^-) and hydroxyl radicals ($\mathrm{OH}^{\square}$) for self-cleansing capability have been suggested [17, 18]. ZnO is a widely used photocatalyst that has the ability to degrade organic materials and kill various bacteria through induced oxidative stress [19, 20].

Additionally, ZnO films have been shown to have good stability at pH above 5 [21], thus ZnO-coated membranes are expected to be robust in water treatment applications at near neutral pH. Although modifying the membrane surface with hydrophilic and photocatalytic oxides can improve fouling resistance, the formation of poor quality coating can cause particle aggregation and severely reduce the membrane performance [22]. Several membrane coating methods, such as dip coating [23], electrospinning [24], acid-catalyzed sol–gel [25], vacuum filtration [26], and atomic layer deposition [27], have been used; however, most of these fabrication methods suffer from drawbacks such as the fragility of coatings, non-uniformity and a shortage of suitable membranes. Sputter deposition, on the other hand, is a versatile technique that is capable of producing uniform, strongly adhered large-area coatings for a wide range of substrates with non-flat or curved surface morphologies, such as porous membranes [28]. The thickness and composition of the coated layer can significantly influence the membrane's photocatalytic activity, hydrophilicity, and pores size [28-30]. It is noteworthy that the use of photocatalytic ZnO coatings on porous membranes for microalgal filtration and harvesting has not been studied to date.

This work reports a new technique to prepare photocatalytic ZnO membranes on a porous stainless steel substrate for microalgae harvesting. We demonstrate two viable approaches for fabricating ZnO-coated membranes, the first involving post-oxidation of a sputtered Zn film and the second reactive sputtering deposition of ZnO coating. The ZnO membranes were systematically characterized using a range of morphological, compositional, structural and optical analytical techniques. The filtration performance of the coated membranes is analyzed in terms of the permeability of microalgae solutions and microalgae rejection. The role of the ZnO coating on biofouling reduction in microalgae filtration is also investigated using ultraviolet (UV) light irradiation and explained by the photoactivity of ZnO under UV activation.

3.1.2. Materials and Methods

3.1.2.1. Membrane preparation

The base material used in this study was a porous and highly corrosion resistant 316L SST sheet from Mott Corporation. The SST sheet has a thickness of 1.6 mm and average pore size of 10 µm. Before coating with ZnO, the SST sheet was successively cleaned with acetone, isopropanol, and deionized water in an ultrasonic bath for 20 minutes for each solvent, dried by instrument grade N_2 gas, and stored in an airtight container. The SST membrane was continuously rotated at a distance of approximately 10 cm from the sputtering target. After that the sputtering chamber was plumbed to reach a base pressure of 9×10^{-6} torr.

Two different methods were used to prepare ZnO-coated SST membranes as illustrated in Fig. 3.1. In the first method (denoted as Zn-SST), a layer of metallic Zn was sputtered onto the SST sheet using a Zn target (DC sputtering power 50 W in Ar atmosphere at 4×10^{-3} torr), and subsequently oxidized in ambient air for 2 hours at 500 ºC to form ZnO. In the second method (denoted as ZnO-SST), a ZnO layer was deposited onto the SST sheet using DC reactive sputtering of a Zn target in a gas mixture of Ar and O_2 at the ratio of 3/1 (sputtering power of 200 W, gas pressure of 4×10^{-3} torr). The ZnO-coated membrane was also annealed under similar condition to produce a crystalline coating layer. In all coating experiments, a glass slide was also placed in the sputtering chamber to obtain a film of ZnO with identical thickness for XRD and UV-Vis analysis. For comparison, the uncoated SST membrane was also annealed in ambient air for 2 hours and used as the control sample.

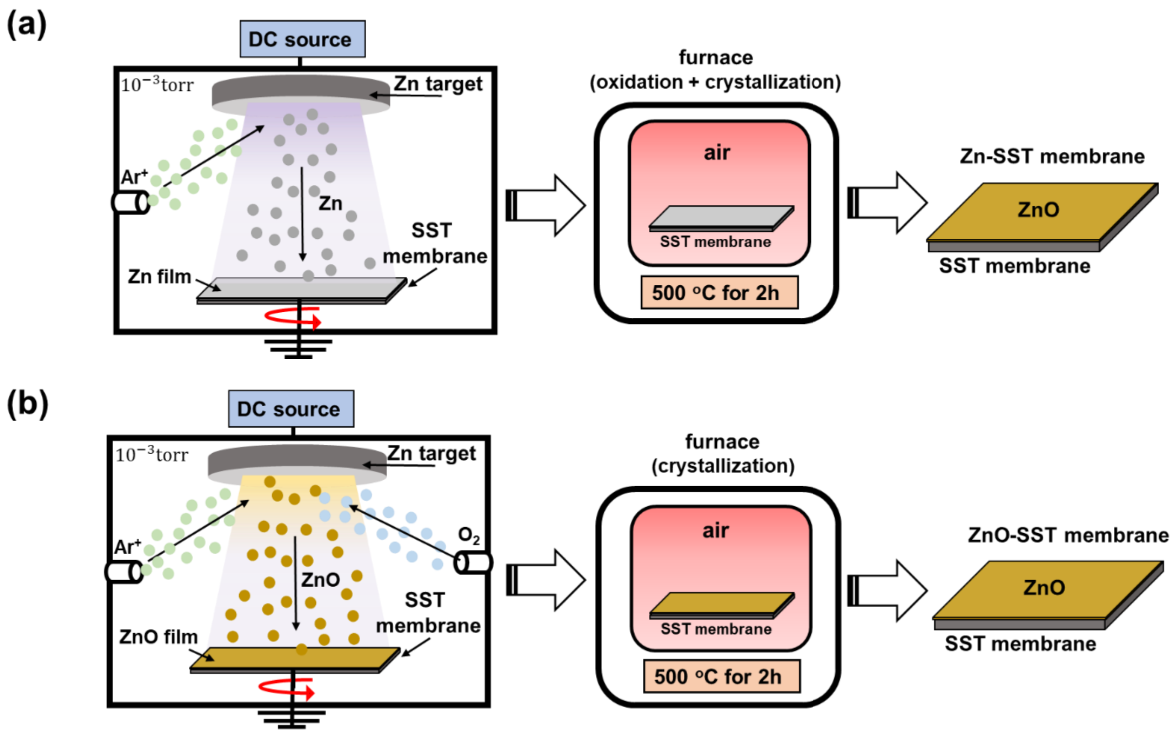

Figure 3.1. Schematic diagram of (a) Zn-SST and (b) ZnO-SST membrane fabrication by DC sputtering deposition.

3.1.2.2. Membrane characterisation

The coated and uncoated membranes were characterized in terms of surface morphology, thickness, and hydrophobicity of the ZnO coating layer. Crystallinity of the ZnO film was examined using X-ray diffraction (XRD, Bruker D8 Discovery diffractometer) using Cu Kα radiation. Optical properties were investigated using an Agilent Cary 7000 UV-Vis spectrophotometer. The XRD and UV-Vis measurements were performed on ZnO film on a glass slice (section 3.12.1). The membrane surface was examined using field emission scanning electron microscope (Zeiss Supra 55VP) equipped with an Oxfords Instruments Energy Dispersive Spectrometer (EDS). X-ray photoelectron spectroscopy (XPS) data were collected at photon energies of 650 eV and 1486.6 eV on the soft x-ray spectroscopy beamline at the Australian Synchrotron. The thickness and hydrophilicity of the ZnO coatings were determined using a profilometer (Bruker DektakXT) and contact angle measurements (Attension optical tensiometer), respectively.

3.1.2.3. Membrane filtration system

A lab scale membrane filtration system was used. The system consisted of a membrane module, circulation pump, flow meter, digital balance, feed reservoir, and permeate water reservoir (Figure 3.2). The membrane module was made of two symmetric and identical acrylic semi-cells. The flow channel of the membrane has a surface area of 1.8×1.8 cm^2. The feed solution was circulated using a Cole-Parmer pump (model 75211-15), while the flow rate was fixed by a Cole-Parmer flow meter (model 32461-42). The transmembrane pressure was measured using a digital pressure gauge (Pressure Meter SDL700). The permeate water was collected on the permeate storage and the water flux was measured by the digital balance (PGL 8001).

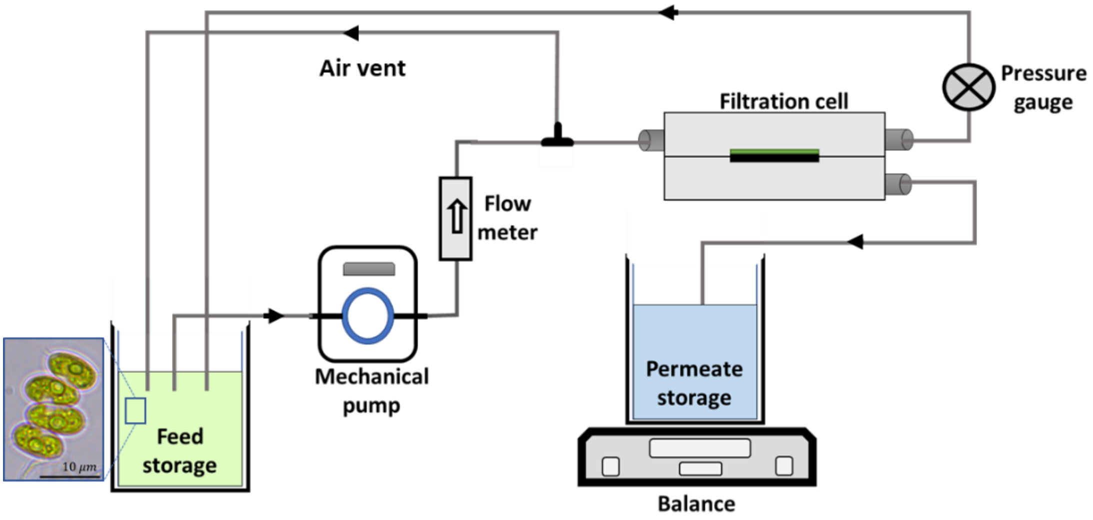

Figure 3.2. Schematic diagram of the membrane filtration system.

During the filtration experiment, microalgae solution was circulated to the filtration cell in a cross-flow mode then returned the feed reservoir. When required, the trapped air was removed through the air vent line. The permeate was collected in the permeate reservoir on a digital balance and its flux was calculated from the permeate mass.

3.1.2.4. Microalgae

Green microalgae strain *Scenedesmus* sp. (UTS-LD), isolated in Australia by the University of Technology Sydney (UTS), was used in this study. *Scenedesmus* sp. occurs in a group of four cells called a coenobium, each coenobium has a comb shape of approximately 3–5 µm in width and 12 µm in length (Fig.3.2). *Scenedesmus* sp. cells have a zeta potential of −23.2 ± 1.3 mV. The culture of *Scenedesmus* sp. was preserved at the Algae Production Facility at UTS, using MLA. It was cultivated in laboratory conditions using pilot scale photobioreactors of 120–350 L as described in a previous study [31].

3.1.2.5. Effects of the ZnO coatings on the performance of the SST membrane

The influence of the ZnO coatings on SST membrane performance was studied by measuring the permeation flux rates of Milli-Q water and microalgal solutions, as well as the rejection rate of microalgae with and without coating. The flux was determined for 1 h, the feed flow was 200 mL/min, while the pressure for the permeation of the algal solution was kept at 1000 Pa. All the microalgae filtration was performed at the same microalgal biomass concentration of 0.7 mg/mL (OD_{680nm} of 0.4 for *Scenedesmus* sp.). All filtration experiments were conducted in triplicate, and the variability of data will be presented by error bars. To fully recover fouled membranes, each was rinsed with water and then sonicated for 30 min. in isopropyl alcohol (IPA), followed by 15 min. of sonication in Milli-Q water. The flux (J), the permeability (permeance) (P), and rejection rate (R) are calculated by the following equations:

$$J = \frac{V}{At} \quad \text{(Eq. 3.1)}$$

$$P = \frac{J}{Dp} \quad \text{(Eq. 3.2)}$$

$$R = \left(1 - \frac{C_p}{C_f}\right) \times 100\% \qquad \text{(Eq. 3.3)}$$

where V is the volume of permeate, A is the effective filtration area, t filtration time, Dp is the trans-membrane pressure, R is the rejection rate, C_f and C_p are the concentrations of the feed solution and permeate solution, respectively. Both C_f and C_p were measured by OD_{680nm}.

3.1.2.6. Recovery of SST membranes by photocatalysis

For all membranes in this study, Milli-Q water was initially used to determine the clean water flux. Milli-Q water was then replaced with a microalgae solution to establish the membrane fouling profile over 1 hour as illustrated in Figure 3.3. At the end of the fouling experiment, the membrane was removed from the filtration cell and rinsed to remove the cake layer. This rinsing process involved agitating the membrane in Milli-Q water for 3 minutes. To determine the effectiveness of membrane cleaning by UV light irradiation, the membrane was removed from the cell, rinsed again for 3 minutes with Milli-Q water, and then placed at a distance of 5 cm directly under a UV LED source for 30 minutes. The UV light source with the main emission at 365 nm wavelength (9 W/m^2 intensity) was chosen to enhance the optical absorption of the ZnO coating. UV sources with similar spectral characteristics have previously been used for photoactivation of modified membranes [28, 32]. After UV irradiation, the membrane was placed back into the filtration cell and Milli-Q water was also used to determine the clean water flux. The recovered flux was calculated using Eq. (3.1) and Eq. (3.2).

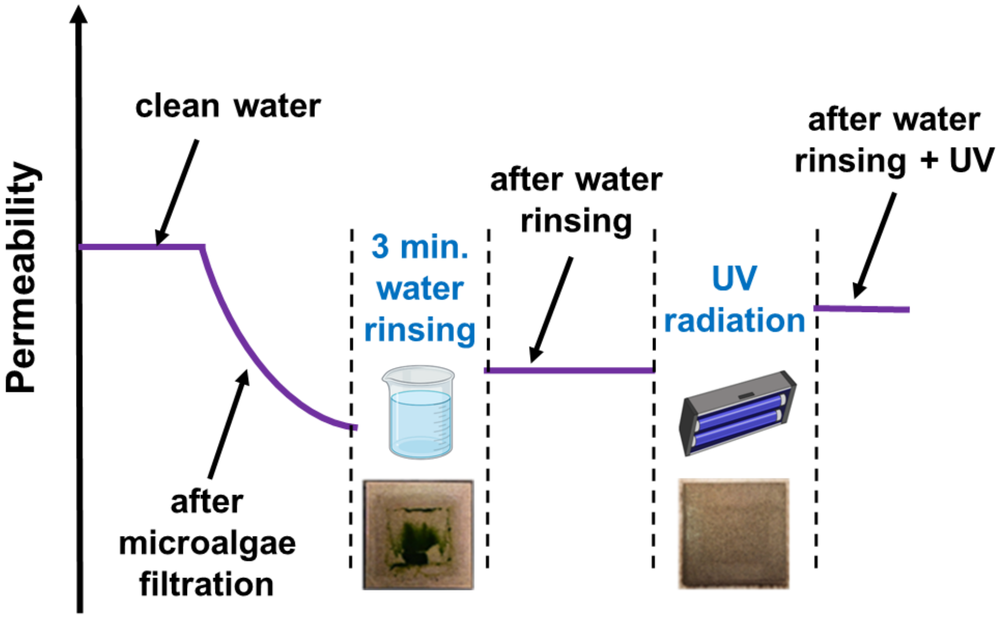

Figure 3.3. Schematic diagram of the ZnO-coated SST membrane cleaning protocol.

3.1.3. Results and discussions

3.1.3.1. Structural properties of ZnO-coated SST membranes

Coating the membrane with ZnO and Zn films does not significantly change the pore structure of the membrane as shown in the SEM images. This is attributed to the relatively large pore size of the SST membrane substrate (average pore size ~ 10 μm), which exceeds the thickness of the deposited coatings (Figure 3.4a). The presence of Zn in the coating layer on the SST substrate is confirmed by the EDS spectra of the membrane surface that show characteristic Zn X-ray peaks (Figure 3.4b). The EDS spectra also reveals Fe, Cr, Ni and Ti from the SST substrate. EDS elemental maps of the ZnO-SST in Figure 3.4c show uniform distribution of Zn over the SST base. Measurement of coating thickness using profilometer on a flat glass slide that is half-coated with a ZnO or Zn layer under the same deposition conditions reveals a thickness of 820 and 120 nm for the ZnO-SST and Zn-SST membrane, respectively (Figure 3.4d). This difference in the ZnO and Zn coating thicknesses can explain stronger Zn peaks in the EDS spectrum from the ZnO-SST membrane compared to the Zn-SST membrane. Both the ZnO-SST and Zn-SST membranes are highly porous with an average pore size of about 10 µm. It is worth noting that no visible changes were observed in the ZnO coating after applying the cleaning procedure involving IPA and ultrasonication.

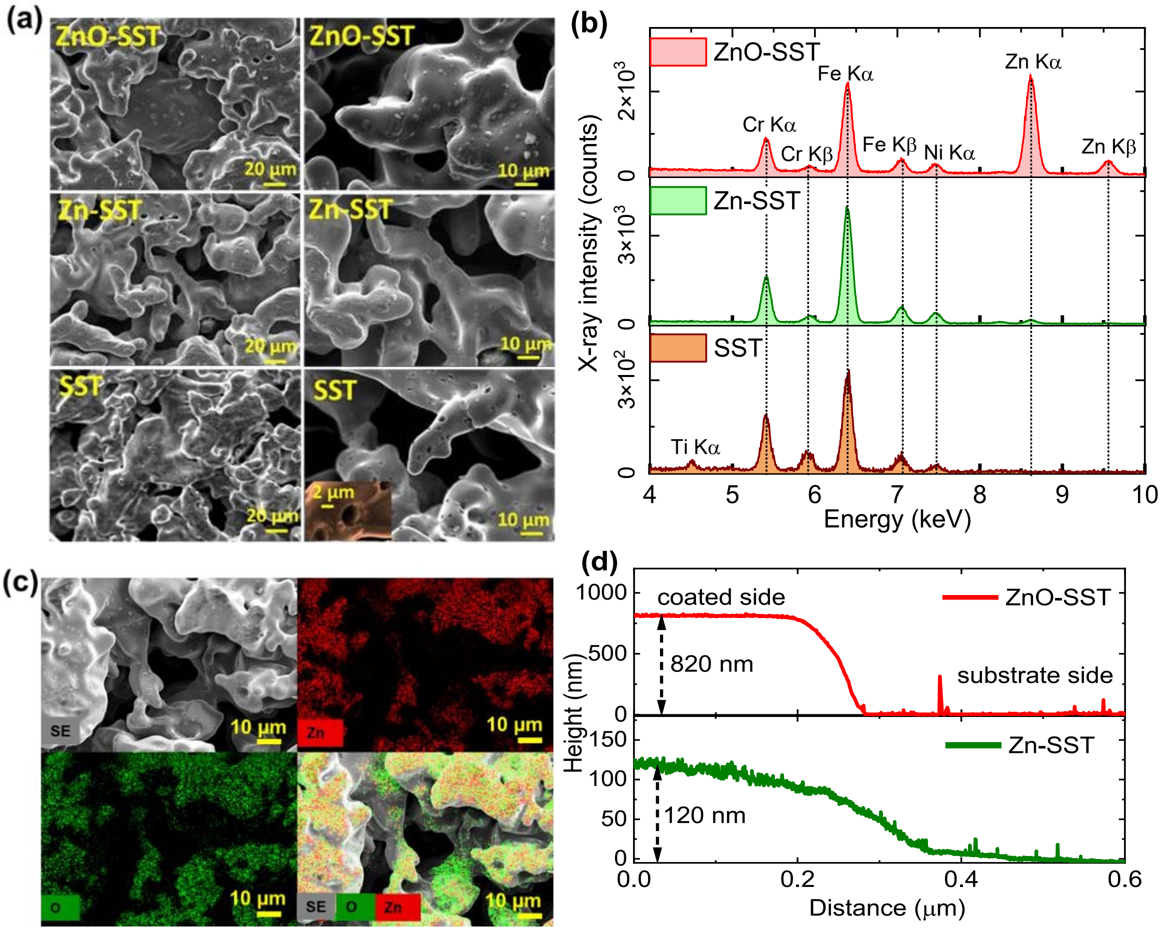

Figure 3.4. (a) SEM images of the SST, Zn-SST and ZnO-SST membranes; (b) EDS spectra of the ZnO-SST and Zn-SST membrane and the SST base. (c) EDS elemental maps of ZnO-SST coating showing ZnO on the surface. (d) Surface profiles showing the coating thickness of the ZnO and Zn coating films, respectively.

Figure 3.5a shows the XRD pattern of ZnO-coated membranes. The XRD pattern of the ZnO-SST reveals characteristics of the hexagonal wurtzite ZnO with all the diffraction peaks indexed to (100), (002), (101), (102), (110), (103), (112), and (201) planes according to the reference data to JCPDS 36-1451 [33]. On the other hand, only three weak peaks corresponding to (002), (101) and (102) planes are observed in the Zn-SST membrane. This could be due to the Zn-SST membrane having a thinner ZnO coating layer and hence lower crystallinity [34]. The optical properties of the ZnO coating layer were also investigated using UV-Vis spectrometer (Figure 3.5b). In this analysis, an optically transparent glass substrate is positioned next to the SST membrane during the deposition inside the disposition chamber, and hence a coated ZnO layer with the same thickness deposited under identical conditions. Both ZnO-SST and Zn-SST coatings exhibit high transparency in the visible region, with a sharp absorption edge around 390 nm, indicating strong light absorption in the UV region. The absorption fluctuation observed in the ZnO spectrum is due to thin film interference. The Tauc plot (Figure 3.5c), yields a bandgap of 3.21 ± 0.01 eV and 3.25 ± 0.01 for the ZnO-SST and Zn-SST coatings, respectively. The narrower bandgap of the ZnO-SST coating leads to stronger optical absorption of and higher photocatalytic activity in the visible range and hence better photocatalytic anti-fouling behaviour.

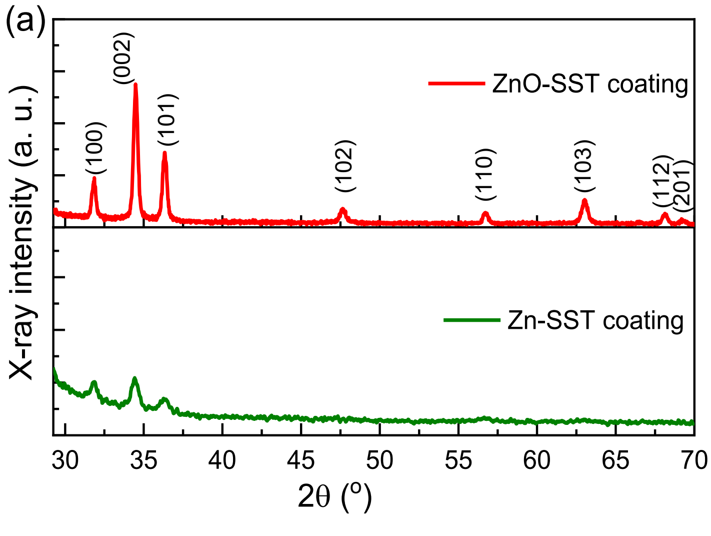

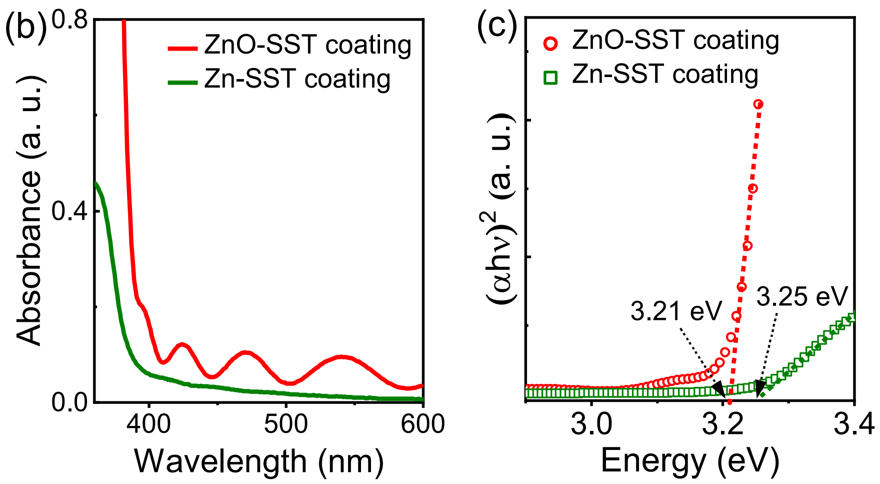

Figure 3.5. (a) XRD patterns of the ZnO-SST and Zn-SST coatings. (b) Optical absorption spectra of the ZnO-SST and Zn-SST coatings. (c) The Tauc plot for the coatings yielding the direct bandgaps shown in the graph.

The surface chemistry of the ZnO membrane is analyzed by XPS. Figure 3.6a presents the survey spectrum of the ZnO-SST membrane, showing photoemission and Auger peaks associated with Zn and O in the ZnO coating (a small C 1s peak is due to adventitious carbon). The depth-dependent chemical state of the ZnO coating is investigated by using two different photon energies of 1486.6 and 650 eV, which correspond to a probe depth of ~ 6 and 2 nm, respectively [35]. Deconvolution of the high-resolution O 1s spectra, shown in Figure 3.6b, is conducted using three fitted peaks corresponding to three different chemical states of oxygen: O^{2-} ions (O-Zn) in the fully coordinated ZnO at a binding energy of 530.6 eV, O^{2-} with a nearby oxygen vacancy (V_O) at 532.0 eV, and surface hydroxyl groups (Zn-OH) at 533.0 eV [36]. Notably, the V_O/O-Zn peak intensity ratio is found to be 0.21 and 0.49 for the top 6 nm and 2 nm layers of the coating, respectively, indicating a high density of V_O on the ZnO-SST surface. These surface V_O defects can attract water molecules and increase the wettability of the ZnO coating [37, 38]. Figure 3.6c shows the Zn 2p spectrum of the ZnO-SST coating. The spectrum shows the characteristic doublet peaks with binding energies of 1021.6 eV (Zn $2p_{3/2}$) and 1044.7 eV (Zn $2p_{1/2}$) with spin-orbit splitting energy of 23.1 eV, manifesting the Zn^{+2} oxidation state in the ZnO coating [39]. The XPS analysis of the Zn-SST coating shows its behaviour is qualitatively similar (Supplementary Data, Figure 3.10).

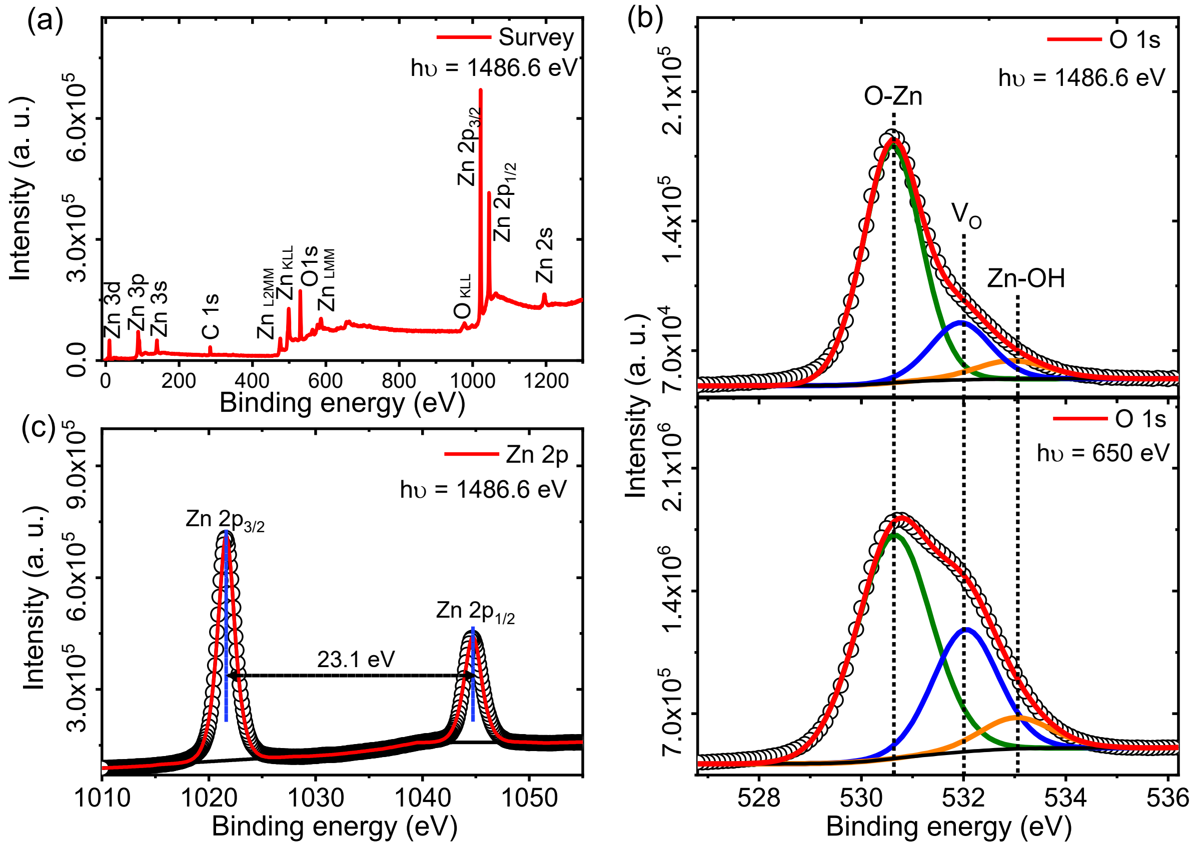

Figure 3.6. (a) XPS survey spectrum of the ZnO-SST coating, showing peaks associated with Zn, O in the coating and adventitious C. (b) High-resolution O 1s spectra of ZnO-SST coating, collected at two photon energies of 1486.6 and 650 eV, which correspond to a probe depth of ~ 6 and 2 nm, respectively. (c) Zn 2p spectrum of the coating, showing the characteristic doublet peaks of Zn $2p_{3/2}$ and Zn $2p_{1/2}$.

3.1.3.2. Membrane hydrophilicity

The hydrophilicity of the SST and the ZnO-coated membranes is investigated by contact angle measurement (Figure 3.6a). The uncoated SST membrane shows a hydrophobic surface with a contact angle of 140° (Figure 3.7a). By contrast, after ZnO or Zn coating, the membranes becomes significantly more hydrophilic with a contact angle of 65 and 68°, respectively.

Changes in hydrophobicity after coating can be attributed to the presence of the hydroxyl —OH group on the ZnO surface that can interact with water molecules [40]. The membrane pure water permeate flux of the uncoated SST membrane was stable at around 2.7×10^5 $L.m^{-2}.h^{-1}.bar^{-1}$ over 60 minutes (Figure 3.7b). Corresponding to the improvement in surface hydrophilicity, the ZnO-SST and Zn-SST membranes also show a significantly improved permeate flux at about 6.2×10^5 $L.m^{-2}.h^{-1}.bar^{-1}$. The permeability (permeance) remain constant for both the Zn-SST, and ZnO-SST membranes throughout the 60-minutes filtration duration, indicating the stability of the coating layer. Although the coating layer of the ZnO-SST membrane (0.8 μm) is thicker than that of the Zn-SST membrane (0.12 μm), both the membranes are highly porous with pore size of approximately 10 μm (Figure 3.4). Consequently, they have comparable water permeability (Figure 3.7b).

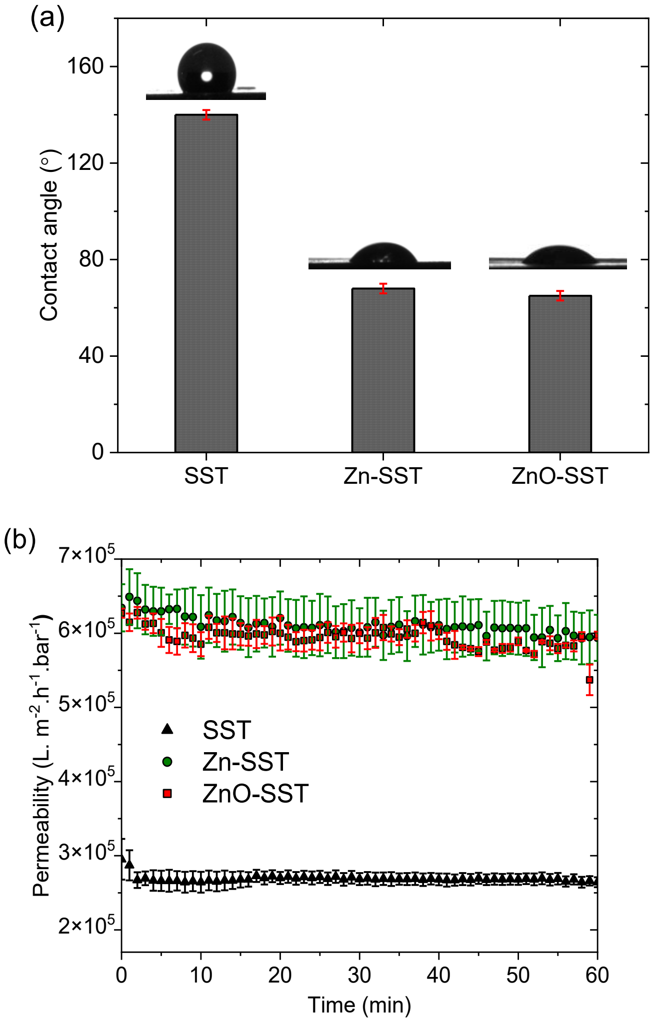

Figure 3.7. (a) Photos of the water droplet on the SST, Zn-SST, and ZnO-SST membranes with the corresponding contact angle displayed in the column graph. (b) The permeate flux of the pure water through SST, Zn-SST, and ZnO-SST membranes. Error bars show the standard deviation obtained from three replicate experiments.

3.1.3.3. Microalgae filtration performance

The base SST, Zn-SST and ZnO-SST membranes show similar filtration profiles for preconcentrating *Scenedesmus* sp. at the initial biomass concentration of 0.7 g/L (Figure 3.8a), albeit the apparent difference in the initial permeability as discussed above. The decrease in the permeate flux over filtration time for all three membranes is due to the accumulation of microalgae on the membrane surface. The ZnO-SST membrane exhibited the highest initial flux during the first 10 minutes, possibly due to a slight reduction in pore size caused by the thicker coating. This was followed by the Zn-SST membrane, while the uncoated SST membrane showed the lowest initial flux. The initial permeate flux increases by 45% and 100% for the Zn-SST and ZnO-SST membranes, respectively. Moreover, the coated membranes exhibits a slower permeate flux decline over time due to their high hydrophilicity, consistent with the notion that higher surface hydrophilicity facilitates membrane fouling prevention [41]. After 20 mins of filtration, all three membranes have a similar permeability due to the deposition of microalgae, forming a cake layer on the membrane surface, which itself acts as a secondary filtration layer during the initial filtration stage [42, 43]. After 40 minutes, the permeate flux of the membranes are stabilized at around 4.0×10^3 $L.m^{-2}.h^{-1}.bar^{-1}$, which could be due to the relatively stable adsorption of the microalgal cells caused by the cross-flow shearing on the membrane surface [44]. All three membranes show high microalgae rejection of above 94% (Figure 3.8b). The membrane coating results in a more hydrophilic surface and higher water permeability compared with the uncoated membrane. These changes in membrane surface properties could have contributed to the small but discernible variation in microalgae rejection as shown in Figure 3.8b. The ZnO-SST membrane showed the highest microalgae rejection of 99.7%, indicating that it is suitable for pre-concentration prior to harvesting.

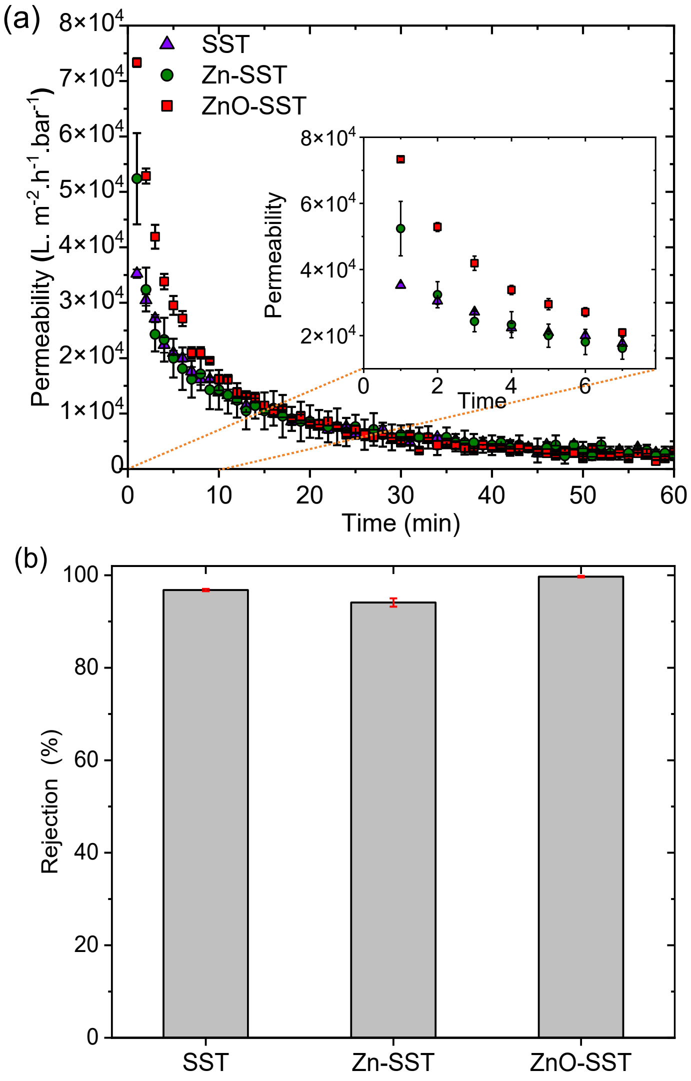

Figure 3.8. (a) Variations of the permeate flux for the base SST, Zn-SST and ZnO-SST membranes during the filtration of the microalgae solution. (b) The rejection rate of microalgae for the membranes. Error bars show the standard deviation obtained from three replicate experiments.

3.1.3.4. Photocatalytic cleaning properties of the ZnO-coated SST membranes

The self-cleansing property of the ZnO-coated SST membranes is demonstrated in Figure 3.9a. For all membranes, water cleaning alone could only result in up to 30% flux (permeability) recovery. No further flux recovery could be observed when the uncoated SST membrane was irradiated with UV for 30 mins. This result confirms that UV irradiation has no effect on degrading the biofilm nor increasing the hydrophilicity of the SST membrane. On the other hand, water cleaning followed by 30 minutes UV radiation resulted in a significant permeability improvement of the ZnO and Zn coated membranes. The permeability recovery of the ZnO-SST membrane was 60%, which is higher than that of the Zn-SST membrane. This improvement is attributed to the higher photocatalytic activity of ZnO, which is facilitated by its narrower bandgap and more efficient generation of reactive species under UV illumination. These results confirm photocatalytic activity and effective self-cleansing performance of the coated membranes. The Zn-SST and ZnO-SST membranes both exhibit endurance over three repetitive filtration cycles with stable permeability recovery of about 60% (standard deviation of 6%). Results in Figure 3.9a confirm the stability of the ZnO coating layer and self-cleansing performance of the membrane. A higher power UV light source (intensity 190 W/m^2) and longer irritation times were also investigated; however, no further improvement could be observed. This is possibly because self-cleansing is driven mostly by photocatalysis at the membrane surface with limited UV penetration into deep membrane pores. Successive filtration and cleaning cycles with UV irradiation show that the permeate flux of water can be restored to approximately 75% after each cycle (Supplementary Data, Figure 3.11). Although the results are promising, self-cleansing was unable to completely recover the membrane flux. Thus, addition research is necessary to further improve the membrane cleaning efficiency, possibly by increasing the strength of UV radiation and ZnO density on the membrane surface.

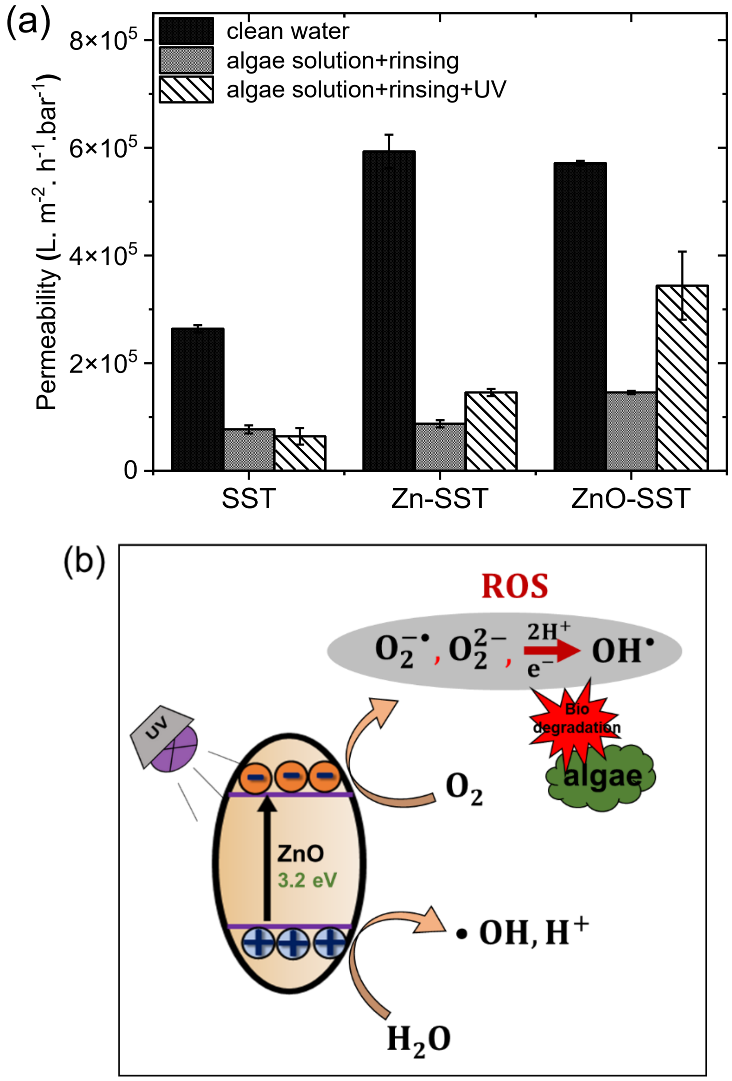

Figure 3.9. (a) The permeate water flux of the SST, Zn-SST, and ZnO-SST membranes (i) before fouling, (ii) after fouling and cleaning with water, and (iii) after fouling and cleaning with water and UV irradiation. Error bars show the standard deviation of three replicate experiments. (b) Proposed photocatalytic self-cleansing mechanism for the ZnO-coated SST membrane.

The self-cleaning capability of the coated SST membranes under UV light irradiation is illustrated in Figure 3.9b. Since the energy of UV light (3.4 eV) is greater than the bandgap of the coating layer (3.25 eV for Zn-SST and 3.21 eV for ZnO-SST), free electrons and holes can be generated. The photogenerated holes have a strong ability to oxidize organic compounds and generate radicals, such as superoxides ($O_2^{-\bullet}$), peroxides (O_2^{2-}), and hydroxides ($OH^{\bullet}$); these radical species are highly reactive and can degrade organic materials from microalgae [45] to ensure effective cleaning. It is noteworthy that these radical species can also penetrate to the membrane pores for effective cleaning. Optical microscope images of the coated SST membranes before and after cleaning with water and UV light irradiation are presented in Supplementary Data, Figure 3.12. Following the cleaning procedure, residual microalgae were still observed on the Zn-SST membrane, whereas no visible fouling layer was detected on the surface of the ZnO-SST membrane. This underscores the economic potential of ZnO coating for self-cleansing to significantly improve membrane cleaning efficiency and durability. As a result, the outcome from this research will lead to a reduction in operational and maintenance costs.

3.1.4. Conclusion

Durable ZnO-coated SST membranes for microalgae pre-concentration have been successfully fabricated using two surface-coating approaches, the first involving post-growth oxidation of a sputtered Zn film and the second involving reactive sputter deposition of a ZnO coating. Surface characterization of the membrane coatings reveals a homogeneous, crystalline ZnO layer on the membrane surface. It is found that the ZnO coating fabricated by reactive sputter deposition has a larger thickness and a narrower optical bandgap than the ZnO layer synthesized via post-growth oxidation. Contact angle measurements show the transformation of the SST membrane from a hydrophobic to a hydrophilic state due to the ZnO coating, which leads to an improvement in the permeate water flux by more than twofold. The high hydrophilicity of the ZnO-SST membranes results in an increase in the permeate flux of the microalgae solution by up 100% and a slower flux decline over filtration time. Moreover, the ZnO-coated SST membranes can be effectively recovered by water rinsing and UV light irradiation by exploiting the UV photocatalytic activity of the ZnO coating. After UV irradiation of a completely fouled ZnO-coated SST membrane for 30 minutes, the permeate flux can be recovered to 60% of the original value.

CRediT authorship contribution statement

Amar Salih: Conceptualization, Investigation, Experimental setup, Data curation, samples characterization, Formal analysis, Writing − original draft. **Lisa Aditya:** Experimental setup, Data curation. **Fatima Matar:** samples characterization. **Long D. Nghiem:** Writing – review & editing, Methodology, Supervision, Formal analysis. **Cuong Ton-That:** Writing – review & editing, Supervision, Formal analysis.

Acknowledgements

This research was partly undertaken on the Soft X-ray Spectroscopy beamline at the Australian Synchrotron, Victoria, Australia. The work was supported under Australian Research Council (ARC) Discovery Project funding scheme (project DP210101146) and the ACT node of the Australian National Fabrication Facility (ANFF). The authors would like to thank Anton Tadich, James Bishop and Herbert Yuan for technical support.

Supplementary data

Supplementary data to this paper can be found in the appendix: A

3.1.5. References

[1] Q.V. Ly, L. Cui, M.B. Asif, W. Khan, L.D. Nghiem, Y. Hwang, Z. Zhang, Membrane-based nanoconfined heterogeneous catalysis for water purification: A critical review, Water Research (2023) 119577.

[2] Y. He, D.M. Bagley, K.T. Leung, S.N. Liss, B.-Q. Liao, Recent advances in membrane technologies for biorefining and bioenergy production, Biotechnology advances 30(4) (2012) 817-858.

[3] S.F. Ahmed, M. Mofijur, M. Nahrin, S.N. Chowdhury, S. Nuzhat, M. Alherek, N. Rafa, H.C. Ong, L. Nghiem, T. Mahlia, Biohydrogen production from wastewater-based microalgae: Progresses and challenges, International Journal of Hydrogen Energy 47(88) (2022) 37321-37342.

[4] L.N. Nguyen, M.T. Vu, H.P. Vu, M.A.H. Johir, L. Labeeuw, P.J. Ralph, T. Mahlia, A. Pandey, R. Sirohi, L.D. Nghiem, Microalgae-based carbon capture and utilization: A critical review on current system developments and biomass utilization, Critical Reviews in Environmental Science and Technology 53(2) (2023) 216-238.

[5] M. Branco-Vieira, T. Mata, A. Martins, M. Freitas, N. Caetano, Economic analysis of microalgae biodiesel production in a small-scale facility, Energy Reports 6 (2020) 325-332.

[6] O.M. Adeniyi, U. Azimov, A. Burluka, Algae biofuel: current status and future applications, Renewable and sustainable energy reviews 90 (2018) 316-335.

[7] A. Ortega, N.R. Geraldi, I. Alam, A.A. Kamau, S.G. Acinas, R. Logares, J.M. Gasol, R. Massana, D. Krause-Jensen, C.M. Duarte, Important contribution of macroalgae to oceanic carbon sequestration, Nature Geoscience 12(9) (2019) 748-754.

[8] L. Aditya, H.P. Vu, L.N. Nguyen, T.I. Mahlia, N.B. Hoang, L.D. Nghiem, Microalgae enrichment for biomass harvesting and water reuse by ceramic microfiltration membranes, Journal of Membrane Science 669 (2023) 121287.

[9] I. Di Termini, A. Prassone, C. Cattaneo, M. Rovatti, On the nitrogen and phosphorus removal in algal photobioreactors, Ecological Engineering 37(6) (2011) 976-980.

[10] C. Hepburn, E. Adlen, J. Beddington, E.A. Carter, S. Fuss, N. Mac Dowell, J.C. Minx, P. Smith, C.K. Williams, The technological and economic prospects for CO2 utilization and removal, Nature 575(7781) (2019) 87-97.

[11] N. Hossain, M. Hasan, T. Mahlia, A. Shamsuddin, A. Silitonga, Feasibility of microalgae as feedstock for alternative fuel in Malaysia: A review, Energy Strategy Reviews 32 (2020) 100536.

[12] M. Zheng, Y. Yang, S. Qiao, J. Zhou, X. Quan, A porous carbon-based electro-Fenton hollow fiber membrane with good antifouling property for microalgae harvesting, Journal of Membrane Science 626 (2021) 119189.

[13] Z. Zhao, B. Liu, A. Ilyas, M. Vanierschot, K. Muylaert, I.F. Vankelecom, Harvesting microalgae using vibrating, negatively charged, patterned polysulfone membranes, Journal of Membrane Science 618 (2021) 118617.

[14] B. Malczewska, A. Żak, Structural changes and operational deterioration of the Uf polyethersulfone (Pes) membrane due to chemical cleaning, Scientific reports 9(1) (2019) 422.

[15] D. Xu, Y. Qin, Y. Fang, M. Chen, X. Li, J. Cai, Stainless steel membranes for harvesting cyanobacteria: Performance, fouling and cleaning, Bioresource Technology 319 (2021) 124143.

[16] A. Ahmad, N.M. Yasin, C. Derek, J. Lim, Chemical cleaning of a cross-flow microfiltration membrane fouled by microalgal biomass, Journal of the Taiwan Institute of Chemical Engineers 45(1) (2014) 233-241.

[17] N. Daneshvar, D. Salari, A. Khataee, Photocatalytic degradation of azo dye acid red 14 in water on ZnO as an alternative catalyst to TiO_2, Journal of photochemistry and photobiology A: chemistry 162(2-3) (2004) 317-322.

[18] K.M. Lee, C.W. Lai, K.S. Ngai, J.C. Juan, Recent developments of zinc oxide based photocatalyst in water treatment technology: a review, Water research 88 (2016) 428-448.

[19] K. Qi, B. Cheng, J. Yu, W. Ho, Review on the improvement of the photocatalytic and antibacterial activities of ZnO, Journal of Alloys and Compounds 727 (2017) 792-820.

[20] M. Sheikh, M. Pazirofteh, M. Dehghani, M. Asghari, M. Rezakazemi, C. Valderrama, J.-L. Cortina, Application of ZnO nanostructures in ceramic and polymeric membranes for water and wastewater technologies: a review, Chemical Engineering Journal 391 (2020) 123475.

[21] S. Heinonen, J.-P. Nikkanen, E. Huttunen-Saarivirta, E. Levänen, Investigation of long-term chemical stability of structured ZnO films in aqueous solutions of varying conditions, Thin Solid Films 638 (2017) 410-419.

[22] Z.-Q. Huang, K. Chen, S.-N. Li, X.-T. Yin, Z. Zhang, H.-T. Xu, Effect of ferrosoferric oxide content on the performances of polysulfone–ferrosoferric oxide ultrafiltration membranes, Journal of Membrane Science 315(1-2) (2008) 164-171.

[23] M. Storms, A.J. Kadhem, S. Xiang, M. Bernards, G.J. Gentile, M.M. Fidalgo de Cortalezzi, Enhancement of the fouling resistance of Zwitterion coated ceramic membranes, Membranes 10(9) (2020) 210.

[24] A. Di Mauro, M. Zimbone, M.E. Fragalà, G. Impellizzeri, Synthesis of ZnO nanofibers by the electrospinning process, Materials Science in Semiconductor Processing 42 (2016) 98-101.

[25] R. Goei, T.-T. Lim, Ag-decorated TiO_2 photocatalytic membrane with hierarchical architecture: Photocatalytic and anti-bacterial activities, Water research 59 (2014) 207-218.

[26] C. Li, W. Sun, Z. Lu, X. Ao, C. Yang, S. Li, Systematic evaluation of TiO_2-GO-modified ceramic membranes for water treatment: Retention properties and fouling mechanisms, Chemical Engineering Journal 378 (2019) 122138.

[27] K.-H. Park, P.-F. Sun, E.H. Kang, G.D. Han, B.J. Kim, Y. Jang, S.-H. Lee, J.H. Shim, H.-D. Park, Photocatalytic anti-biofouling performance of nanoporous ceramic membranes treated by atomic layer deposited ZnO, Separation and Purification Technology 272 (2021) 118935.

[28] L.L. Coelho, M. Grao, T. Pomone, M. Ratova, P. Kelly, M. Wilhelm, R.d.F.P.M. Moreira, Photocatalytic microfiltration membranes produced by magnetron sputtering with self-cleaning capabilities, Thin Solid Films 747 (2022) 139143.

[29] J. Kacprzyńska-Gołacka, M. Łożyńska, W. Barszcz, S. Sowa, P. Wieciński, E. Woskowicz, Microfiltration membranes modified with composition of titanium oxide and silver oxide by magnetron sputtering, Polymers 13(1) (2020) 141.

[30] S. Khamseh, F.A. Davani, A. Samimi, The effects of RF-sputtered TiO_2 top layer on pore structure of composite ceramic membranes, Surface and Coatings Technology 258 (2014) 1256-1258.

[31] H.P. Vu, L.N. Nguyen, M.T. Vu, L. Labeeuw, B. Emmerton, A.S. Commault, P.J. Ralph, T. Mahlia, L.D. Nghiem, Harvesting Porphyridium purpureum using polyacrylamide polymers and alkaline bases and their impact on biomass quality, Science of the Total Environment 755 (2021) 142412.

[32] H.N.C. Dharma, J. Jaafar, N. Widiastuti, H. Matsuyama, S. Rajabsadeh, M.H.D. Othman, M.A. Rahman, N.N.M. Jafri, N.S. Suhaimin, A.M. Nasir, A review of titanium dioxide (TiO_2)-based photocatalyst for oilfield-produced water treatment, Membranes 12(3) (2022) 345.

[33] P. Basnet, D. Samanta, T. Inakhunbi Chanu, J. Mukherjee, S. Chatterjee, Assessment of synthesis approaches for tuning the photocatalytic property of ZnO nanoparticles, SN Applied Sciences 1 (2019) 1-13.

[34] P. Shewale, G. Agawane, S. Shin, A. Moholkar, J. Lee, J. Kim, M. Uplane, Thickness dependent H2S sensing properties of nanocrystalline ZnO thin films derived by advanced spray pyrolysis, Sensors and actuators B: chemical 177 (2013) 695-702.

[35] M.P. Seah, W. Dench, Quantitative electron spectroscopy of surfaces: A standard data base for electron inelastic mean free paths in solids, Surface and interface analysis 1(1) (1979) 2-11.

[36] L. Jiang, J. Li, K. Huang, S. Li, Q. Wang, Z. Sun, T. Mei, J. Wang, L. Zhang, N. Wang, Low-temperature and solution-processable zinc oxide transistors for transparent electronics, ACS omega 2(12) (2017) 8990-8996.

[37] H. Hu, H.-F. Ji, Y. Sun, The effect of oxygen vacancies on water wettability of a ZnO surface, Physical Chemistry Chemical Physics 15(39) (2013) 16557-16565.

[38] H.-P. Chang, E.-D. Chu, Y.-T. Yeh, Y.-C. Wu, F.-Y. Lo, W.-H. Wang, M.-Y. Chern, H.-C. Chiu, Influence of oxygen vacancies on the frictional properties of nanocrystalline zinc oxide thin films in ambient conditions, Langmuir 33(34) (2017) 8362-8371.

[39] R. Al-Gaashani, S. Radiman, A. Daud, N. Tabet, Y. Al-Douri, XPS and optical studies of different morphologies of ZnO nanostructures prepared by microwave methods, Ceramics International 39(3) (2013) 2283-2292.

[40] H. Ennaceri, L. Wang, D. Erfurt, W. Riedel, G. Mangalgiri, A. Khaldoun, A. El Kenz, A. Benyoussef, A. Ennaoui, Water-resistant surfaces using zinc oxide structured nanorod arrays with switchable wetting property, Surface and Coatings Technology 299 (2016) 169-176.

[41] D. Rana, T. Matsuura, Surface modifications for antifouling membranes, Chemical reviews 110(4) (2010) 2448-2471.

[42] A. Ahmad, N.M. Yasin, C. Derek, J. Lim, Harvesting of microalgal biomass using MF membrane: kinetic model, CDE model and extended DLVO theory, Journal of membrane science 446 (2013) 341-349.

[43] F. Qu, H. Liang, J. Tian, H. Yu, Z. Chen, G. Li, Ultrafiltration (UF) membrane fouling caused by cyanobateria: Fouling effects of cells and extracellular organics matter (EOM), Desalination 293 (2012) 30-37.

[44] K. Ebert, D. Fritsch, J. Koll, C. Tjahjawiguna, Influence of inorganic fillers on the compaction behaviour of porous polymer based membranes, Journal of Membrane Science 233(1-2) (2004) 71-78.

[45] M. Rezayian, V. Niknam, H. Ebrahimzadeh, Oxidative damage and antioxidative system in algae, Toxicology reports 6 (2019) 1309-1313.

3.1.6. Appendix A: Additional surface chemistry and membranes photocatalytic cleaning data

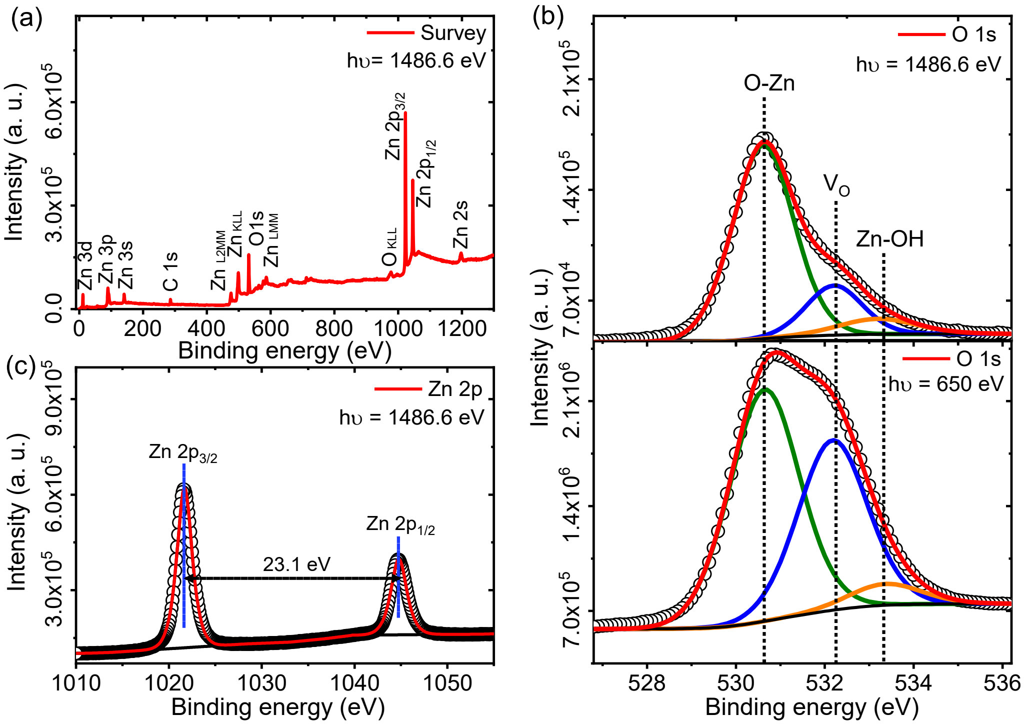

Figure 3.10. (a) XPS survey spectrum of the Zn-SST coating collected at a photon energy of 1486.6 eV showing photoemission and Auger peaks corresponding to Zn and O in the ZnO film (the small C 1s peak arises from adventitious carbon). (b) Depth-dependent O 1s XPS spectra of the Zn-SST coating acquired at two photon energies of 1486.6 eV and 650 eV, which correspond to a sampling depth of ~6 and 2 nm, respectively. The spectra are fitted with three Gaussian peaks: O^{2-} ions (O-Zn) in the fully coordinated ZnO, O^{2-} with a nearly oxygen vacancy (V_O), surface hydroxyl (Zn-OH) at binding energies of 530.6, 532.2, and 533.3 eV, respectively. The V_O/O-Zn peak intensity ratio is 0.20 and 0.73 for the top 6 and 2 nm layer respectively, indicating a high density of V_O defects on the coating surface. (c) High resolution Zn 2p spectrum of the film, showing the characteristic doublet peaks with binding energies of 1021.6 (Zn $2p_{3/2}$) and 1044.7 eV (Zn $2p_{1/2}$) with spin-orbit splitting energy of 23.1 eV, manifesting the Zn^{+2} oxidation state.

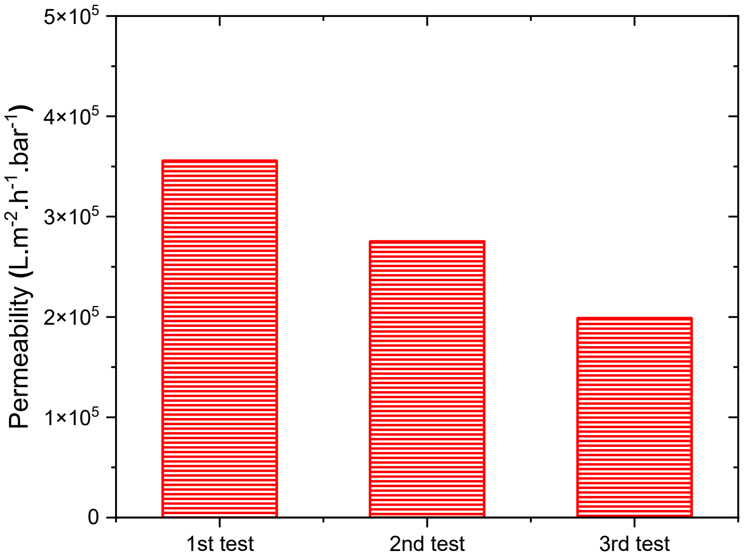

Figure 3.11. Water permeation performance of the ZnO-SST membrane in three successive tests after complete fouling and cleaning with water and UV light irradiation. The results show that the permeate water flux can be restored to more than 75% of the original by this cleaning method.

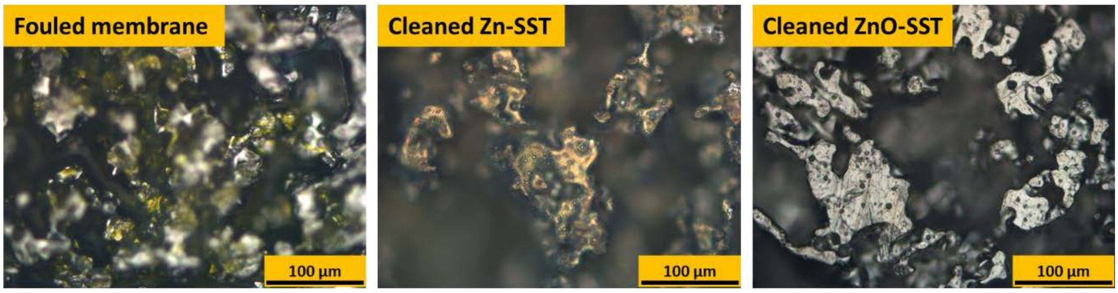

Figure 3.12. Optical microscope images of a fouled ZnO-SST membrane, and cleaned Zn-SST and ZnO-SST membranes after 30 minutes of UV light irradiation and water rinsing.

3.2. Photocatalytic Self-Cleansing ZnO-coated Ceramic Membranes for Preconcentrating Microalgae

Abstract

Microalgae present strong potential for biofuel and bioproduct production; however, efficient harvesting methods remain a critical challenge to enhancing the economic competitiveness of microalgal products. This study introduces a simple approach for fabricating self-cleaning microfiltration membranes tailored for *Scenedesmus* sp. microalgae solutions by coating alumina substrates with ZnO. The ZnO layer was deposited using reactive magnetron sputtering and the functional properties of the membrane were tailored through controlled coating thicknesses. Surface characterization confirmed the formation of a uniform, crystalline ZnO layer. The solar light absorption of the ZnO-coated membrane was found to vary with coating thickness. The water contact angle of the membrane decreased from 80° to 42° after ZnO coating, demonstrating a substantial increase in hydrophilicity. While both uncoated and ZnO-coated alumina membranes initially exhibited a permeate flux of about 55 $L\cdot m^{-2}\cdot h^{-1}$ (LMH), the ZnO-coated membranes demonstrated superior fouling resistance, with only a 5% flux decline after three filtration cycles compared to a 32% reduction in uncoated membranes. Under optimal conditions, the ZnO-coated membranes achieved full flux recovery within 30 minutes of solar simulator exposure, highlighting their excellent photocatalytic self-cleaning capabilities. The performance of the ZnO-coated membranes remained stable over three repetitive filtration cycles and membrane recovery, with the standard deviation of <5%, confirming the durability of the ZnO coatings. These findings highlight the potential of ZnO-coated ceramic membranes as a cost-effective solution for sustainable microalgae harvesting.

Keywords: Microalgae harvesting; ZnO coating; Ceramic microfiltration membranes; Photocatalysis; Fouling control; Self-cleansing.

3.2.1. Introduction

Population growth and industrialization have improved the world economy, but they have led to a significant increase in global energy and fuel consumption. A large body of research has focussed on the development of eco-friendly energy resources to reduce reliance on fossil fuels, secure access to fresh water and mitigate global warming [1, 2]. Microalgae-derived biofuels and biochemicals have emerged as a sustainable alternative to fossil materials [3]. Microalgae are rich in proteins, carbohydrates, lipids, and nucleic acids, with lipid biomolecules such as fatty acids, triglycerides, phospholipids, and glycolipids offering a renewable source for the production of fuel and raw materials [4, 5]. However, despite their potential, microalgae refineries have not been realized at industrial scale due to the high cost of harvesting [6, 7]. Economically viable biofuel production requires efficient harvesting techniques that minimize energy and chemical consumption while enabling the recycling of water and nutrients [8]. There are currently no suitable harvesting techniques that satisfy both cost and environmental constraints for producing microalgae-derived biofuels and biochemicals [8, 9].

Current microalgae harvesting techniques, such as centrifugation and chemical flocculation, are highly energy- and chemical-intensive, contributing significantly to the overall production cost. While centrifugation is effective and fast, it incurs high operational costs. Chemical flocculation, on the other hand, is less energy-intensive but requires flocculants like cationic polymers, which can increase maintenance requirements, complicate downstream processing and limit applications due to residual chemicals [10, 11]. Recent research has demonstrated the potential of microfiltration for preconcentrating microalgae for harvesting, improving biomass recovery efficiency and cost competitiveness [12, 13]. However, previous studies also reveal that algal organic matter, consisting of extracellular and intracellular components, plays a dominant role in fouling by accumulating on the membrane surface and within pores, forming dense and irreversible fouling layers [14, 15].

Several techniques, such as membrane vibration and frequent aerated backwashing, have been developed to tackle membrane fouling caused by high biomass levels [15, 16]. Although these methods help restore membrane flux, the presence of thick extracellular polymeric materials from microalgae cells can lead to a gradual deterioration of the filtration process over time [15]. To mitigate membrane fouling effectively, incorporating and optimizing self-cleaning materials in microfiltration membranes is essential. Moreover, enhancing the membrane's wettability and introducing a surface charge can significantly reduce membrane fouling. Increasing hydrophilicity creates a hydration layer on the membrane surface, preventing direct contact between foulants and the membrane surface [17, 18]. Additionally, electrostatic repulsion can inhibit foulants from attaching to the membrane surface, thereby reducing the fouling rate and improving filtration performance [19]. These techniques can alleviate but cannot completely remove fouling, and eventually membrane cleaning is still necessary.

Advanced oxidation processes (AOP) based on photoactive materials, such as TiO_2, ZrO_2, Fe_2O_3, ZnO, and MOF, have been explored in combination with membrane filtration to degrade and remove bio-contaminants through the production of reactive oxygen species [20-23]. This approach provides a potential platform for developing self-cleansing membranes. When a semiconducting oxide material is illuminated with ultraviolet (UV) or solar light, electrons can be excited from the valence to the conduction band, generating free electron and holes. These electrons and holes can directly oxidize pollutants or interact with dissolved oxygen or OH^- ions in water to create reactive oxygen species (ROS), which degrade pollutants and organic foulants on the membrane surface [21]. Although photocatalytic degradation using metal oxides has been demonstrated for synthetic wastewater and organic compounds [24, 25], few studies have investigated the use of coated membranes for microalgae harvesting, with membrane recovery rates of ~ 60% achieved after ultraviolet irradiation cleaning [26]. While surface coatings can enhance antifouling resistance and hydrophilicity, low-quality coatings may cause particle aggregation, significantly impairing its performance [27]. Deposition techniques such as electrospinning [28], dip coating [29], sol–gel [30], atomic layer deposition [24], and pulsed laser deposition [31], have been used for membrane coating; however, most methods encounter issues like non-uniformity, fragility, and limited membrane compatibility. In contrast, sputter deposition offers distinct advantages by providing strongly adherent, uniform coatings over large areas and accommodating porous membranes with irregular or curved surfaces [32]. ZnO is an effective photocatalyst for AOP, offering superior organic degradation compared to alternatives such as TiO_2 due to its higher electron mobility and a lower valence band position, which increases the oxidation potential of hydroxyl radicals [33, 34]. Moreover, ZnO has low toxicity and is stable in aqueous environments at pH levels above 5 [35].

This study develops a self-cleaning membrane system to enhance microalgae biomass harvesting. We hypothesize that integrating a ZnO coating layer onto an alumina membrane will enable photocatalytic cleaning while reducing fouling through enhanced wettability. The approach involves incorporating a hydrophilic and photocatalytic ZnO coating onto a ceramic membrane. The ZnO layer was systematically characterized to confirm its photocatalytic functionality. The performance of the ZnO-coated membrane was evaluated for preconcentrating microalgae solutions, with key performance parameters including water permeability, flux recovery through photocatalytic self-cleaning.

3.2.2. Materials and Methods

3.2.2.1. Membrane preparation

A flat sheet ceramic membrane made of alumina (ALO) from Suzhou Dasen Electronic Material Co. (Jiangxi, China) was used. The membrane, measuring 150 mm by 100 mm, has an average pore size of 0.1 µm (according to the manufacturer). Before coating, the membrane was sequentially cleaned in an ultrasonic bath for 20 minutes using acetone, isopropanol and deionized water. After cleaning, it was dried with dry N_2 gas and stored in an airtight container. During deposition, the membrane was placed on a rotating stage approximately 10 cm from the sputtering target in a sputtering chamber, as described previously [26]. ZnO layers of varying thicknesses (200, 450, 750, and 1100 nm, denoted as T–ZnO/ALO, where T is the coating thickness) were deposited onto the membrane using direct current reactive sputtering (plasma power of 100 W) from a Zn target in a gas mixture of Ar and O_2 with a ratio of 3:1. The thickness of the ZnO coating was monitored by a quart crystal thickness monitor. Post-deposition, the ZnO-coated membranes were annealed in ambient air at 500 °C for 2 hours to improve the crystallinity of the ZnO layer. The uncoated membrane was also annealed under identical conditions and used as a control sample. Additionally, a glass slide was placed beside the membrane during deposition to obtain a ZnO film of identical thickness for optical analysis.

3.2.2.2. Membrane characterization

The ZnO-coated and uncoated ceramic membranes were characterized to evaluate their coating thickness, surface morphology, composition, crystallinity, and hydrophilic properties. X-ray diffraction (XRD) analysis was conducted using a Bruker D8 Discovery diffractometer with Cu Kα radiation. Optical absorption measurements were measured using an Agilent Cary 7000 UV-Vis spectrometer. The coating thickness was determined using a Bruker DektakXT profilometer, while hydrophilicity and contact angles were measured using an Attension optical tensiometer. Surface morphologies of the membranes were investigated with a Zeiss Supra

55VP field emission scanning electron microscope (SEM) equipped with Oxford Instruments Energy Dispersive Spectrometer (EDS). SEM images were analysed using ImageJ software to determine membrane pore sizes. The membrane surface roughness was measured using Park XE7 atomic force microscopy (AFM). X-ray photoelectron spectroscopy (XPS) data were collected at the Australian Synchrotron's Soft X-ray Spectroscopy (SXS) beamline.

3.2.2.3. *Membrane filtration performance*

The uncoated ALO and ZnO/ALO membranes were utilized in a submerged configuration (Fig. 3.13a). A plate and frame membrane module was submerged in a rectangular glass reservoir with dimensions of 45 cm in height, 20 cm in length, and 5 cm in width. A Masterflex Peristaltic pump (Cole-Parmer) was used to facilitate the clean water extraction from the membrane module. The system contained a digital pressure gauge data logger (Pressure Meter SDL700) to monitor the transmembrane pressure (TMP). Permeate water was collected in a storage tank, while water flux was measured using a digital balance (PGL 8001).

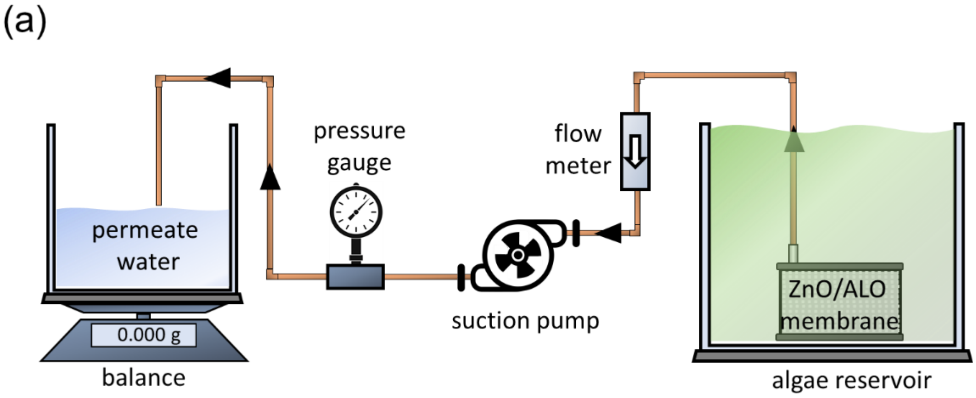

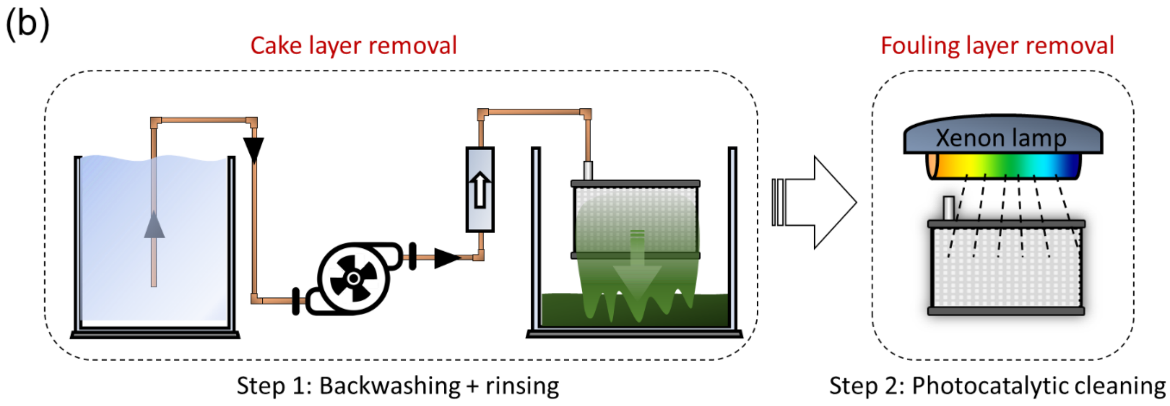

Figure 3.13. (a) Schematic diagram of the membrane filtration system, which includes a submerged membrane module, algae reservoir, flow meter, suction pump, pressure gauge, balance, and storage tank. (b) Schematic diagram of the cleaning protocol for the ZnO/ALO membrane. Step 1 entails backwashing and rinsing the membrane with permeate water to remove the cake fouling layer, followed by Step 2, which involves photocatalytic cleaning using solar irradiation.

Effects of the ZnO coating on filtration performance

The effects of the ZnO coating on the ceramic alumina membrane were investigated by measuring the TMP at a flow rate of 30 mL/min and the rejection rate of a microalgae solution for both coated and uncoated ALO membranes. The initial volume of the microalgae solution was 4.5 L, while each filtration cycle was set to recover 1 L of water. All filtration experiments were conducted in duplicate to ensure reproducibility and calculate uncertainty. Before each replicate measurement, the membranes were backwashed at a flow rate of 30 mL/min for 3 minutes to remove the cake fouling layer, followed by rinsing with tap water, 30 minutes of sonication in isopropyl alcohol (IPA), and 15 minutes of sonication in Milli-Q water. The flux (J), rejection rate (R), and flux recovery rate (FRR) are calculated by the following equations:

$$J\ (LMH) = \frac{V}{At} \qquad \text{(Eq. 1)}$$

$$R\ (\%) = \left(1 - \frac{C_p}{C_f}\right) \times 100\% \qquad \text{(Eq. 2)}$$

$$FRR\ (\%) = \left(\frac{J_c}{J_o}\right) \times 100\% \qquad \text{(Eq. 3)}$$

where V is the volume of filtered water, A is the effective filtration area, t is the filtration time, C_f and C_p are the concentrations of the feed solution and permeate solution, respectively, both measured using optical density at 680 nm ($\mathrm{OD_{680nm}}$). J_c and J_o are the flux of the cleaned and original membranes, respectively. The filtration performance of the membrane was also evaluated over three repetitive filtration cycles. After each cycle, the membrane was kept inside the algae reservoir and backwashed at a flow rate of 30 mL/min for 3 mins before starting the subsequent cycle. The TMP was monitored and recorded every minute during each filtration cycle. To investigate the effect of aeration on the permeate flux, a plastic tube connected to an air pump was placed at the bottom of the reservoir to deliver an airflow of 0.5 LPM (litre per minute) when required.

Recovery of ZnO/ALO membranes by photocatalysis

Milli-Q water was used to determine the initial clean water flux for ALO and ZnO/ALO membranes. To form a fouling layer, 1 L of the microalgae solution was filtered through the membrane at a flow rate of 30 mL/min. Two cleaning steps were performed to recover the membrane flux (Fig. 3.13b) and the recovery rate was examined after each step. The first step involved backwashing the membrane with permeated water to remove the cake layer deposited during filtration. The second step involved removing the membrane module and rinsing it with tap water to remove any remaining cake layer. Next, the membrane was placed inside a container and submerged in water with the water level maintained at approximately 1 cm above the membrane to minimize light scattering. The membrane was then exposed to a solar simulator for 30 mins. The solar simulator used was a 300 W xenon lamp (Perfect Light, PLS-SXE 300) with a wavelength range of 320-780 nm and the light intensity was 100 mW/cm^2, corresponding to1 Sun illumination. Long-term filtration performance of the alumina and

ZnO/ALO membranes was examined using 3 L of the microalgae solution over three repetitive filtration cycles (1 L in each cycle).

3.2.2.4. *Microalgae*

The green microalgae strain *Scenedesmus sp.* (UTS-LD), isolated in Australia by the University of Technology Sydney (UTS), was used in this study. *Scenedesmus sp.* typically forms clusters of four cells known as a coenobium, with each coenobium resembling a comb shape approximately 12 μm long and 3 – 5 μm wide. The cells of *Scenedesmus sp.* exhibit a zeta potential of −23.2 ± 1.3 mV. The culture was maintained at the UTS Algae Production Facility using MLA medium and grown under laboratory conditions in pilot-scale photobioreactors ranging from 120–350 L, as described in a previous study [7]. For all measurements, the microalgae solution was kept at a concentration of 1.5 $\mathrm{OD}_{680\mathrm{nm}}$, corresponding to 0.7 mg/mL for *Scenedesmus sp.*

3.2.3. Results and discussions

3.2.3.1. *Structural properties of the neat alumina and ZnO/ALO membranes*

Preliminary work was conducted to optimize the deposition time for desirable ZnO coating thickness. To validate the results, ZnO was initially coated on a flat glass slide at specific deposition times and the coating thickness was measured using a profilometer [36], as shown in Fig. 3.19(a). The results confirmed successful deposition with average thicknesses of 200 $\pm$ 5 nm, 450 $\pm$ 5 nm, 750 $\pm$ 5 nm, and 1100 $\pm$ 5 nm. For clarity, these membranes are labelled as 200 nm–ZnO/ALO, 450 nm–ZnO/ALO, 750 nm–ZnO/ALO, and 1100 nm–ZnO/ALO, respectively.

SEM imaging reveals that the neat (uncoated) alumina membrane has a rough surface whereas the ZnO coated membranes show micron-sized ZnO domains with lateral dimensions of

1 – 3 mm (Fig. 3.14a). The uncoated alumina membrane exhibits non-uniform pores characteristic of porous ceramic membranes [24]. For the 200 nm-ZnO/ALO membrane, near-complete coverage by ZnO is observed with small visible gaps between ZnO domains. In contrast to the 1100 nm coating, which significantly obstructs permeate flow, the ZnO/ALO membranes with coating thicknesses of 450 nm and 750 nm exhibit a continuous coating layer on the alumina substrate without completely blocking the pores, thereby allowing water to pass through. The average pore size of the ALO membrane is approximately 100 nm. Based on SEM image analysis (Fig. 3.14a) using ImageJ software, the deposition of ZnO layers with thicknesses of 200 nm, 450 nm, 750 nm, and 1100 nm resulted in average pore size reductions of approximately 36%, 65%, 71%, and 92%, respectively. EDX elemental maps of Al and Zn as well as the EDX spectrum of the 450 nm-ZnO/ALO membranes (Fig. 3.14b, c) reveal complete coverage of the membrane surface by ZnO, demonstrating the effectiveness of the reactive sputtering technique and rotating stage during deposition. At the acceleration voltage of 15 kV, the electron beam penetrates the ZnO coating down to the alumina membrane, resulting in a uniform Al elemental EDX map (Fig. 3.14b). Coating the membrane with a 450 nm-thick ZnO layer reduces its surface roughness from 372 nm to 195 nm [Fig. 3.19(b)]. However, thicker ZnO coatings (750 nm and 1100 nm) lead to vertical grain growth (Fig. 3.14a), causing the surface roughness to exceed the measurement limit of the AFM. These results suggest a ZnO coating thickness of 450 nm is optimal as it effectively covers the membrane surface while minimizing surface roughness. The XRD patterns for the membranes (Fig. 3.14d), exhibit diffraction peaks (marked with black dots) attributed the α-Al_2O_3 phase of the alumina substrate [37], and the hexagonal wurtzite structure of ZnO layer, with diffraction peaks indexed to the (100), (002), (101), (102), (110), and (103) planes (JCPDS 36–1451) [26]. The optical absorption spectra of the ZnO coating layer (Fig. 3.14e) reveal a higher absorbance and a red shift in the absorption edge with increasing layer thickness. Tauc's plot analysis of

the ZnO layers (inset of Fig. 3.14e) shows a slight decrease in the band gap from 3.27 to 3.22 eV as the ZnO thickness increases from 200 to 1100 nm. This decrease in the optical bandgap with increasing film thickness is consistent with previous results of ZnO film growth by sputter deposition and is attributed to larger grain sizes and higher crystalline quality with increasing film thickness [38].

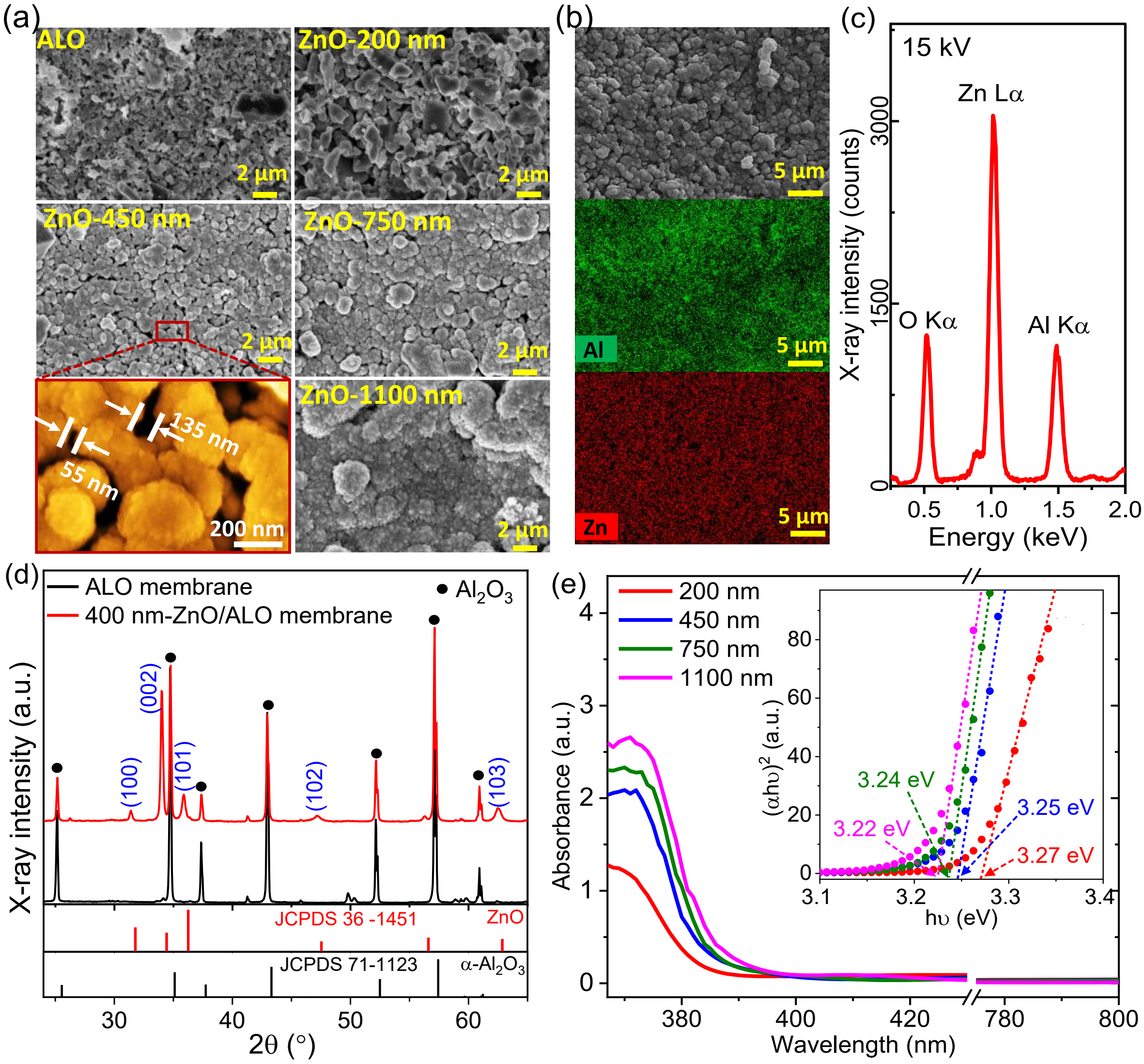

Figure 3.14. (a) SEM images of the neat alumina and ZnO-coated membranes with ZnO layer thicknesses of 200, 450, 750 and 1100 nm. (b, c) EDX elemental maps and spectrum of the 450 nm thick ZnO/ALO membrane acquired at 15 kV, showing a homogenous ZnO coating even over the membrane pores. (d) XRD patterns of neat alumina and 450 nm-ZnO/ALO

membranes. (e) UV-Vis absorption spectra and Tauc's plots for the ZnO coating layers, yielding the optical bandgap values indicated within the graph.

3.2.3.2. Membrane hydrophilicity

Surface hydrophilicity of the alumina and ZnO/ALO membranes is reported as water contact angle in Fig. 3.15). The contact angle of the alumina membrane is approximately 80°, consistent with previously reported values for alumina membranes [39]. Upon coating with ZnO, the contact angle decreases to 42 ± 4° for ZnO coating thicknesses between 200 and 750 nm, indicating an increase in the hydrophilicity of the coated membranes due to the hydrophilic nature of ZnO. This enhancement in hydrophilicity can be attributed to the presence of -OH groups on the ZnO surface, which interact with water molecules [26]. Furthermore, the contact angle of the 1100 nm–ZnO/ALO further decreases to 30°, likely due to the increased surface roughness associated with the thicker coating (Fig. 3.15a; ZnO-1100 nm). This observation is consistent with Wenzel's model, which states that increased surface roughness enhances the contact area between a droplet and the film surface, thereby increasing wettability [40]. Surface analysis of the oxygen chemical state in the alumina and ZnO/ALO coatings is analysed using XPS, with a photon energy of 650 eV (corresponding to a sampling depth of ~ 2 nm) (Fig. 3.20). Deconvolution of the O 1s spectra reveals two fitted peaks corresponding to two different chemical states of oxygen: O^{2-} ions (O-Zn) in the fully coordinated ZnO at a binding energy of 530.6 eV, and surface hydroxyl groups (Zn-OH) at 532.4 eV [41, 42]. The OH/O-Zn peak intensity ratio is found to be 0.24 for the neat alumina and 0.62 for the 450 nm-ZnO/ALO, indicating a higher proportion of surface -OH groups in the coated membranes.

ZnO coating improves filtration performance considerably (Fig. 3.15b). The uncoated alumina membrane exhibits a water permeate flux of around 58 LMH. Remarkably, all ZnO/ALO membranes show no significant flux reduction despite the decrease in pore size caused by the ZnO coatings, except for the membrane with a ZnO coating thickness of 1100 nm. This suggests that the increased hydrophilicity provided by the ZnO coating compensates for the reduced pore size, maintaining consistent water permeate flux. This observation, consistent with previous studies [25], indicates that coating ceramic membranes with hydrophilic metal oxide layers can sustain permeate flux even as pore size decreases. The permeate flux remains stable across all ZnO-coated membranes over the 90-minute filtration period.

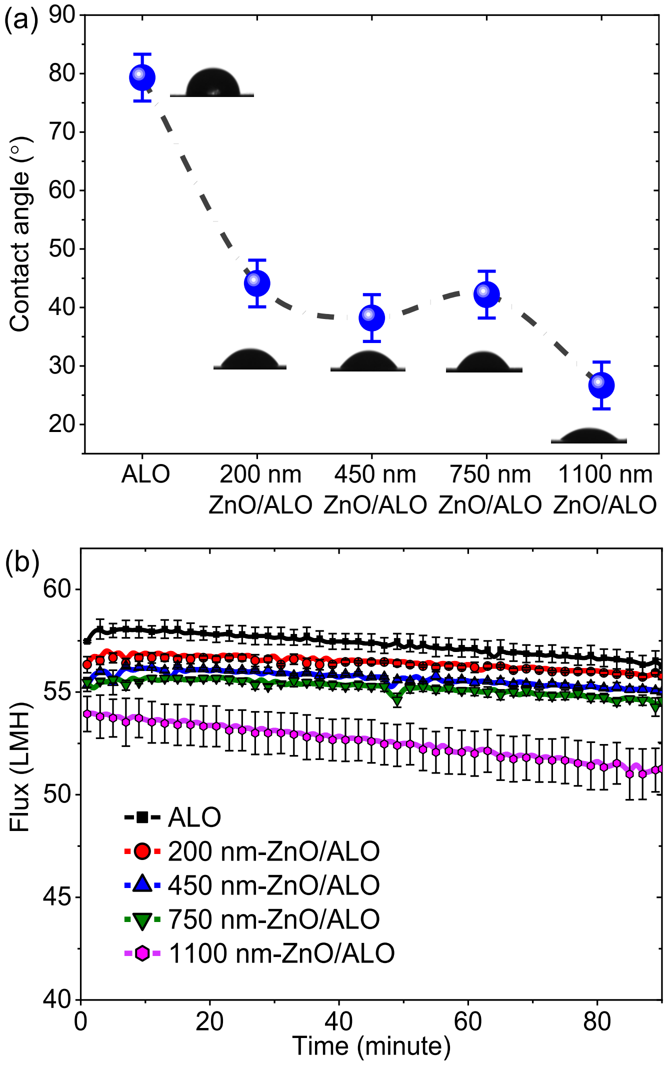

Figure 3.15. (a) Contact angle measurements for the ALO and ZnO/ALO membranes, accompanied by the photo of the water droplet on the membrane surface. (b) Pure water flux

through the neat alumina and ZnO/ALO membranes. Error bars represent the standard deviation calculated from two measurements.

3.2.3.3. Microalgae filtration performance

A volume of 1 L of pre-concentrated *Scenedesmus sp.* microalgae solution with an initial biomass concentration of 0.7 g/L was used to test the filtration performance of the alumina and ZnO/ALO membranes (Fig. 3.16a). The uncoated alumina membrane as well as the 450 nm–ZnO/ALO, and 750 nm–ZnO/ALO membranes also show a similar filtration profile. It took approximately 50 minutes to complete one filtration cycle (1 L) for each of the membranes. The decrease in permeate flux over time for the three membranes is due to the accumulation of microalgae on the membrane surface. The fouling rate is significantly less for the 200 nm–ZnO/ALO membrane, which has a shorter filtration cycle of 40 minutes. This improvement in filtration performance could be attributed to the combined effects of a relatively larger pore size and the hydrophilic ZnO-coated layer [24]. However, the 1100 nm–ZnO/ALO membrane exhibits an immediate drop in permeate flux, followed by a continued decline over a longer filtration cycle (Fig. 3.16a inset). The increase in TMP caused by the membrane's pore blockage is shown in Fig. 3.16b. Except for the 1100 nm-ZnO/ALO membrane, all the ZnO/ALO membranes exhibit lower TMP at the end of the filtration cycle than the uncoated alumina membrane. This is due to the more hydrophilic coating layer possibly due to the presence of hydroxylic groups on ZnO surface (Fig. 3.20). At the end of the filtration cycle, the TMP for the 200 nm–ZnO/ALO membrane is around 10 kPa, followed by 20 kPa, 23 kPa, and 53 kPa for the 450 nm, 750 nm and 1100 nm–ZnO/ALO membranes, respectively, approximately proportional to the increase in the thickness of the coating layer.

Scenedesmus sp. has a cylindrical-fusiform shape and exists as a coenobium consisting of four cells, each larger than 10 µm in size [15]. Due to their size, these cells cannot pass through or fully cover the membrane pores, causing their accumulation and adherence to the membrane surface. As expected, the measured microalgae rejection by the neat alumina and ZnO/ALO membranes was all above 99.9%. Aeration effectively reduces membrane fouling (Fig. 3.21). Under the aeration filtration condition, both the uncoated ALO and 450 nm–ZnO/ALO membranes exhibit a significant increase in permeate flux rate and reduction in TMP. This improvement in filtration performance is attributed to the synergistic effects of buoyancy and drag force from flowing bubbles, which reduce fouling by the dense cell cake layer [15].

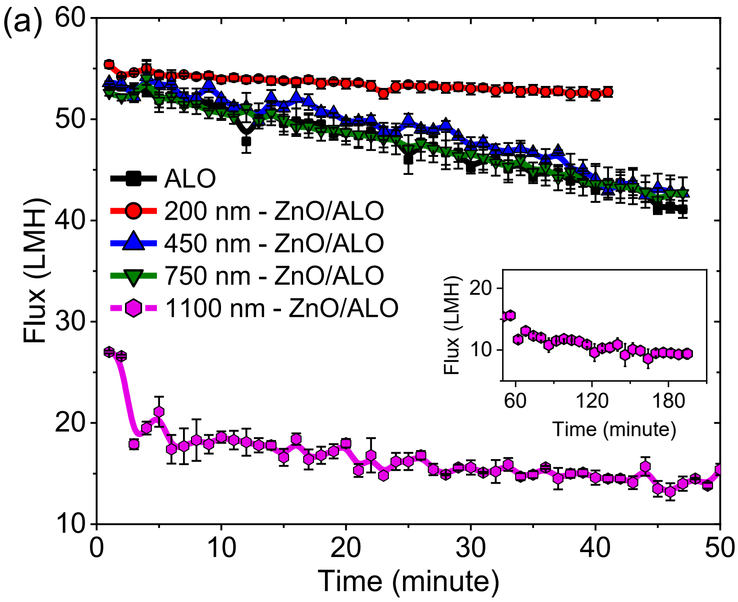

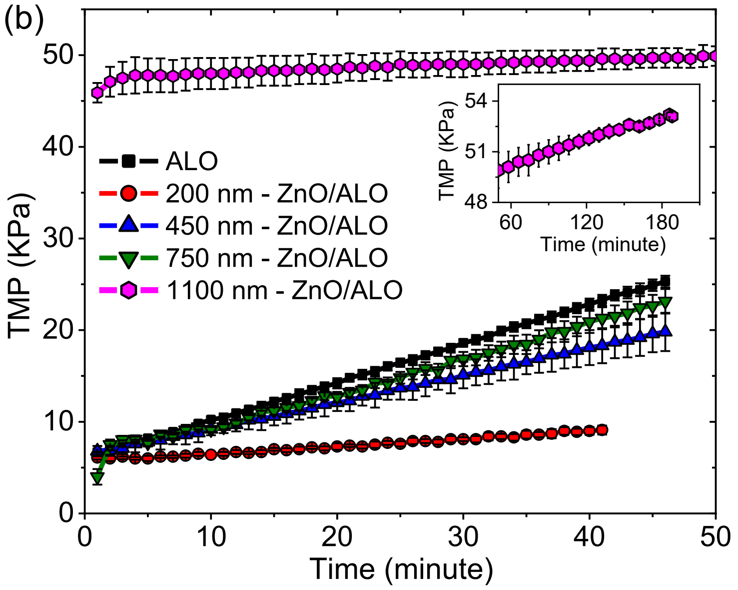

Figure 3.16. Variations of (a) flux, (b) TMP of the neat ALO and ZnO-coated ALO membranes during the filtration of 1 L of microalgae solution under non-aerated filtration conditions. The insets display the performance of the 1100 nm–ZnO/ALO membrane over extended filtration cycles. The error bar represents the standard deviation from two measurements.

3.2.3.4. Multi-filtration cycle performance

The long-term filtration performance of the alumina and ZnO/ALO membranes was evaluated over three repetitive filtration cycles. After each cycle, the membranes were backwashed at a flow rate of 30 mL/min for 3 minutes. At the beginning of each filtration process, a cake layer forms and rapidly covers the entire membrane surface, resulting in an immediate and noticeable decline in permeate flux and an increase in transmembrane pressure (TMP), as observed in the case of the uncoated ALO membrane (Fig. 3.17a). Similar findings have been reported in the literature, indicating that algae cake layer formation can occur within the first 5 minutes of the filtration cycle [43]. At the end of the second cycle, the permeate flux decreased by approximately 25% compared to the end of the first cycle, and this reduction further increased to 34% after the third cycle. The TMP increased by 32% after the first cycle and by an additional 16% after the second cycle. The decline in filtration performance is caused by the accumulation of *Scenedesmus sp.* on the membrane despite backwashing after each cycle. Conversely, the electrostatic repulsion between the negatively charged ZnO/ALO membrane surfaces due to the surface —OH groups and negatively charged *Scenedesmus sp.* cells (zeta potential of −23.2 ± 1.3 mV) reduces the adhesion of algae cells to the membrane wall, making the backwashing process more efficacious [44]. For instance, the 200 nm–ZnO/ALO membrane (Fig. 3.17b) exhibits only a 5% decrease in flux and less than a 24% increase in TMP after each cycle. Similar behaviour was observed for the 450 nm–ZnO/ALO and 750 nm–ZnO/ALO membranes (Fig. 3.17c and d). However, the smaller pore size in these two membranes results in a noticeable drop in permeate flux and an increase in TMP, although their filtration performance is still better than the uncoated alumina membrane. In the case of the 1100 nm–ZnO/ALO membrane, the excessive coating reduced the average pores size by approximately 92%, leading to a significant increase in the TMP during the backwashing step. This elevated pressure resulted in the formation of multiple leakage points at the membrane terminals, limiting the membrane's reusability in subsequent experiments.

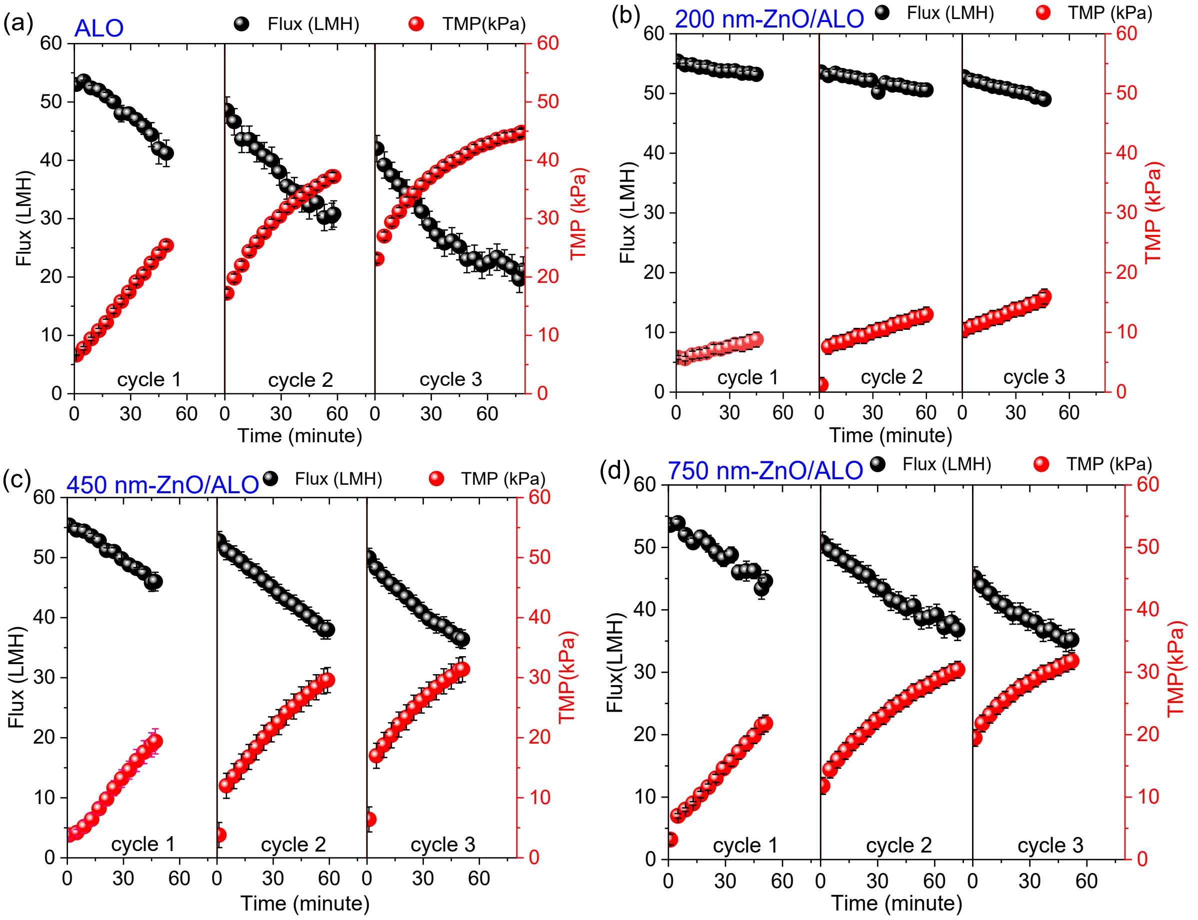

Figure 3.17. Comparison of permeate flux and TMP of (a) ALO, (b) 200 nm–ZnO/ALO, (c) 450 nm–ZnO/ALO, and (d) 750 nm–ZnO/ALO membranes during the dewatering of the microalgae solution across three repetitive filtration cycles. Each cycle involves recovering 1 L of water, followed by backwashing for 3 minutes. The error bars in the second and third cycles has been estimated from the first cycle.

3.2.3.5. Self-cleansing performance of the ZnO/ALO membranes

The self-cleaning property of the alumina and ZnO/ALO membranes is demonstrated in Fig. 3.18. The permeate water flux for the fouled membranes was recorded after backwashing and after irradiation with a solar simulator, and then compared with the initial unfouled membrane flux (Figure 3.18a). The neat alumina membrane recovers around 68% of its initial permeate flux after backwashing and around 81% after 30 minutes of solar irradiation. The slight improvement in the uncoated alumina is due to its ability to absorb a portion of the UV light from the solar irradiation [45, 46]. No further flux increase is observed with longer irradiation. In contrast, the ZnO/ALO membranes show a noticeable improvement in flux recovery after solar light irradiation, confirming the self-cleaning properties of the ZnO-coated layers. The 450 nm–ZnO/ALO membrane shows a flux recovery rate of 82% after the backwashing step and 102% after light irradiation. Slightly lower filtration performance was observed in the case of the 750 nm–ZnO/ALO membrane, with flux recovery rates of 79% and 98% after the backwashing and light irradiation steps, respectively. The slight reduction in recovered flux can be attributed to the blockage of some pores, likely caused by the higher TMP resulting from the decreased pore size in the 750 nm–ZnO/ALO membrane, as shown in Fig. 3.17d. Although the 200 nm–ZnO/ALO membrane shows the highest recovery rate through the backwashing process (83%), only around 90% flux recovery rate is achieved after light irradiation, indicating a lower photocatalytic self-cleaning property compared to the ZnO/ALO membranes with thicker ZnO coatings. This is likely due to the lower solar absorbance of the 200 nm–ZnO/ALO (Fig. 3.14e), which leads to a reduced generation of photogenerated radicals, limiting the oxidation of the deposited organic compounds [47, 48]. Among all tested membranes, the 450 nm–ZnO/ALO membrane demonstrated significantly higher recovery rate compared to both uncoated and 200 nm–ZnO/ALO membranes. Furthermore, when considering multiple performance indicators, including flux reduction, TMP and flux recovery rate, and the standard deviation (with error bars < 5%), 450 nm– ZnO/ALO membrane exhibited superior overall filtration performance compared to the 750 nm– ZnO/ALO membrane. Notably, prolonging the backwashing step does not significantly enhance the removal of biofouling. The self-cleaning mechanism of ZnO-coated membranes under solar light irradiation is illustrated in Fig. 3.18b. The simulated solar light used in this test has a wavelength range of 320 – 780 nm (corresponding to photon energies of 3.9 – 1.6 eV), which is partly absorbed by the ZnO coating layer (3.2 eV). Upon irradiation, the ZnO coating generates free electrons and holes, triggering photocatalytic activity. The photogenerated holes are effective at oxidizing organic compounds through the generation of ROS, including superoxide ($O_2^{-\bullet}$), peroxide (O_2^{2-}), and hydroxyl radicals ($OH^{\bullet}$). These reactive species effectively degrade organic materials such as microalgae residues, ensuring effective membrane cleaning [47]. Additionally, these radicals can penetrate the membrane pores, providing comprehensive cleaning.

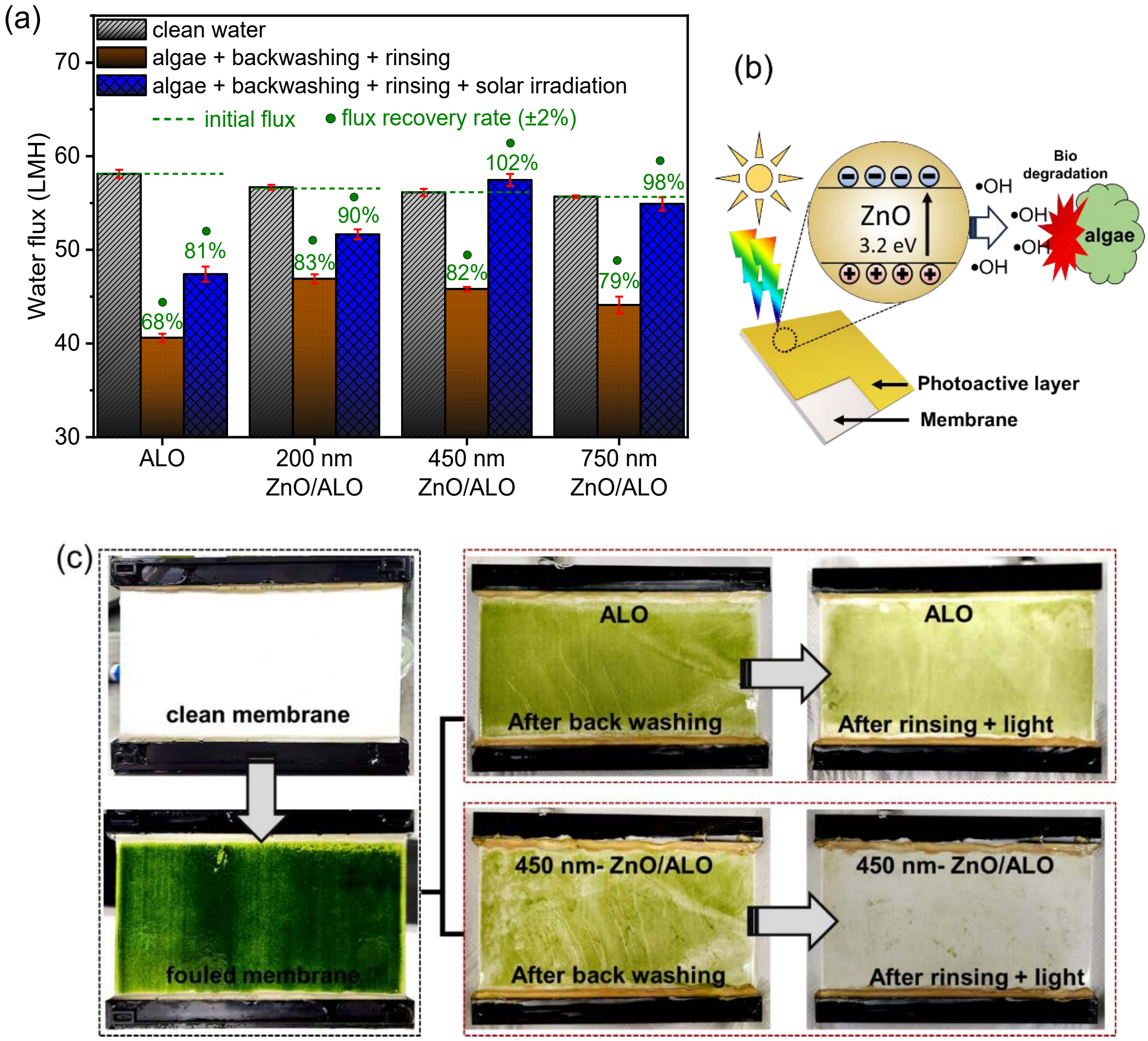

Figure 3.18. (a) Permeate water flux of the neat alumina and 450 nm–ZnO/ALO membranes under three conditions: (i) before fouling, (ii) after fouling and cleaning with backwashing (BW) and rinsing, and (iii) after fouling and cleaning with BW, rinsing and solar light irradiation. Error bars represent the standard deviation from two replicate experiments. (b) Schematic diagram illustrating the self-cleansing capability of photocatalytic ZnO/ALO

membranes. (c) Optical images of the fouled alumina and 450 nm–ZnO/ALO membranes before and after backwashing, followed by solar light cleansing.

Table 3.1. Comparison of flux recovery methods and performance for different microalgae harvesting membrane systems

Membrane	Microalgae species	Cleaning method	Flux recovery rate (%)	Ref.
ZnO/ALO	*Scenedesmus* sp.	Backwashing + solar irradiation	100%	This work
PVDF/PEI	*Chlorella* sp.	Stirring in water	100%	[49]
PVDF/TA-APTES@FeOOH	*Chlorella vulgaris*	H_2O_2 + solar irradiation	98.2%	[50]
PC@PDA/PEI/PSS/PDADMAC	*Chlorella vulgaris*	Water rinsing	~ 94%	[51]
PVDF	*Chlorella pyrenoidosa*	Water rinsing	90.7%	[52]
Stainless steel	*Chlorella* sp.	NaOH rinsing	68%	[53]
Stainless steel	*Scenedesmus* sp.	Water rinsing + UV irradiation	60%	[26]
Stainless steel	*Microcystis aeruginosa*	Backwashing	39.9%	[54]

Optical images of the neat alumina and 450 nm–ZnO/ALO membranes after fouling, backwashing and cleaning steps clearly demonstrate the effectiveness of photocatalytic self-cleansing (Figure 3.18c). After each filtration cycle, a thick and compact cake layer of *Scenedesmus sp.* is deposited on the membrane surface. Following backwashing, the cake layer deposited on the ZnO/ALO membrane is less dense compared to the uncoated alumina membrane. Subsequent water rinsing and solar irradiation further remove the majority of the deposited biofilm on the ZnO/ALO membrane due to the high AOP activity of the ZnO coating, while a significant amount of the biofilm remains on the uncoated alumina membrane. These images, captured after 15 filtering cycles and the backwashing processes, confirm the excellent durability and self-cleaning properties of the ZnO coating on the alumina membrane, ensuring more efficient and sustained performance over multiple filtration cycles. Table 3.1 compares the recovery methods and performance of various membrane filtration systems used for microalgae harvesting. The ZnO/ALO membrane demonstrate superior performance, achieving the complete recovery after backwashing and solar irradiation, outperforming most other cleaning methods [26, 53, 54]. Additionally, the ZnO/ALO membrane offers a straightforward fabrication process and greater durability compared to polymer-based membrane systems [49-52], making it highly competitive among microalgae harvesting systems. This highlights the economic promise of using ZnO/ALO membranes for microalgae harvesting. One drawback with the ZnO/ALO membrane is the potential release of by-products, such as Zn^{2+} ions. While these ions can provide health benefits in controlled amounts, excessive release may lead to toxicity risks [55]. Therefore, it is necessary to quantify the Zn^{2+} ion release and the generation of ROS post-treatment, and to assess their potential impacts on human health. The enhanced self-cleaning properties minimize the need for frequent or prolonged physical cleaning methods, such as vibration, and reduce chemical use. This not only preserves membrane durability but also extends operational lifespan and lowers maintenance costs. This study demonstrates that incorporating a ZnO coating on a ceramic alumina microfiltration membrane is a robust and cost-effective solution for maintaining high membrane performance in microalgae harvesting.

3.2.4. Conclusion

ZnO-coated ceramic membranes with self-cleansing capabilities were successfully developed for preconcentrating *Scenedesmus sp.* microalgae prior to harvesting. The ZnO coating enhanced the membrane's hydrophilicity, maintaining high permeate flux despite a reduction in pore size. Results from multiple filtration cycles showed a significant reduction in flux decline for ZnO-coated membranes (200–450 nm thickness) compared to uncoated membranes. However, excessive coating thickness led to pore blockage and reduced efficiency. The optimal 450 nm ZnO coating demonstrated 82% flux recovery after backwashing and rinsing, and 100% flux recovery after 30 minutes of solar irradiation, minimizing the need for intensive physical or chemical cleaning. Overall, this study presents an antifouling and photocatalytic ZnO-coated membrane filtration system. The approach offers a durable, scalable and cost-effective solution for efficient and sustainable microalgae harvesting, addressing the critical challenges associated with the economic competitiveness of microalgal products.

CRediT authorship contribution statement

Amar Salih: Conceptualization, Investigation, Experimental setup, Data curation, Sample characterization, Formal analysis, Writing − original draft. **Curtis P. Irvine:** Sample preparation, Experimental setup. **Fatima Matar:** Sample preparation and characterization. **Lisa Aditya:** Sample preparation, Experimental setup. **Long D. Nghiem:** Writing – review & editing, Methodology, Supervision, Formal analysis. **Cuong Ton-That:** Writing – review & editing, Supervision, Formal analysis.

Acknowledgements

This research was partly undertaken on the Soft X-ray Spectroscopy beamline at the Australian Synchrotron, part of ANSTO. The work was supported under Australian Research Council (ARC) Discovery Project funding scheme (project DP210101146). The authors would like to thank Anton Tadich, James Bishop and Herbert Yuan for technical support.

Long D. Nghiem is an Editor of the journal but is not involved in the editorial or review process.

Supplementary data

Supplementary data to this paper is available in the appendix: B

3.2.5. References

[1] T. Ramachandra, D. Hebbale, Bioethanol from macroalgae: Prospects and challenges, Renewable and Sustainable Energy Reviews 117 (2020) 109479.

[2] N. Kumar, C. Banerjee, J.-S. Chang, P. Shukla, Valorization of wastewater through microalgae as a prospect for generation of biofuel and high-value products, Journal of Cleaner Production 362 (2022) 132114.

[3] C. Ju, F. Wang, Y. Huang, Y. Fang, Selective extraction of neutral lipid from wet algae paste and subsequently hydroconversion into renewable jet fuel, Renewable Energy 118 (2018) 521-526.

[4] G. Deviram, T. Mathimani, S. Anto, T.S. Ahamed, D.A. Ananth, A. Pugazhendhi, Applications of microalgal and cyanobacterial biomass on a way to safe, cleaner and a sustainable environment, Journal of Cleaner Production 253 (2020) 119770.

[5] L.N. Nguyen, M.T. Vu, H.P. Vu, M.A.H. Johir, L. Labeeuw, P.J. Ralph, T. Mahlia, A. Pandey, R. Sirohi, L.D. Nghiem, Microalgae-based carbon capture and utilization: A critical review on current system developments and biomass utilization, Crit. Rev. Environ. Sci. Technol. 53(2) (2023) 216-238.

[6] A. Udayan, R. Sirohi, N. Sreekumar, B.-I. Sang, S.J. Sim, Mass cultivation and harvesting of microalgal biomass: Current trends and future perspectives, Bioresour. Technol. 344 (2022) 126406.

[7] L. Aditya, H.P. Vu, M.A.H. Johir, S. Mao, A. Ansari, Q. Fu, L.D. Nghiem, Synthesizing cationic polymers and tuning their properties for microalgae harvesting, Sci. Total Environ. 917 (2024) 170423.

[8] I. Demir-Yilmaz, M.S. Ftouhi, S. Balayssac, P. Guiraud, C. Coudret, C. Formosa-Dague, Bubble functionalization in flotation process improve microalgae harvesting, Chem. Eng. J. 452 (2023) 139349.

[9] A. Golzary, S. Imanian, M.A. Abdoli, A. Khodadadi, A. Karbassi, A cost-effective strategy for marine microalgae separation by electro-coagulation–flotation process aimed at bio-crude oil production: Optimization and evaluation study, Sep. Purif. Technol. 147 (2015) 156-165.

[10] M. Ghazvini, M. Kavosi, R. Sharma, M. Kim, A review on mechanical-based microalgae harvesting methods for biofuel production, Biomass Bioenergy 158 (2022) 106348.

[11] A. Agarwalla, K. Mohanty, A critical review on the application of membrane technology in microalgal harvesting and extraction of value-added products, Separation and Purification Technology (2024) 127180.

[12] J. Zhu, M. Wakisaka, T. Omura, Z. Yang, Y. Yin, W. Fang, Advances in industrial harvesting techniques for edible microalgae: Recent insights into sustainable, efficient methods and future directions, Journal of Cleaner Production (2024) 140626.

[13] A.K. Lau, M. Bilad, N. Nordin, K. Faungnawakij, T. Narkkun, D.K. Wang, T. Mahlia, J. Jaafar, Effect of membrane properties on tilted panel performance of microalgae biomass filtration for biofuel feedstock, Renewable and Sustainable Energy Reviews 120 (2020) 109666.

[14] S. Laksono, I.M. ElSherbiny, S.A. Huber, S. Panglisch, Fouling scenarios in hollow fiber membranes during mini-plant filtration tests and correlation to microalgae-loaded feed characteristics, Chem. Eng. J. 420 (2021) 127723.

[15] L. Aditya, H.P. Vu, L.N. Nguyen, T.I. Mahlia, N.B. Hoang, L.D. Nghiem, Microalgae enrichment for biomass harvesting and water reuse by ceramic microfiltration membranes, J. Membr. Sci. 669 (2023) 121287.

[16] Z. Zhao, B. Liu, A. Ilyas, M. Vanierschot, K. Muylaert, I.F. Vankelecom, Harvesting microalgae using vibrating, negatively charged, patterned polysulfone membranes, Journal of Membrane Science 618 (2021) 118617.

[17] H. Chen, A. Zhou, Y. Zhang, X. Wang, G. Pan, S. Xu, Q. Liu, H. Shan, Q. Fu, J. Ge, Carbonaceous nanofibrous membranes with enhanced superhydrophilicity and underwater superoleophobicity for effective purification of emulsified oily wastewater, Chem. Eng. J. 468 (2023) 143602.

[18] Z.R. Usha, D.M. Babiker, Y. Zhao, X. Chen, L. Li, Advanced super-wetting biaxial polypropylene membrane with hierarchical rough surface for multipollutant removal from oily wastewater, Journal of Environmental Chemical Engineering 11(5) (2023) 110775.

[19] J. Lu, T. Bai, D. Wang, H. Yu, Q. Wang, Z. Niu, Y. Hu, X. Liu, G. Han, W. Cheng, Electrospun polyacrylonitrile membrane in situ modified with cellulose nanocrystal anchoring TiO2 for oily wastewater recovery, Advanced Fiber Materials 5(6) (2023) 2055-2068.

[20] N. Daneshvar, D. Salari, A. Khataee, Photocatalytic degradation of azo dye acid red 14 in water on ZnO as an alternative catalyst to TiO_2, J. Photochem. Photobiol. A: Chem. 162(2-3) (2004) 317-322.

[21] K.M. Lee, C.W. Lai, K.S. Ngai, J.C. Juan, Recent developments of zinc oxide based photocatalyst in water treatment technology: a review, Water research 88 (2016) 428-448.

[22] Z. Huang, L. Shen, H. Lin, B. Li, C. Chen, Y. Xu, R. Li, M. Zhang, D. Zhao, Fabrication of fibrous MXene nanoribbons (MNRs) membrane with efficient performance for oil-water separation, Journal of Membrane Science 661 (2022) 120949.

[23] J. Yu, L. Zhang, L. Shen, R. Li, D. Zhao, H. Lin, Y. Xu, Y. Jiao, In situ grown cyclodextrin metal-organic framework nanoparticles templated stripe nano-wrinkled polyamide nanofiltration membranes for efficient desalination and antibiotic removal, Journal of Membrane Science 694 (2024) 122413.

[24] K.-H. Park, P.-F. Sun, E.H. Kang, G.D. Han, B.J. Kim, Y. Jang, S.-H. Lee, J.H. Shim, H.-D. Park, Photocatalytic anti-biofouling performance of nanoporous ceramic membranes treated by atomic layer deposited ZnO, Separation and Purification Technology 272 (2021) 118935.

[25] A. Lee, J.A. Libera, R.Z. Waldman, A. Ahmed, J.R. Avila, J.W. Elam, S.B. Darling, Conformal nitrogen-doped TiO_2 photocatalytic coatings for sunlight-activated membranes, Advanced Sustainable Systems 1(1-2) (2017).

[26] A.K. Salih, L. Aditya, F. Matar, L.D. Nghiem, C. Ton-That, Improved flux and anti-fouling performance of a photocatalytic ZnO membrane on porous stainless steel substrate for microalgae harvesting, J. Membr. Sci. 694 (2024) 122405.

[27] Z.-Q. Huang, K. Chen, S.-N. Li, X.-T. Yin, Z. Zhang, H.-T. Xu, Effect of ferrosoferric oxide content on the performances of polysulfone–ferrosoferric oxide ultrafiltration membranes, Journal of Membrane Science 315(1-2) (2008) 164-171.

[28] A. Di Mauro, M. Zimbone, M.E. Fragalà, G. Impellizzeri, Synthesis of ZnO nanofibers by the electrospinning process, Materials Science in Semiconductor Processing 42 (2016) 98-101.

[29] M. Storms, A.J. Kadhem, S. Xiang, M. Bernards, G.J. Gentile, M.M. Fidalgo de Cortalezzi, Enhancement of the fouling resistance of Zwitterion coated ceramic membranes, Membranes 10(9) (2020) 210.

[30] R. Goei, T.-T. Lim, Ag-decorated TiO_2 photocatalytic membrane with hierarchical architecture: Photocatalytic and anti-bacterial activities, Water research 59 (2014) 207-218.

[31] L. Van, M. Hong, J. Ding, Structural and magnetic property of Co-doped–ZnO thin films prepared by pulsed laser deposition, Journal of Alloys and Compounds 449(1-2) (2008) 207-209.

[32] L.L. Coelho, M. Grao, T. Pomone, M. Ratova, P. Kelly, M. Wilhelm, R.d.F.P.M. Moreira, Photocatalytic microfiltration membranes produced by magnetron sputtering with self-cleaning capabilities, Thin Solid Films 747 (2022) 139143.

[33] R. Vevers, A. Kulkarni, A. Seifert, K. Pöschel, K. Schlenstedt, J. Meier-Haack, L. Mezule, Photocatalytic Zinc Oxide Nanoparticles in Antibacterial Ultrafiltration Membranes for Biofouling Control, Molecules 29(6) (2024) 1274.

[34] S. Abou Zeid, Y. Leprince-Wang, Advancements in ZnO-based photocatalysts for water treatment: a comprehensive review, Crystals 14(7) (2024) 611.

[35] S. Heinonen, J.-P. Nikkanen, E. Huttunen-Saarivirta, E. Levänen, Investigation of long-term chemical stability of structured ZnO films in aqueous solutions of varying conditions, Thin Solid Films 638 (2017) 410-419.

[36] M. Karthik, J.M. Gohil, A.K. Suresh, Probing the thickness and roughness of the functional layer in thin film composite membranes, International Journal of Hydrogen Energy 42(42) (2017) 26464-26474.

[37] H. Qin, W. Guo, X. Huang, P. Gao, H. Xiao, Nanoscale phase transition seeds-assisted low temperature preparation of α-Al2O3 ultrafiltration membrane, Microporous Mesoporous Mater. 293 (2020) 109815.

[38] A. Samavati, H. Nur, A.F. Ismail, Z. Othaman, Radio frequency magnetron sputtered ZnO/SiO2/glass thin film: role of ZnO thickness on structural and optical properties, J. Alloys Compd. 671 (2016) 170-176.

[39] S. Koonaphapdeelert, K. Li, Preparation and characterization of hydrophobic ceramic hollow fibre membrane, J. Membr. Sci. 291(1-2) (2007) 70-76.

[40] C.E. Caballero-Güereca, M.A. Cruz, E. Luévano-Hipólito, L.M. Torres-Martínez, Transparent ZnO thin films deposited by dip-coating technique: Analyses of their hydrophobic properties, Surfaces and Interfaces 37 (2023) 102705.

[41] K.H. Yoon, H. Kim, Y.-E.K. Lee, N.K. Shrestha, M.M. Sung, UV-enhanced atomic layer deposition of Al 2 O 3 thin films at low temperature for gas-diffusion barriers, RSC advances 7(10) (2017) 5601-5609.

[42] M.S. Abdel-Wahab, A. Jilani, I. Yahia, A.A. Al-Ghamdi, Enhanced the photocatalytic activity of Ni-doped ZnO thin films: Morphological, optical and XPS analysis, Superlattices Microstruct. 94 (2016) 108-118.

[43] Z. Yu, H. Chu, W. Zhang, K. Gao, L. Yang, Y. Zhang, X. Zhou, Multi-dimensional in-depth dissection the algae-related membrane fouling in heterotrophic microalgae harvesting: Deposition dynamics, algae cake formation, and interaction force analysis, Journal of Membrane Science 635 (2021) 119501.

[44] L. Miao, C. Wang, J. Hou, P. Wang, J. Qian, S. Dai, Kinetics and Equilibrium Biosorption of Nano-ZnO Particles on Periphytic Biofilm under Different Environmental Conditions, Journal of Environmental Informatics 23(2) (2014).

[45] R. Ahmad, J.K. Kim, J.H. Kim, J. Kim, Effect of polymer template on structure and membrane fouling of TiO_2/Al_2O_3 composite membranes for wastewater treatment, Journal of industrial and engineering chemistry 57 (2018) 55-63.

[46] P. Prashanth, R. Raveendra, R.H. Krishna, S. Ananda, N. Bhagya, B. Nagabhushana, K. Lingaraju, H.R. Naika, Synthesis, characterizations, antibacterial and photoluminescence studies of solution combustion-derived α-Al_2O_3 nanoparticles, Journal of Asian Ceramic Societies 3(3) (2015) 345-351.

[47] M. Rezayian, V. Niknam, H. Ebrahimzadeh, Oxidative damage and antioxidative system in algae, Toxicology reports 6 (2019) 1309-1313.

[48] A.K. Salih, M.R. Phillips, C. Ton-That, Enhanced solar-driven water splitting performance using oxygen vacancy rich ZnO photoanodes, Solar Energy Materials and Solar Cells 259 (2023) 112436.

[49] T. Hwang, M.R. Kotte, J.-I. Han, Y.-K. Oh, M.S. Diallo, Microalgae recovery by ultrafiltration using novel fouling-resistant PVDF membranes with in situ PEGylated polyethyleneimine particles, Water Research 73 (2015) 181-192.

[50] Y. Wang, Z. Jiao, W. Li, S. Zeng, J. Deng, M. Wang, L. Ren, Superhydrophilic membrane with photo-Fenton self-cleaning property for effective microalgae anti-fouling, Chinese Chemical Letters 34(8) (2023) 108020.

[51] R. Huang, Z. Liu, B. Yan, Y. Li, H. Li, D. Liu, P. Wang, F. Cui, W. Shi, Layer-by-layer assembly of high negatively charged polycarbonate membranes with robust antifouling property for microalgae harvesting, Journal of Membrane Science 595 (2020) 117488.

[52] F. Zhao, X. Han, Z. Shao, Z. Li, Z. Li, D. Chen, Effects of different pore sizes on membrane fouling and their performance in algae harvesting, Journal of membrane science 641 (2022) 119916.

[53] A. Ahmad, N.M. Yasin, C. Derek, J. Lim, Chemical cleaning of a cross-flow microfiltration membrane fouled by microalgal biomass, Journal of the Taiwan Institute of Chemical Engineers 45(1) (2014) 233-241.

[54] D. Xu, Y. Qin, Y. Fang, M. Chen, X. Li, J. Cai, Stainless steel membranes for harvesting cyanobacteria: Performance, fouling and cleaning, Bioresource Technology 319 (2021) 124143.

[55] S.R. Lee, Critical role of zinc as either an antioxidant or a prooxidant in cellular systems, Oxidative medicine and cellular longevity 2018(1) (2018) 9156285.

3.2.6. Appendix B: Additional characterization and membranes filtration data

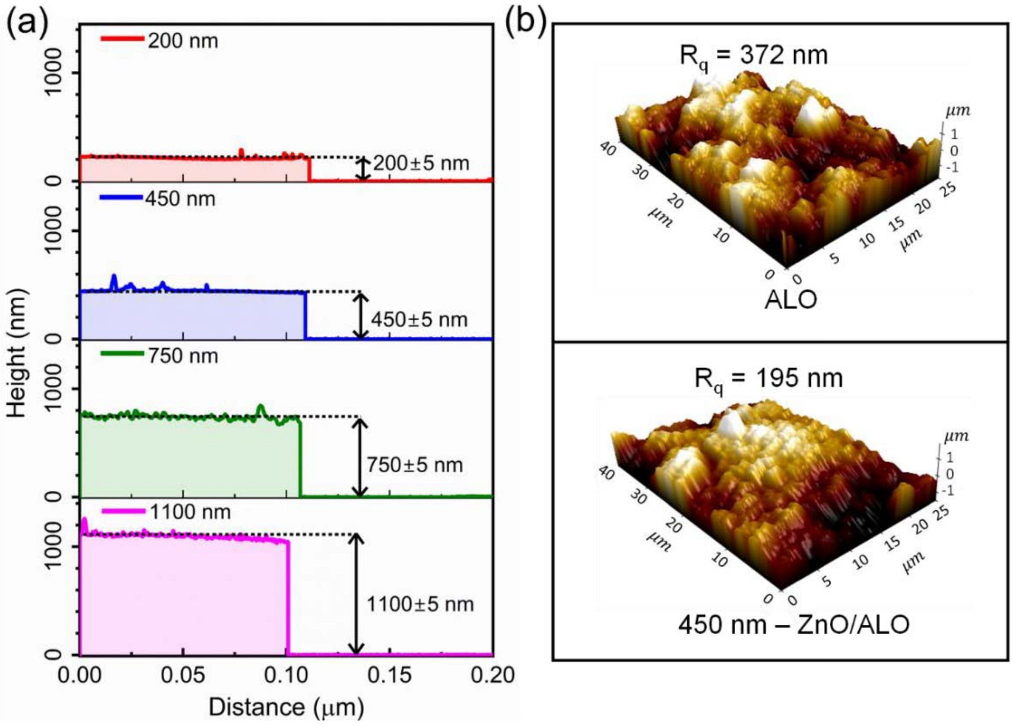

Figure 3.19. (a) Surface profiles showing the thickness of the ZnO coating layers. (b) AFM images of the ALO membrane before and after coating with a 450 nm ZnO layer. The RMS roughness measured over an area of 25 ´ 25 mm^2 is R_q = 372 nm the bare ALO membrane and 195 nm for the ZnO/ALO membrane.

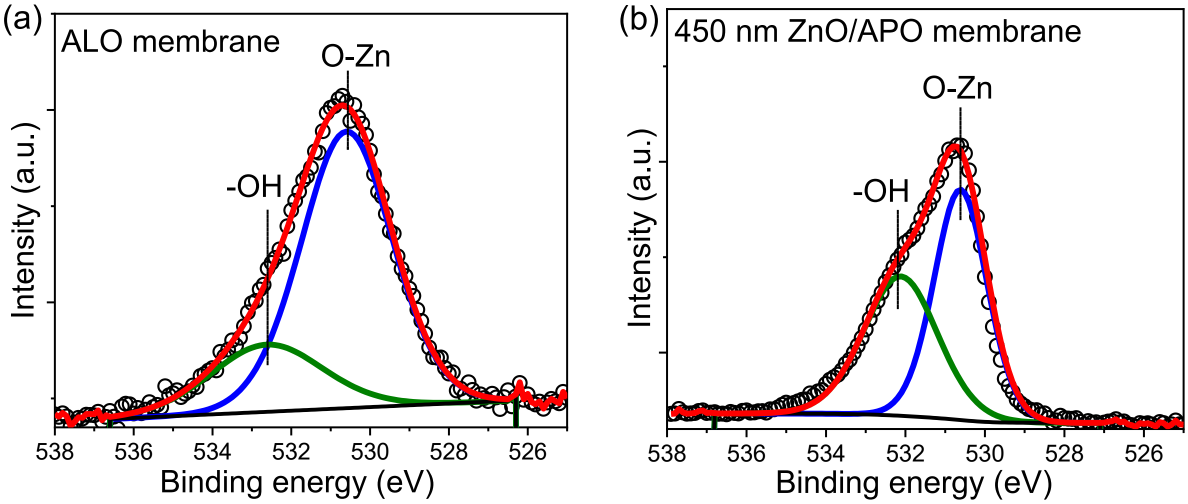

Figure 3.20. Surface-sensitive XPS O 1s spectra of the bare ALO and 450 nm-ZnO/ALO membranes, acquired at a photon energy of 650 eV. The spectra reveal a higher density of surface hydroxyl groups (-OH) on the coated membrane.

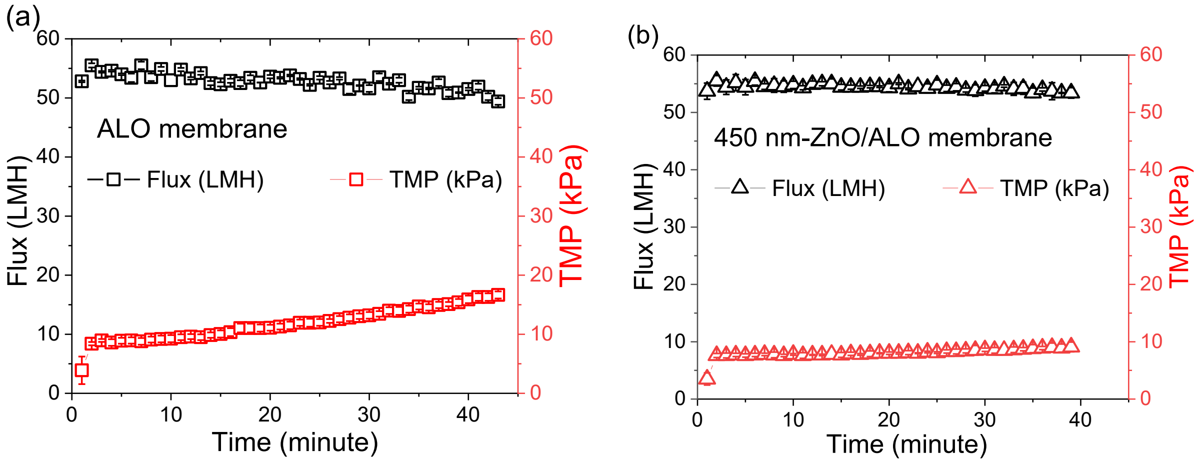

Figure 3.21. Variations of flux and TMP for (a) uncoated ALO and (b) 450 nm–ZnO/ALO membranes during the filtration of 1 L of microalgae solution in the aerated filtration condition. The error bars represent the standard deviation from two measurements.

Chapter 4. Enhanced solar-driven water splitting performance using oxygen vacancy rich ZnO photoanodes

This chapter presents a scalable and economical approach for fabricating high-performance ZnO photoanodes to enhance hydrogen evolution via PEC water splitting. The study presents a comprehensive investigation into the development of nanostructured ZnO films enriched with V_O for enhanced solar-driven water splitting. By engineering oxygen vacancies and ZnO film morphologies, this approach aims to enhance charge carrier separation, extend light absorption and improve PEC performance, offering a promising pathway toward efficient hydrogen production.

Abstract

This work reports a facile two-step method of producing highly efficient ZnO photoanodes for photoelectrochemical (PEC) water splitting under solar light conditions and describes the role of surface oxygen vacancies (V_O) in their enhanced PEC performance. The photoanode fabrication involves post-growth oxidation of a metallic Zn layer, which produces a nanostructured ZnO film consisting of ~50 nm diameter nanorods containing a high concentration of V_O defects. The PEC activity of the ZnO films is investigated by studying water oxidation in an aqueous electrolyte under simulated solar illumination. The relationship of PEC and charge transfer characteristics of the ZnO photoanodes with ionized surface V_O defects is established using cathodoluminescence, X-ray photoemission, voltammetry, electrochemical impedance spectroscopy and chronoamperometry. The combined results show that the photoanode fabricated in this work possesses a high surface density of ionized V_O states that facilitate the effective transportation of holes for water oxidation. It is found that the photoanode exhibits an exceptional photocurrent density of 1.14 mA/cm^2 at 1.23 V_{RHE}, being one of the best performances reported in the literature for ZnO-based photoelectrodes so far. Our results demonstrate a simple, low-cost method for fabricating highly efficient V_O rich ZnO-based PEC photoanodes that is suitable for large scale production.

Keywords: photoelectrochemical water splitting; oxides; photoanodes; surface defects; oxygen vacancies

4.1. Introduction

Utilizing renewable energy from hydrogen sources is currently attracting considerable attention to address energy and environmental issues. Photoelectrochemical (PEC) water splitting is widely considered to be a viable technique to generate sustainable, clean and storable hydrogen energy from water using solar radiation.[1-3] During water slitting, two separate half-reactions are involved in the PEC redox process: a water reduction reaction ($\mathrm{H_2}$ reduction, $\mathrm{2H_2O + 2e^- \rightarrow H_2 + 2OH^-}$) and a water oxidation reaction ($\mathrm{O_2}$ production, $\mathrm{2H_2O + 4h^+ \rightarrow O_2 + 4H^+}$).[3] When an n-type ZnO photoanode is immersed in a suitable water-based electrolyte, conduction band (CB) electrons flow from the ZnO electrode to the solution since the ZnO Fermi level is above the electrolyte redox potential. This outward flow of electrons to the electrolyte creates a depletion layer at the ZnO photoanode surface with a build-in potential and an associated electric field pointing towards redox interface that causes upward bending of the near-surface band edges.[4, 5] Under solar illumination, e-h pairs generated within the surface depletion layer by photoionization are formed and subsequently charge separated by the electric field. Consequently, photogenerated holes drift towards the semiconductor/electrolyte interface, where they oxidize water molecules creating O_2, while photogenerated electrons are transported to the cathode through an external bias voltage to reduce water molecules generating H_2.[6] Of these two-half reactions, the water oxidation process is considered to be a bottleneck in the PEC water splitting efficiency because it is a sluggish reaction requiring the rapid transfer of four holes to the electrolyte to create one molecule of oxygen. In comparison, the water reduction needs the transfer of a single electron to generate a molecule of hydrogen.

Several metal oxides such as Fe_2O_3, CdO, TiO_2, and ZnO have been evaluated as potential photoanodes for PEC water splitting because of their low fabrication cost and high stability in aqueous media compared with other types of traditional semiconductors.[1, 7-9] However, to date most of most metal oxide photoanodes have been proven to be unsuitable for PEC applications. For example, hematite (α-Fe_2O_3) exhibits poor charge separation in its surface depletion layer due to a low hole drift mobility and short hole diffusion length,[10] CdO is not suitable as Cd is highly toxic while TiO_2 absorbs solar radiation poorly due to its wide bandgap and poor hole transport.[11] In contrast, ZnO is an attractive PEC candidate due to its favorable band edge energy positions with respect to the redox potentials of water, low toxicity, ability to be grown in a variety of bespoke nanostructures, and significantly larger hole mobility compared with TiO_2 and Fe_2O_3.[12-14] Recently, it has been reported that the introduction of oxygen vacancy (V_O) defects can be used to increase the PEC efficiency of oxide-based photoanodes [15-18]. Different methods have been attempted to create V_O defects in ZnO, including hydrogenation, growth under oxygen-deficient conditions, post-growth annealing under a reducing atmosphere, as well as lowering the V_O formation energy by the incorporation of acceptor dopants.[19-22] Significantly, Duan *et al.*[17] used electrochemical reduction to increase the V_O density in ZnO and observed a threefold increase in the PEC photocurrent density. While the benefits of V_O incorporation into oxide photoanodes on the PEC performance are clear,[1] no phenomenological model currently exists to explain the role of this defect in the underlying electrical processes at metal oxide photoanodes. This work focuses on the incorporation of V_O defects in ZnO photoanodes by the oxidation of metallic Zn films and their role in mediating the PEC performance. It is found that V_O rich ZnO photoanodes fabricated using this approach exhibit an exceptional photocurrent density of 1.14 mA/cm^2 at 1.23 V_{RHE}, being among the best ZnO-based PEC performance values reported in the literature so far. These ZnO photoanodes exhibit an intense signature green luminescence (GL) band associated with V_O defects. Accordingly, we present a model that explains the relationship between the density of V_O defects in ZnO photoanodes and their PEC activity, shown in the schematic in Figure 4.1. Here, *e-h* pairs are separated by the electric field across the depletion layer efficiently transporting holes to the ZnO photoanode/electrolyte interface rich in reactive charged V_O^{2+} surface sites that enhance the PEC water redox reaction. The high concentration of near interface V_O^{2+} is produced by the transformation of bulk V_O^{O} due to the surface upward bending of the $V_O^{2+/0}$ charge transfer level (CTL) above the Fermi level of the *n*-type ZnO photoanode. The model is supported by cathodoluminescence (CL) and X-ray photoemission spectroscopy (XPS) studies, which both confirm that the ZnO photoanode with the highest PEC performance has the largest V_O concentration. We further present a facile, inexpensive method for producing high-performance ZnO-based photoanodes that exhibit a high absorption efficiency in the visible spectral range and low charge-transfer resistance.

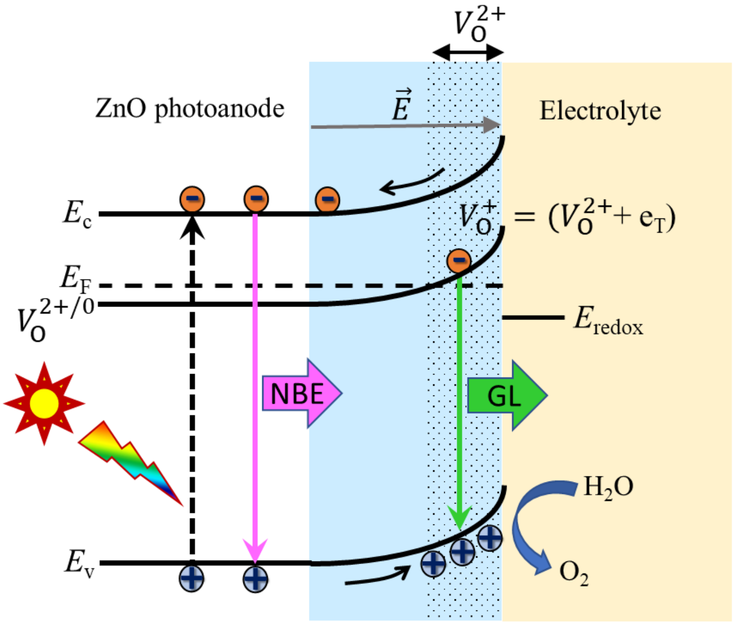

Figure 4.1. A schematic representation of the PEC and GL processes in a V_O rich ZnO photoanode. Since the surface pinned Fermi level (E_F) of the *n*-type ZnO photoanode is typically above the electrolyte redox potential (E_{redox}), CB electrons flow from ZnO to the electrolyte. This charge equalization produces a surface depletion layer (blue region) with an associated outward pointing electric field that causes upward bending of the band edges. The *e-h* pairs photoexcited within the depletion layer are charge separated by the electric field, which transports holes (electrons) to the photoanode (cathode)/electrolyte interface to drive the oxidation (reduction) reaction. Notably, the $V_O^{2+/0}$ CTL also bends upwards and when it rises above E_F a near surface layer of reactive V_O^{2+} defects (blue shaded region) is produced that promotes the PEC water redox process. The V_O^{2+} defects can also capture a free electron forming the V_O^{+} (V_O^{2+} + e_T) state with a deeply trapped electron (e_T) that can radiatively recombine with a photogenerated free hole, producing the observed GL (green arrow) and restoring the V_O^{2+} state.[23] Ultraviolet emission (purple arrow) arises from the near-band-edge (NBE) *e-h* recombination in the ZnO bulk.

4.2. Experimental

4.2.1. Fabrication of ZnO thin films for photoanodes

Two fabrication approaches were used to produce ZnO photoanodes. The first approach involved depositing a metallic Zn films of ~ 200 nm thickness on an FTO-coated glass substrate (Sigma-Aldrich, 8 Ω/sq resistivity) using a DC sputtering system (NSC-4000, Nanomaster). The sputtering target was metallic Zn (99.995 % purity, ACI alloys Inc.). The sputtering chamber had a base pressure of 8×10^{-6} torr and was maintained at a working pressure of 3×10^{-3} torr during film deposition at a DC sputtering power of 100 W, a constant Ar flow of 75 sccm for 10 mins. The deposited Zn films were oxidized in ambient air using a tube furnace at 450, 550, and 650 °C (denoted as Zn-450ºC, Zn-550ºC, and Zn-650ºC, respectively). The furnace was heated at a rate of 10 °C/min to the set temperature and the films were annealed for two hours. The second approach was to deposit a ZnO film via DC reactive sputtering deposition in a 1:1 Ar/O_2 gas mixture, and a thickness of ~ 200 nm. The film was then annealed for 2 hours at 550 ºC separately in argon or air atmosphere (denoted as ZnO-argon, and ZnO-air, respectively, and ZnO-AG for as-grown ZnO). The annealing temperature of 550 °C was selected to ensure high film crystallinity without deforming the FTO substrate, consistent with previous studies [21]. This temperature allows for a systematic comparison with the highest performance achieved using the previous fabrication approach. It is worth noting that the fabricated ZnO photoanodes will exhibit upward surface bending of the band edges due to chemisorbed oxygen species depleting electrons from the ZnO surface.

4.2.1.1. Structural and optical characterization

The fabricated ZnO films were characterized using a broad variety of complementary analytical techniques. First, the crystallinity of the ZnO films was examined using X-ray diffraction (XRD, Rigaku Miniflex-600) using Cu Kα radiation $\lambda = 1.5406$ Å. The ZnO film morphologies were investigated using Zeiss Supra 55VP scanning electron microscope (SEM). The optical properties of the films were studied using a double-beam UV-Vis spectrometer (Jasco V-570). CL measurements were performed on a FEI Quanta 200 SEM equipped with a parabolic mirror collector and an Ocean Optics QE65000 spectrometer; all CL spectra were corrected for the total system response. Chemical state analysis of the films was conducted using XPS (ESCALAB250Xi, Thermo Fisher); binding energies were calibrated using the C 1*s* peak at 286 eV. All samples were etched with Ar^+ ions for 30 seconds before XPS analysis.

4.2.1.2. Photoelectrochemical and photocatalytic measurements

The PEC performance of the ZnO photoanodes was investigated using chronoamperometry, linear sweep voltammetry, and electrochemical impedance spectroscopy in a quartz cell connected to a Voltalab PGZ 402 potentiostat via a three-electrode measuring setup as described previously.[24] ZnO thin-films, saturated calomel electrode (SCE), and platinum coil were used as working electrodes, reference electrode, and counter electrode, respectively. The measured potential (V_{SCE}) was converted to the reversible hydrogen electrode (V_{RHE}) potential using Nernst equation:[25]

$$\mathrm{V_{RHE}} = \mathrm{V_{SCE}} + 0.0591 \times \mathrm{pH} + \mathrm{V_{SCE}^{0}} \qquad \text{Eq. (4.1)}$$

where $\mathrm{V_{SCE}}$ is the applied potential versus the SCE, and $\mathrm{V_{SCE}^{0}}$ (= 0.244 V) is the standard redox potential of the SCE at 298 K. A 0.5 M Na_2SO_4 solution was utilized as an electrolyte. The photocatalytic activity of the ZnO photoanode was assessed under simulated solar light irradiation using a Xenon lamp (Max-303, 300 W) with a light intensity of 100 mW/cm^2 in the wavelength range of 300 – 600 nm The charge transfer resistance (R_{ct}) of the deposited films was determined using electrochemical impedance spectroscopy (EIS) in the dark and under illumination. The EIS measurements were made over the frequency range from 10 mHz to 100 kHz.

4.3. Results and discussion

4.3.1. Fabrication of ZnO photoanodes rich with oxygen vacancies

Typical SEM images of the ZnO films studied are displayed in Figure 4.2. The as-grown ZnO-AG film has a granular texture comprised of irregular shaped ~ 100 nm plate-like particles, suggesting that the FTO substrate is responsible for the rough morphology and voids in the films. The ZnO-air and ZnO-argon films, shown in Figure 4.2(b, c), consist of closely packed, uniform crystal grains with a ~ 50 nm diameter. The morphology of the oxidized Zn films is distinctly different, exhibiting randomly oriented nanorod-like structures with an average diameter of approximately 20 nm (inset of Fig. 4.2e). These nanorods are formed during the annealing process as a result of the interaction between the metallic Zn layer and atmospheric oxygen. Initially, the top layer of the Zn film oxidizes to form ZnO. As annealing continues for 2 hours, Zn ions diffuse through the grain boundaries of the ZnO layer to the air/ZnO interface, and subsequently oxidize, leading to the formation of nanowire-like structures [26]. The nanorods are found to enlarge with increasing annealing temperature. These results are significant as the active surface area of a ZnO photoanode is directly proportional to its PEC activity.

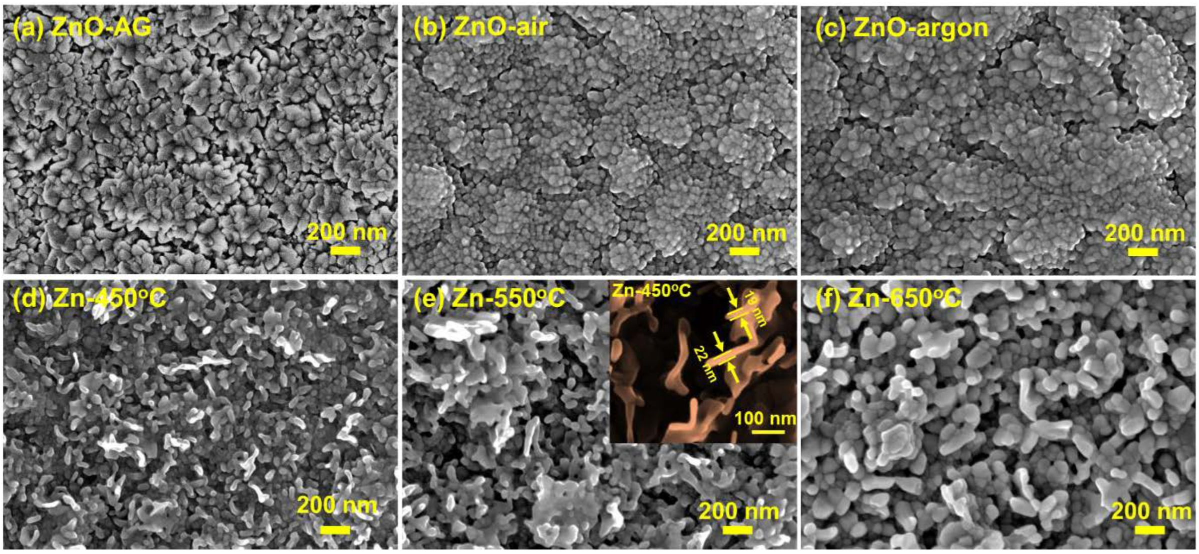

Figure 4.2. Typical SEM images of the ZnO films (a, b, and c) and the oxidized Zn films (d, e and f). The ZnO films grow in the form of closely packed crystal grains, while the oxidized Zn films are comprised of randomly oriented nanorods. The nanorods in the oxidized Zn films become larger in both diameter and length as the post-oxidation temperature is raised from 450 to 650°C.

The XRD patterns for both the ZnO and oxidized Zn film sets are shown in Figure 4.3. All the diffraction patterns contain peaks (indicated by a red circle) corresponding to the FTO coating layer of the substrate. The fabricated ZnO films by the DC reactive sputtering method (ZnO-AG, ZnO-argon, and ZnO-air) exhibit a strong preferential growth along the *c*-axis parallel to the surface normal as expected. The (0002) diffraction peak is weak in the ZnO-AG and enhanced substantially after annealing as the film crystallinity improves. For the oxidized Zn films (Zn-450ºC, Zn-550ºC, and Zn-650ºC), multiple diffraction peaks are observed and can be indexed to (11-20), (0002), (10-11), (10-12), (11-20), (10-13), and (11-22) planes of wurtzite ZnO since their XRD patterns are governed by the growth of crystalline nanorods along random directions on the substrate (see Figure 4.2). These XRD findings are consistent with the compositional and chemical state analysis results by XPS for both the ZnO and oxidized Zn film sets shown in Supplementary Material Figure 4.6, which confirms the successful conversion of the metallic Zn films to highly crystalline ZnO by oxidative annealing. Based on the higher intensity and narrower full width at half maximum (FWHM) of the (11-20), (0002), and (10-11) diffraction peaks, the Zn film annealed at 650 °C exhibits a slight improvement in crystallinity compared to the films annealed at 450 °C and 550 °C.

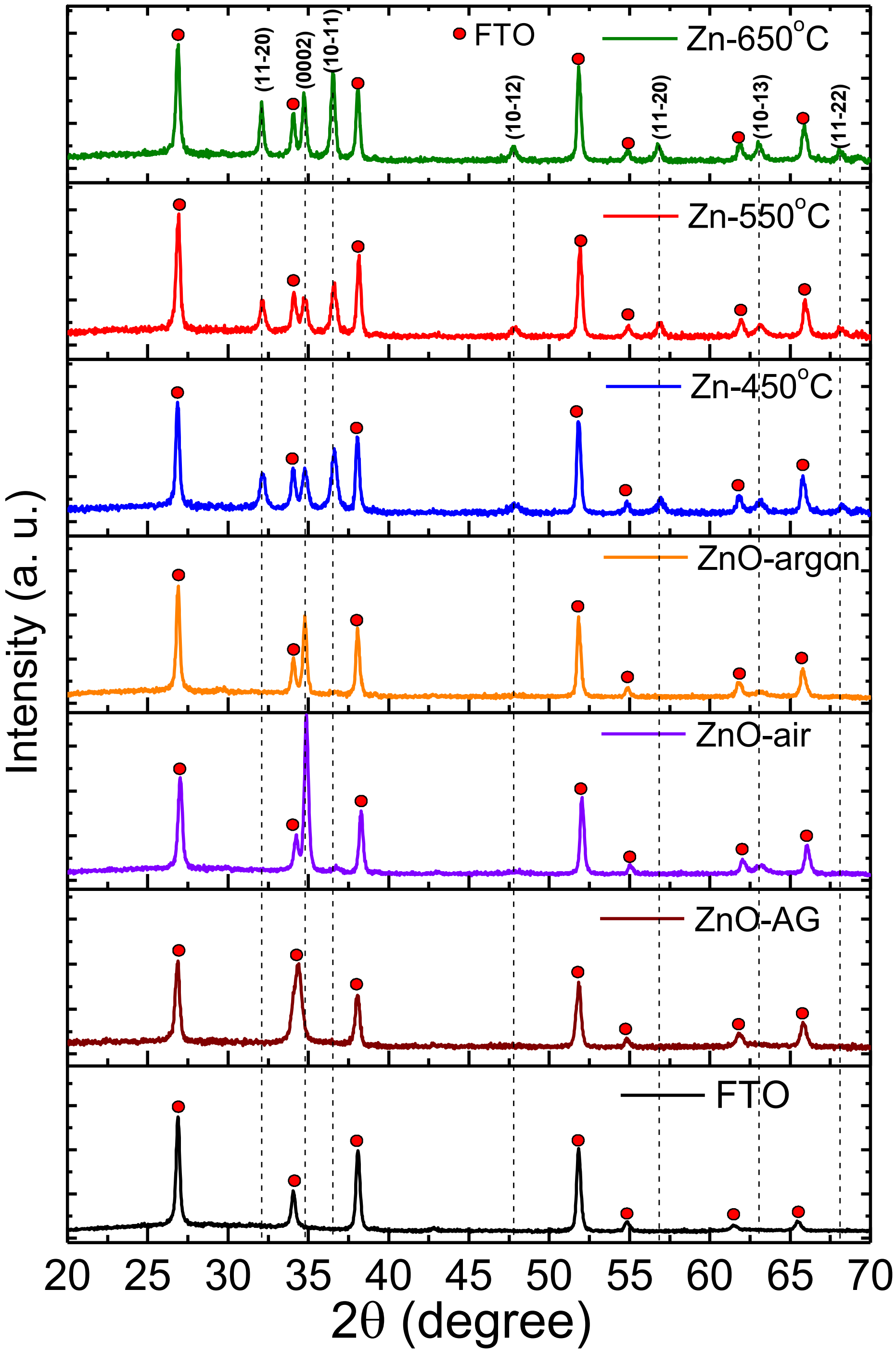

Figure 4.3. XRD patterns for the oxidized Zn and ZnO films. The peaks are indexed as follows: the red dots correspond to the FTO substrate while the dashed lines indicate reflections from the ZnO films. All the ZnO peaks can be identified as the wurzite phase of ZnO, indicating the successful conversion of the metallic Zn films (Zn-450ºC, Zn-550ºC and Zn-650ºC) to highly crystalline ZnO by oxidative annealing. The oxidized Zn films comprises of crystallites with multiple orientations such as (0002), (11-20), (10-11) and (11-20), while the ZnO films (ZnO-AG, ZnO-argon, and ZnO-air) have a predominantly (0002) growth orientation.

The optical properties of the ZnO films are determined using UV-Vis spectrometry [Figure 4.4(a, b)]. The ZnO films exhibit absorption only in the UV spectral region with a sharp absorption edge at 387 ± 3 nm (3.24 ± 0.02 eV from the Tauc plot extrapolation), close to the bandgap of bulk ZnO, while the optical absorption spectra of the oxidized Zn films display an exponential absorption edge over the visible spectral range. The extended absorption tails in the spectra of the Zn-450ºC, Zn-550ºC, and Zn-650ºC films can be attributed to light scattering in the nanostructured films and the Urbach tail effect [27] caused by band edge potential fluctuations produced by a high density of V_O defects. The light scattering effect in these films could be significant since the size of the nanorods is of the order of the wavelength of visible light. From the Tauc plot, the bandgap of these oxidized Zn films can be determined to be 3.01 ± 0.02 eV, which is significantly narrower than that of the ZnO films. The narrowed bandgap together with the exponential absorption edge enable these films to expand the absorption range thus enhances the PEC activity in the visible region.

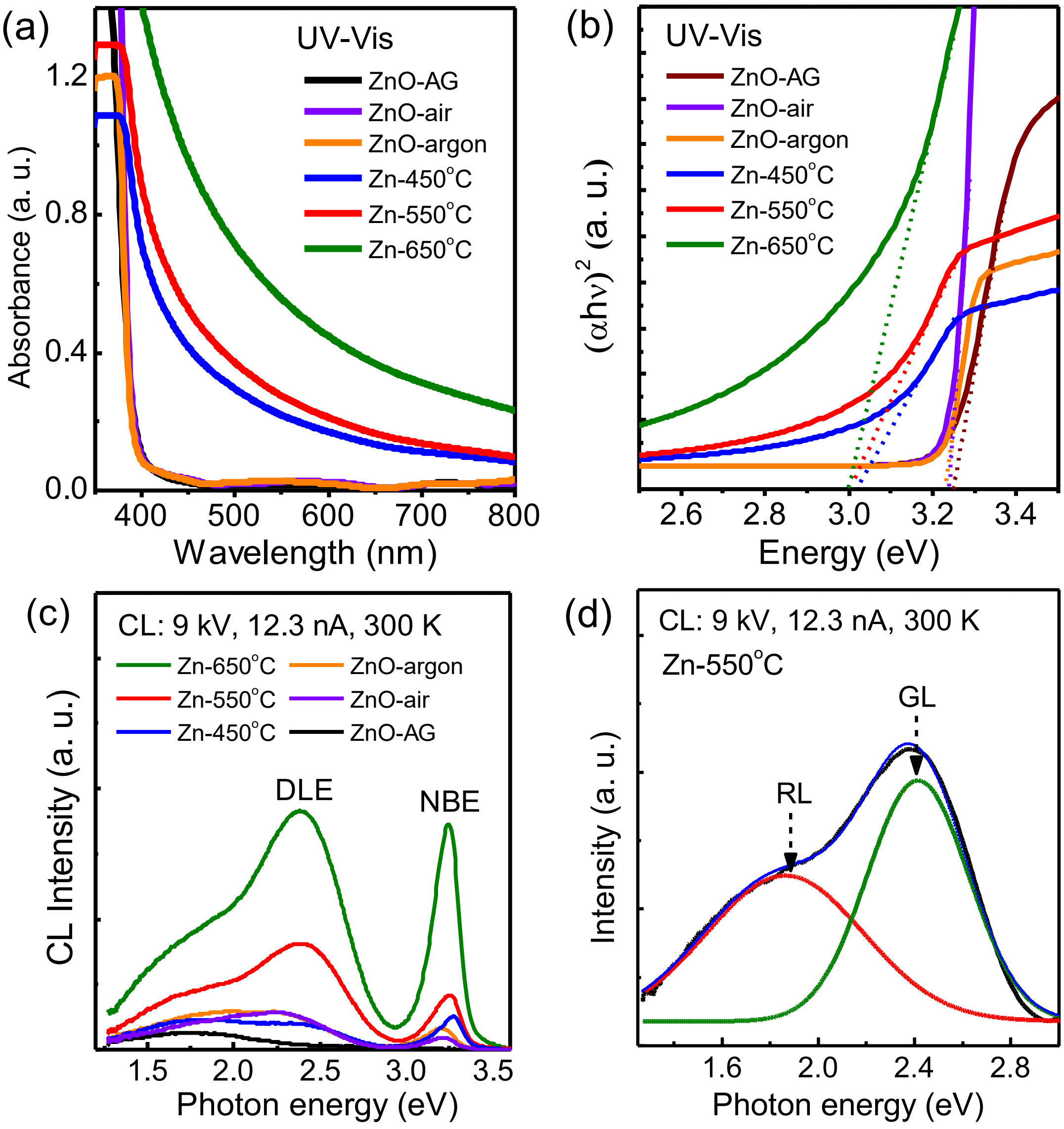

Figure 4.4. (a) UV-Vis absorption spectra measured from the as-grown and thermally annealed ZnO and oxidized Zn films at 450°C, 550°C and 650°C. The ZnO films exhibit a sharp optical absorption edge at 402 nm. In contrast, the spectra from the oxidized Zn films display an exponential absorption tail due to the presence of a high concentration of V_O defects. (b) Tauc plots for the films, yielding $E_g = 3.24 \pm 0.02$ eV and 3.01 ± 0.02 eV for the ZnO and oxidized Zn films, respectively. (c) CL spectra of the ZnO and oxidized Zn films acquired under identical conditions (300 K, 9 kV and 12.3 nA). The ZnO-AG film exhibits only a RL peak at 1.9 eV. Conversely, the other films exhibit three emission bands: UV at 3.3 eV, GL at 2.45 eV and RL at ~1.9 eV, attributed to NBE *e-h* recombination, V_O and V_{Zn}, respectively. (d) Gaussian fits of the deep-level emission for the oxidized Zn-550°C film. The Zn-550°C spectrum has the largest I_{GL}/I_{NBE} ratio (see Table 4.2), indicating that this film has the highest V_O density.

The defect structure in both the ZnO and oxidized Zn film sets is further studied using CL spectroscopy [Figure 4.4(c, d)]. All the films, except the ZnO-AG, exhibit a characteristic NBE emission at ~ 3.3 eV due to the radiative recombination of free excitons in wurtzite ZnO. The NBE emission is accompanied by a deep-level emission (DLE) comprised of a GL peak centred at 2.45 eV and a red luminescence (RL) shoulder at ~1.80 eV; these luminescence bands have previously been assigned to V_{O} and V_{Zn} defects, respectively.[28, 29] The ZnO-AG film displays only the RL and no NBE emission, indicating that this film contains an excess of V_{Zn} defects consistent with the oxygen-rich growth environment. The ZnO-air and ZnO-argon CL spectra show the presence of an NBE emission as defects are gradually annealed out. For the oxidized Zn films, the strong green emission indicates an abundance of V_{O} defects, which improves their light absorption capability as observed in the UV-Vis results. The strong GL emission observed in the oxidized Zn films confirms a high density of V_{O}. In wurtzite ZnO, V_{O} has three possible charge states: neutral V_{O}^{0}, singly ionized V_{O}^{+} and doubly ionized V_{O}^{2+}. Computational studies indicate that V_{O}^{+} exhibits negative U behavior and is unstable under thermal equilibrium [30]. Accordingly, V_{O}^{+} instantly transforms into its V_{O}^{0} or V_{O}^{2+} charge state by the gain or loss of an electron, depending on whether the ZnO Fermi level is above or below the $V_{\mathrm{O}}^{2+/0}$ CTL, respectively (see Figure 4.1). However, V_{O}^{0} is the thermodynamically stable charge state in the ZnO bulk due to its *n*-type nature with the Fermi level above the CTL. Conversely, V_{O}^{2+} states exist within the near surface region of the depletion layer due to the $V_{\mathrm{O}}^{2+/0}$ CTL bending above the ZnO Fermi level. In addition, it is widely reported that the ionized V_{O} signature GL emission intensity is strongest at the surface of ZnO nanowires.[31, 32] As a result, the measured GL emission in Figure 4.4(c) results from radiative recombination involving V_{O} defects. Here, a surface V_{O}^{2+} defect captures a free electron and converts into a V_{O}^{+} state with a deeply trapped electron that radiatively recombines with a photogenerated hole in the valence band, restoring the V_{O}^{2+} center and producing the GL (see Figure 4.1).[16, 23, 28, 33] Notably, the overall CL intensity of the oxidized Zn films increases with increasing annealing temperature as expected due to the improvement in film crystallinity and the associated removal of non-radiative defects, consistent with the XRD results as shown above. The DLE band is fitted with two Gaussian components to find the integrated intensities of the GL and RL bands for each of the ZnO photoanodes [Figure 4.4(d)]. The large variation of the GL and RL intensities in the ZnO films are evidenced in Table 4.2, which shows the $I_{\mathrm{GL}}/I_{\mathrm{NBE}}$ and $I_{\mathrm{RL}}/I_{\mathrm{NBE}}$ intensity ratios. The ZnO films possess larger I_{RL} than I_{GL} as the formation of V_{Zn} is favourable in oxygen-rich growth conditions. On the other hand, the GL is the dominant peak in the oxidized Zn films with the Zn-550°C film exhibiting the largest $I_{\mathrm{GL}}/I_{\mathrm{NBE}}$ ratio, which renders this film with its high V_{O} density suitable for PEC water oxidation. These CL point defect characterization findings are further supported by the oxidation state XPS analysis shown in Figure 4.6. As displayed in this figure, the O 1s spectra for the films can be deconvoluted into two peaks at 530.6 eV, which corresponds to O^{2-} ions in the wurtzite fully coordinated ZnO, and at 532.3 eV ascribed to O^{2-} ions with a V_{O} defect nearby.[34] The relative oxygen vacancy concentrations present in the films are estimated by obtaining the intensity ratio of the two deconvoluted peaks; this ratio is found to be $I(V_{\mathrm{O}})/I(\mathrm{O\text{-}Zn}) = 0.28$, 0.30, and 0.37 (± 0.2) for ZnO-air, ZnO-argon and Zn-550°C films, respectively. This result further confirms that the Zn-550°C film has a higher V_{O} concentration compared to the as-grown ZnO films.

4.3.2. PEC water splitting performance

The PEC performance of the ZnO photoanodes over the potential range of 0 – 1.4 V_{RHE} is shown in Figure 4.5(a) and the measured photocurrent density, I_{photo}, at 1.23 V_{RHE} is presented in Table 4.2. The ZnO-AG films show the lowest photocurrent density of 0.07 mA/cm^2 at 1.23 V_{RHE} due to their low film quality, consistent with the CL result that shows their optical properties are dominated by defects. The photocatalytic activity increases slightly to 0.13 and 0.34 mA/cm^2 at 1.23 V_{RHE} when the ZnO-AG film is annealed at 550°C in air (ZnO-air) and argon (ZnO-argon), respectively. This PEC performance enhancement could be attributable to the improvement in the film crystallinity, and possibly a higher density of V_O defects as revealed by the CL [see Figure 4.4(c)]. In comparison, the oxidized Zn photoanodes exhibit a three- to four-fold increase over the ZnO counterparts; at 1.23 V_{RHE}, the Zn-450°C and Zn-550°C photoanodes have a photocurrent density of 0.87 and 1.14 mA/cm^2, respectively. As discussed above, this remarkable improvement can be attributed to several factors. First, the oxidized Zn photoanodes have a much higher concentration of near-surface charged V_O defects. These reactive centres are known to act as preferential active sites for the surface adsorption of reactive oxygen species, such as H_2O, H and O_2, with their bonding at the V_O sites facilitating efficient charge transfer in the PEC process.[17, 18] Second, the V_O rich oxidized Zn films have a narrower bandgap due to the Urbach tail effect generating an exponential absorption edge that extends into the visible spectral range, improving light absorption efficiency of the photoanode under solar light irradiation. Third, the oxidized Zn films are comprised of nanorods with a large surface area that significantly increases the interaction between the electrolyte and ZnO photoanode. Notably, the oxidized Zn-650°C film has a lower photocurrent of 0.72 mA/cm^2 at 1.23 V_{RHE}, which is likely caused by thermal damage to the FTO substrate.[35]

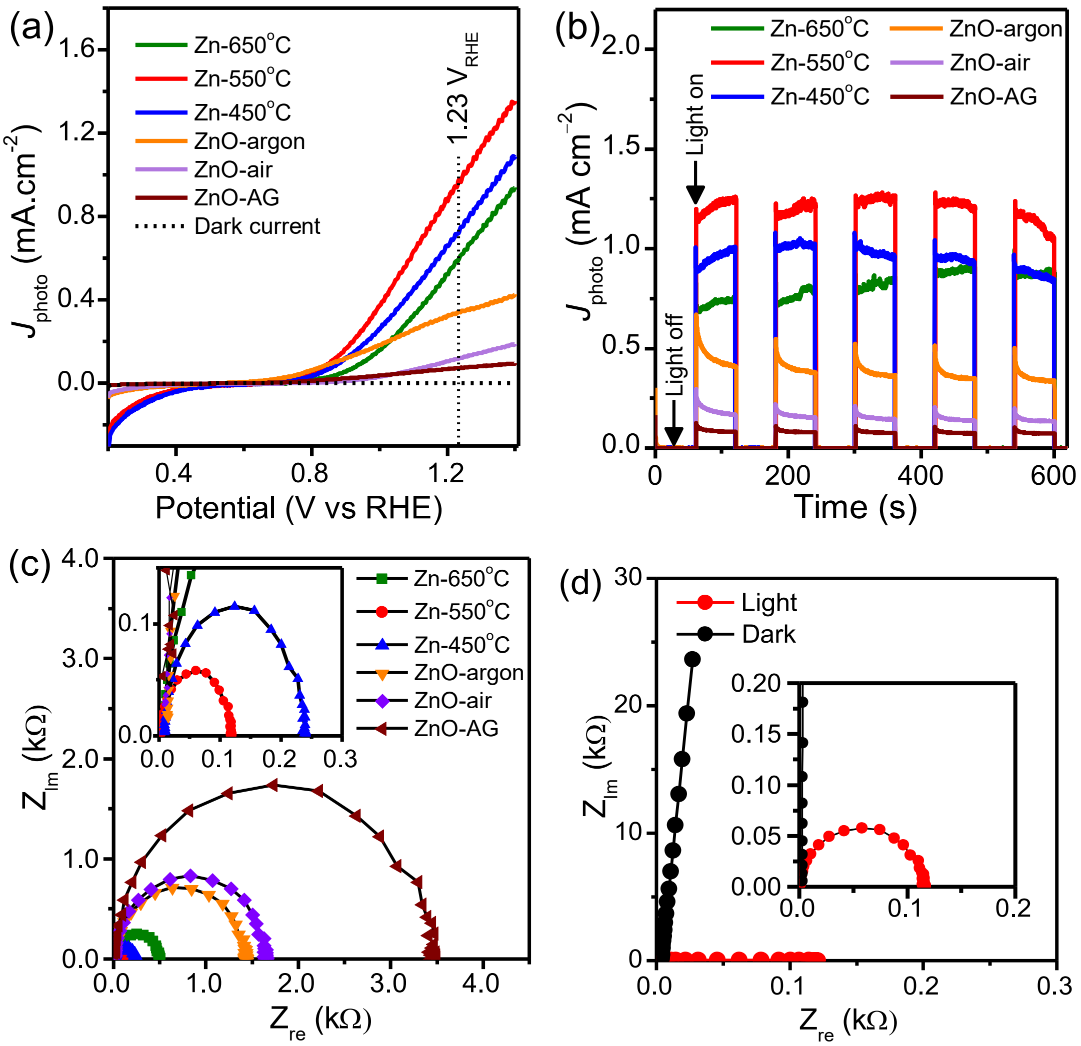

Figure 4.5. (a) Linear sweep voltammetry (LSV) plots, (b) chopped light chronoamperometry curves, and (c) Nyquist plots from impedance spectroscopy measurements for the ZnO and oxidized Zn photoanodes in 0.5M Na_2SO_4 aqueous solution and under 100 mW/cm^2 light intensity. The oxidized Zn photoanodes show a higher photocurrent density and lower charge transfer resistance, R_{ct}, compared with the ZnO counterparts. (d) Impedance spectroscopy of the Zn-550°C photoanode in the dark and under 1.23 V_{RHE} illumination. The resistance is extremely large in the dark, confirming that the photocurrent is generated by photogenerated *e-h* pairs induced by solar irradiation.

A chopped light chronoamperometry test reveals a similar photoactivity trend at 1.23 V_{RHE} under AM 1.5G solar simulator irradiation. Figure 4.5(b) shows the photocurrent density J_{photo}

versus time under on/off solar irradiation. In the absence of solar irradiation, all the photoanodes do not produce a measurable photocurrent. When the photoanode is illuminated, a large number of charge separated photoexcited carriers accumulate at the photoanode/electrolyte interface, resulting in the instantaneous generation of photocurrent spikes. Notably the Zn-550°C photoanode with the highest J_{photo} also contains the highest V_{O} density. With the annealed ZnO photoanodes, an exponential drop in photocurrent is observed with increasing light exposure time which is repeated after blanking the optical excitation cycle as shown in Figure 4.5(b). This decrease in the photocurrent could arise from shallow defects trapping the charge separated carriers producing an opposing electric field that screens the in-built surface field. In contrast, with the Zn-450ºC, Zn-550ºC, and Zn-650ºC photoanodes, following light exposure after the initial spike, the photocurrent slowly increases, saturates and maintains its intensity at re-exposure after most light-off cycles. These time dependent photocurrent kinetics are likely caused by the high density of ionized V_{O} defects being effective centers for carrier trapping and de-trapping, preventing free holes reaching the surface of the photoanode until a steady state condition is achieved.[36, 37]

The kinetics of the PEC process at the ZnO photoanode/electrolyte interface was assessed using the EIS technique at 1.23 $\mathrm{V_{RHE}}$ under 100 $\mathrm{mW/cm^2}$ light intensity and the Nyquist plots for the six photoanodes are shown in Figure 4.5(c). The semicircle diameter of the Nyquist plot represents the charge transfer resistance (R_{ct}), which is shown in Table 4.2 for both the ZnO and oxidized Zn photoanodes. For the ZnO-AG photoanode, the plot is an incomplete semicircle, indicating a very large R_{ct} value. While with the annealed ZnO samples $R_{\mathrm{ct}} = 1.66$ and 1.42 kΩ for the ZnO-air and ZnO-argon photoanodes, respectively. In comparison, the electrical impedance is an order of magnitude lower for the Zn-450ºC, Zn-550ºC, and Zn-650ºC photoanodes with $R_{\mathrm{ct}} = 0.24$, 0.12, and 0.50 kΩ, respectively. The relatively high R_{ct} for the Zn-650ºC photoanodes is likely due to the thermal damage of the FTO substrate caused by the high annealing temperature. The remarkably high electrical conductivity of the Zn-550ºC photoanode can be attributed to the high surface density of ionized V_O states, which creates a layer of holes at the photoanode/electrolyte interface as a result of the electric field across the depletion layer in the photoanode (see Figure 4.1). Moreover, the oxidized Zn films are comprised of randomly oriented nanorods with a large surface area that enhances its interaction with the electrolyte. The EIS of the Zn-550ºC sample was also measured both in the dark and under light exposure at 100 mW/cm^2 intensity [Figure 4.5(d)]. In the dark, the Nyquist plot is an incomplete semicircle and only a straight line is present due to very high resistance. This finding is consistent with the dark photocurrent exhibited in the LSV and chopped light chronoamperometry results [see Figure 4.5(a, b)], which confirms that the photocurrent is generated by photogenerated *e-h* pairs induced by solar irradiation and is not an electrochemical current. It also confirms the extremely high PEC activity of the Zn-550ºC photoanode.

4.3.3. Comparison with other ZnO photoanodes

The PEC performance of the optimized Zn film is compared with the reported results for ZnO photoanodes in the literature in Table 4.1. Comparison is made for photoanodes exposed to AM 1.5G sunlight and similar illumination conditions. As seen in the table, the Zn-550ºC film has a photocurrent density of 1.14 mA/cm^2 at 1.23V_{RHE}, which is higher than most previously reported for ZnO photoanodes in the literature. The superior performance of this film can be attributed to several factors. Firstly, it consists of randomly oriented nanorods, which provide a larger surface area for interaction with the electrolyte compared to ZnO films fabricated using conventional methods such as sputtering or chemical vapor deposition (CVD). These conventional techniques typically produce compact films with significantly lower surface area, as reported in previous studies [38-41]. The high-quality crystalline nanorods in the oxidized

Zn film exhibit a high density of ionized V_O defects, which facilitate efficient hole transport to the photoanode surface, enhancing water oxidation while suppressing electron-hole recombination. In comparison to previously reported ZnO nanostructures such as nanosheets, nanowires, and nanorods [15, 42-47], our ZnO films demonstrate a notably narrower bandgap of 3.0 eV. This reduction in bandgap is primarily attributed to an optimal density of oxygen vacancies, significantly improving visible light absorption capabilities. For example, ZnO prepared by Vairale et al. [43] exhibits a higher bandgap of 3.14 eV, characterized by a sharp absorption edge around 420 nm. In contrast, our ZnO films feature an extended absorption tail into the visible spectrum, a direct consequence of the enhanced density of V_O defects. Consequently, these superior structural and optical properties allow our ZnO films to more effectively utilize a broader range of solar radiation.

Table 4.1. Comparison of ZnO photoanodes and their PEC performances reported in the literature. Compared to previous reports, the Zn-550°C photoanode has excellent PEC performance with J_{photo} = 1.14 mA/cm^2 at 1.23 V vs RHE. This photocurrent density is the largest among the ZnO photoanodes investigated to date, which include nanostructured thin films produced by physical, chemical and chemo-physical methods.

Fabrication method	**Photoanode structure**	**J_{photo} (mA/cm^2)**	**Bias voltage (V)**	**Electrolyte**	**Light source**	**Ref.**
Oxidation of Zn films	Nanorods	1.14	1.23	0.5 M Na_2SO_4	AM 1.5G (100 mW/cm^2)	This work
Hydrothermal	Nanorods	~1.30	1.23	0.5 M Na_2SO_4	AM 1.5G solar	[44]
Chemical synthesis	Nanorods	0.705	1.23	0.5 M Na_2SO_4	AM 1.5G (100 mW/cm^2)	[15]
Dip coating	Nanorods	0.39	1.23	0.5 M Na_2SO_4	Xe lamp (100 mW/cm^2)	[45]
Aerosol assisted CVD	Thin film	0.3	1.1	0.1 M Na_2SO_4	AM 1.5G solar	[40]

RF sputtering	Thin film	0.25	1.23	0.1 M KOH	150 W Xe lamp	[38]
Chemical bath deposition	Nanosheets	0.2	1.23	–	300 W Xe lamp (100 mW/cm^2)	[43]
Chemical bath deposition	Nanowires	~0.15	1.23	0.1 M NaOH	UV lamp (11.5 mW/cm^2)	[48]
MOCVD	Nanowires	0.11	1.23	0.35 M Na_2SO_3 + 0.25 M Na_2S	300 W Xe lamp	[49]
DC reactive sputtering	Thin film	0.05	1.23	0.5 M Na_2SO_4	AM 1.5G solar	[39]
Hydrothermal	Nanowires	0.03	1.23	0.1 M Na_2S + 0.2 M NaOH	500 W Xe lamp	[47]
Hydrothermal	Nanorods	~0.01	1.23	0.1 M NaOH	–	[46]
Sol-gel coating	Thin film	0.005	1.00	0.5 M Na_2CO_3	500 W Xe lamp	[41]

4.4. Conclusions

This study demonstrates a facile, inexpensive method for fabricating V_O-rich ZnO photoanodes with high PEC activity under solar light irradiation. The method involves post-growth oxidation of a metallic Zn film, which produces a ZnO film comprised of randomly oriented nanorods that contain a high concentration of V_O defects. These nanostructured ZnO films are well suited as PEC photoanodes in water splitting applications due to their large surface area, strong optical absorption in the visible spectral range and charge transfer characteristics. Compared with previous reports on ZnO photoanodes, our V_O-rich ZnO photoanodes exhibit outstanding PEC performance with an exceptional photocurrent density of 1.14 mA/cm^2 at 1.23 V_{RHE}. Using correlative characterization techniques, we establish a direct relationship between the density of charged V_O defects in the subsurface region of ZnO photoanodes and their PEC activity. Our results demonstrate that the PEC efficiency and electrical conductivity of ZnO photoanodes can be considerably enhanced by controlling the surface defect structure to increase the generation and charge transfer of photoexcited carriers.

CRediT authorship contribution statement

Amar K. Salih: Conceptualization, Investigation, Formal analysis, Writing – original draft. **Matthew R. Phillips:** Data curation, Writing – review & editing. **Cuong Ton-That:** Formal analysis, Supervision, Writing – review & editing

Declaration of Competing Interest

The authors declare that they have no known competing financial interests or personal relationships that could have appeared to influence the work reported in this paper.

Supplementary data

Supplementary data to this paper is available in the appendix: C

Acknowledgements

The authors acknowledge the technical assistance of Curtis Irvine, Herbert Yuan and Mark Lockrey. This work was supported under Australian Research Council (ARC) Discovery Project funding scheme (project DP210101146).

4.5. References

[1] S.M. Fawzy, M.M. Omar, N.K. Allam, Photoelectrochemical water splitting by defects in nanostructured multinary transition metal oxides, Solar Energy Materials and Solar Cells 194 (2019) 184-194.

[2] M.D. Regulacio, M.-Y. Han, Multinary I-III-VI2 and I2-II-IV-VI4 semiconductor nanostructures for photocatalytic applications, Accounts of chemical research 49(3) (2016) 511-519.

[3] M.G. Walter, E.L. Warren, J.R. McKone, S.W. Boettcher, Q. Mi, E.A. Santori, N.S. Lewis, Solar water splitting cells, Chemical reviews 110(11) (2010) 6446-6473.

[4] M. Grätzel, Photoelectrochemical cells, Nature 414 (2001) 338-344.

[5] Y. Chen, X. Feng, Y. Liu, X. Guan, C. Burda, L. Guo, Metal oxide-based tandem cells for self-biased photoelectrochemical water splitting, ACS Energy Letters 5(3) (2020) 844-866.

[6] Z. Chen, H.N. Dinh, E. Miller, Photoelectrochemical water splitting, Springer2013.

[7] K. Shankar, J.I. Basham, N.K. Allam, O.K. Varghese, G.K. Mor, X. Feng, M. Paulose, J.A. Seabold, K.-S. Choi, C.A. Grimes, Recent advances in the use of TiO_2 nanotube and nanowire arrays for oxidative photoelectrochemistry, The Journal of Physical Chemistry C 113(16) (2009) 6327-6359.

[8] P. Qiu, F. Li, H. Zhang, S. Wang, Z. Jiang, Y. Chen, Photoelectrochemical performance of α-Fe_2O_3@NiOOH fabricated with facile photo-assisted electrodeposition method, Electrochimica Acta 358 (2020) 136847.

[9] H. Ennaceri, M. Boujnah, D. Erfurt, J. Rappich, X. Lifei, A. Khaldoun, A. Benyoussef, A. Ennaoui, A. Taleb, Influence of stress on the photocatalytic properties of sprayed ZnO thin films, Solar Energy Materials and Solar Cells 201 (2019) 110058.

[10] Y. Qiu, S.-F. Leung, Q. Zhang, B. Hua, Q. Lin, Z. Wei, K.-H. Tsui, Y. Zhang, S. Yang, Z. Fan, Efficient photoelectrochemical water splitting with ultrathin films of hematite on three-dimensional nanophotonic structures, Nano letters 14(4) (2014) 2123-2129.

[11] R. Pessoa, M. Fraga, L. Santos, M. Massi, H. Maciel, Nanostructured thin films based on TiO_2 and/or SiC for use in photoelectrochemical cells: A review of the material characteristics, synthesis and recent applications, Materials Science in Semiconductor Processing 29 (2015) 56-68.

[12] A.Y. Faid, N.K. Allam, Stable solar-driven water splitting by anodic ZnO nanotubular semiconducting photoanodes, RSC Advances 6(83) (2016) 80221-80225.

[13] M. Khelladi, L. Mentar, A. Beniaiche, L. Makhloufi, A. Azizi, A study on electrodeposited zinc oxide nanostructures, Journal of Materials Science: Materials in Electronics 24(1) (2013) 153-159.

[14] C. Klingshirn, ZnO: material, physics and applications, ChemPhysChem 8(6) (2007) 782-803.

[15] D. Commandeur, G. Brown, E. Hills, J. Spencer, Q. Chen, Defect-rich ZnO nanorod arrays for efficient solar water splitting, ACS Applied Nano Materials 2(3) (2019) 1570-1578.

[16] F. Kayaci, S. Vempati, I. Donmez, N. Biyikli, T. Uyar, Role of zinc interstitials and oxygen vacancies of ZnO in photocatalysis: a bottom-up approach to control defect density, Nanoscale 6(17) (2014) 10224-10234.

[17] S.-F. Duan, Y.-F. Ji, W. Wang, D.-F. Han, H.-Y. Wang, Q.-Y. Wei, C.-F. Li, F. Jia, D.-X. Han, L. Niu, Unraveling the Impact of Electrochemically Created Oxygen Vacancies on the Performance of ZnO Nanowire Photoanodes, ACS Sustainable Chemistry & Engineering 7(21) (2019) 18165-18173.

[18] J. Wang, R. Chen, L. Xiang, S. Komarneni, Synthesis, properties and applications of ZnO nanomaterials with oxygen vacancies: A review, Ceramics International 44(7) (2018) 7357-7377.

[19] T. Xia, P. Wallenmeyer, A. Anderson, J. Murowchick, L. Liu, X. Chen, Hydrogenated black ZnO nanoparticles with enhanced photocatalytic performance, RSC advances 4(78) (2014) 41654-41658.

[20] C. Wang, D. Wu, P. Wang, Y. Ao, J. Hou, J. Qian, Effect of oxygen vacancy on enhanced photocatalytic activity of reduced ZnO nanorod arrays, Applied Surface Science 325 (2015) 112-116.

[21] V. Kumar, M. Gohain, R. Kant, O. Ntwaeaborwa, P. Hari, H. Swart, V. Dutta, Annealing induced oxygen defects on green sonochemically synthesized ZnO nanoparticles for photoelectrochemical water splitting, ChemistrySelect 3(42) (2018) 11914-11921.

[22] H. Khan, S. Samanta, M. Seth, S. Jana, Role of Oxygen Defects on Photoelectrochemical Activity of ZnO Nanorods Grown on Transparent Conducting Oxide Thin Film, General Chemistry 6(3) (2020) 190025.

[23] P. Camarda, F. Messina, L. Vaccaro, S. Agnello, G. Buscarino, R. Schneider, R. Popescu, D. Gerthsen, R. Lorenzi, F.M. Gelardi, Luminescence mechanisms of defective ZnO nanoparticles, Physical Chemistry Chemical Physics 18(24) (2016) 16237-16244.

[24] A. Mohamedkhair, Q. Drmosh, M. Qamar, Z. Yamani, Nanostructured Magnéli-Phase $W_{18}O_{49}$ Thin Films for Photoelectrochemical Water Splitting, Catalysts 10(5) (2020) 526.

[25] S.B. Kale, A. Lokhande, R. Pujari, C. Lokhande, Effect of pretreatment on catalytic activity of cobalt sulfide thin film for oxygen evolution reaction, Materials Letters 228 (2018) 418-420.

[26] V. Chawla, N. Sardana, H. Kaur, A. Kumar, R. Chandra, S. Mishra, Effect of annealing parameters and activation top layer on the growth of copper oxide nanowires, Applied Surface Science 504 (2020) 144369.

[27] R. Rai, Analysis of the Urbach tails in absorption spectra of undoped ZnO thin films, Journal of Applied Physics 113(15) (2013) 153508.

[28] C. Ton-That, L. Weston, M. Phillips, Characteristics of point defects in the green luminescence from Zn-and O-rich ZnO, Physical Review B 86(11) (2012) 115205.

[29] S. Anantachaisilp, S.M. Smith, C. Ton-That, S. Pornsuwan, A.R. Moon, C. Nenstiel, A. Hoffmann, M.R. Phillips, Nature of red luminescence in oxygen treated hydrothermally grown zinc oxide nanorods, Journal of Luminescence 168 (2015) 20-25.

[30] A. Janotti, C.G. Van de Walle, Fundamentals of zinc oxide as a semiconductor, Reports on progress in physics 72(12) (2009) 126501.

[31] M. Foley, C. Ton-That, M.R. Phillips, Cathodoluminescence inhomogeneity in ZnO nanorods, Appl. Phys. Lett. 93(24) (2008) 243104.

[32] C. Ton-That, M. Phillips, Cathodoluminescence microanalysis of ZnO nanowires, Semiconductor Nanowires, Elsevier2015, pp. 393-407.

[33] T.J. Penfold, J. Szlachetko, F.G. Santomauro, A. Britz, W. Gawelda, G. Doumy, A.M. March, S.H. Southworth, J. Rittmann, R. Abela, Revealing hole trapping in zinc oxide nanoparticles by time-resolved X-ray spectroscopy, Nature Communications 9(1) (2018) 1-9.

[34] X. Wei, B. Man, M. Liu, C. Xue, H. Zhuang, C. Yang, Blue luminescent centers and microstructural evaluation by XPS and Raman in ZnO thin films annealed in vacuum, N_2 and O_2, Physica B: Condensed Matter 388(1-2) (2007) 145-152.

[35] E.S. Cho, M.J. Kang, Y.S. Kang, Enhanced photocurrent density of hematite thin films on FTO substrates: effect of post-annealing temperature, Physical Chemistry Chemical Physics 17(24) (2015) 16145-16150.

[36] Y. Huang, Y. Yu, Y. Yu, B. Zhang, Oxygen vacancy engineering in photocatalysis, Solar RRL 4(8) (2020) 2000037.

[37] P.M. Wojcik, L.D. Bastatas, N. Rajabi, P.V. Bakharev, D.N. McIlroy, The effects of sub-bandgap transitions and the defect density of states on the photocurrent response of a single ZnO-coated silica nanospring, Nanotechnology 32(3) (2020) 035202.

[38] Y. Lee, S. Kim, S.Y. Jeong, S. Seo, C. Kim, H. Yoon, H.W. Jang, S. Lee, Surface-Modified Co-doped ZnO photoanode for photoelectrochemical oxidation of glycerol, Catalysis Today 359 (2021) 43-49.

[39] H. Li, X. Li, W. Dong, J. Xi, G. Du, Z. Ji, Cu nanoparticles hybridized with ZnO thin film for enhanced photoelectrochemical oxygen evolution, Journal of Alloys and Compounds 768 (2018) 830-837.

[40] H.R. Khan, M. Aamir, B. Akram, A.A. Tahir, M.A. Malik, M.A. Choudhary, J. Akhtar, Superior visible-light assisted water splitting performance by Fe incorporated ZnO photoanodes, Materials Research Bulletin 122 (2020) 110627.

[41] F.S. Lim, S.T. Tan, Y. Zhu, J.-W. Chen, B. Wu, H. Yu, J.-M. Kim, R.T. Ginting, K.S. Lau, C.H. Chia, Tunable plasmon-induced charge transport and photon absorption of bimetallic Au–Ag nanoparticles on ZnO photoanode for photoelectrochemical enhancement under visible light, The Journal of Physical Chemistry C 124(26) (2020) 14105-14117.

[42] D. Maity, K. Karmakar, D. Pal, S. Saha, G.G. Khan, K. Mandal, One-Dimensional p-$ZnCo_2O_4$/n-ZnO Nanoheterojunction Photoanode Enabling Photoelectrochemical Water Splitting, ACS Applied Energy Materials 4(10) (2021) 11599-11608.

[43] P. Vairale, V. Sharma, B. Bade, A. Waghmare, P. Shinde, A. Punde, V. Doiphode, R. Aher, P. Subhash, S. Nair, Melanin sensitized nanostructured ZnO photoanodes for efficient photoelectrochemical splitting of water: synthesis and characterization, Engineered Science 11(2) (2020) 76-84.

[44] X. Long, T. Wang, J. Jin, X. Zhao, J. Ma, The enhanced water splitting activity of a ZnO-based photoanode by modification with self-doped lanthanum ferrite, Nanoscale 13(25) (2021) 11215-11222.

[45] J. Han, H. Xing, Q. Song, H. Yan, J. Kang, Y. Guo, Z. Liu, A ZnO@CuO core–shell heterojunction photoanode modified with ZnFe-LDH for efficient and stable photoelectrochemical performance, Dalton Transactions 50(13) (2021) 4593-4603.

[46] P. Sahoo, A. Sharma, S. Padhan, R. Thangavel, Visible light driven photosplitting of water using one dimensional Mg doped ZnO nanorod arrays, International Journal of Hydrogen Energy 45(43) (2020) 22576-22588.

[47] Y. Lin, S. Liu, Robust ZnO nanowire photoanodes with oxygen vacancies for efficient photoelectrochemical cathodic protection, Applied Surface Science 566 (2021) 150694.

[48] K. Govatsi, G. Syrrokostas, S. Yannopoulos, S. Neophytides, Optimization of aluminum doped ZnO nanowires for photoelectrochemical water splitting, Electrochimica Acta 392 (2021) 138995.

[49] I.V. Bagal, S. Jun, M. Choi, A. Abdullah, A. Waseem, S. Ahn, M.A. Kulkarni, Y.-H. Cho, S.-W. Ryu, Investigation of charge carrier dynamics in beaded ZnO nanowire decorated with SnS_2/IrO_x cocatalysts for enhanced photoelectrochemical water splitting, Applied Surface Science 613 (2022) 156091.

4.6. Appendix C: Additional surface chemistry and cathodoluminescence data

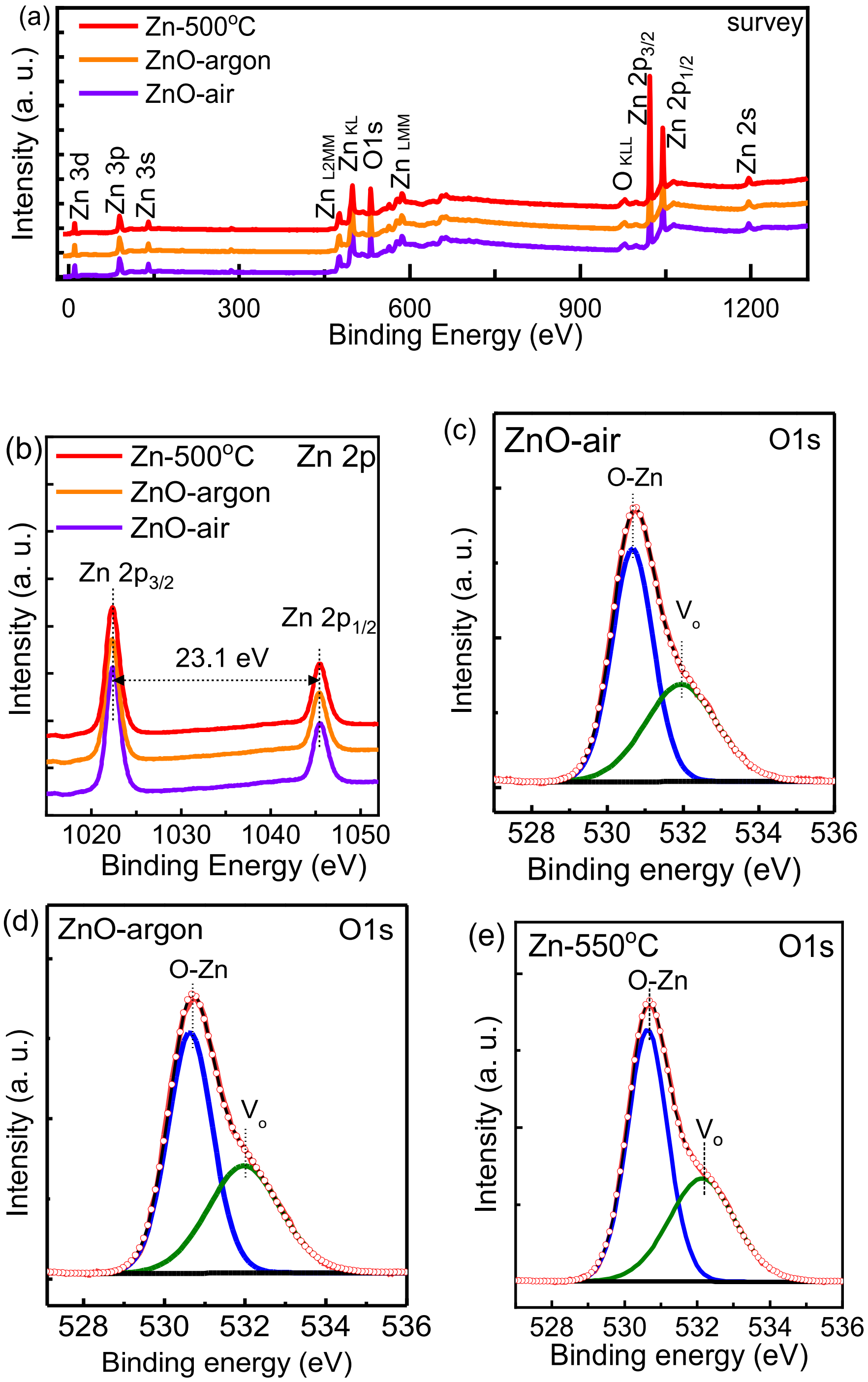

Figure 4.6. Surface chemical analysis of the ZnO and oxidized Zn film sets by XPS. Figure 4.6(a) presents the XPS survey spectra of the ZnO-air, ZnO-argon and Zn-550°C samples. All the XPS peaks can be attributed to Zn and O without any other impurities. The high-resolution Zn 2p spectra of the films show the characteristic doublet peaks with binding energies of

1022.4 eV (Zn 2p$_{3/2}$) and 1045.6 eV (Zn 2p$_{1/2}$) with spin-orbit splitting energy of 23.1 eV [Figure 4.6(b)], manifesting the presence of Zn^{2+} oxidation state.[50] Notably, the as-grown ZnO and thermally annealed Zn films have the same Zn 2p binding energies, which confirms the complete transformation of metallic Zn to ZnO (Zn^0 to Zn^{2+}) by post-growth thermal oxidation. Figure 4.6(c-e) displays the O 1s spectra of the films fitted with two Gaussian peaks at 530.6 and 532.3 eV peaks corresponding to O^{2-} ions in the fully coordinated ZnO and O^{2-} ions with a nearby V_O, respectively.[34] It is worth noting that because the films were etched with Ar$^+$ ions before XPS analysis, the generally observed O 1s peak centred at ~ 534.2 eV due to surface absorbed oxygen species, such as OH, H_2O and O_2, is not present in the measured XPS spectra. The V_O/O-Zn ratio, obtained using the integrated intensity of the fitted peaks, is found to be 0.28, 0.30, and 0.37 (± 0.2) for the ZnO-air, ZnO-argon and Zn-550°C films, respectively. This result provides further evidence that the thermally annealed Zn film has a higher V_O concentration compared with the as-grown ZnO films.

Table 4.2. Summary of the CL intensity ratios of I_{GL}/I_{NBE} and I_{RL}/I_{NBE}, photocurrent density, and charge transfer resistance, R_{ct}, for the investigated ZnO photoanodes. The ZnO-AG has no NBE emission and an immeasurably large R_{ct}.

Film	I_{GL}/I_{NBE}	I_{RL}/I_{NBE}	J_{photo} **(mA/cm^2) at 1.23V$_{RHE}$**	R_{ct} **(kΩ)**
Zn-650°C	2.1	2.1	0.72	0.50
Zn-550°C	4.3	3.9	1.14	0.12
Zn-450°C	1.8	2.5	0.87	0.24
ZnO-argon	2.2	5.5	0.34	1.42
ZnO-air	1.8	4.9	0.13	1.66
ZnO-AG	–	–	0.07	–

References

[50] R. Al-Gaashani, S. Radiman, A. Daud, N. Tabet, Y. Al-Douri, XPS and optical studies of different morphologies of ZnO nanostructures prepared by microwave methods, Ceramics International 39(3) (2013) 2283-2292.

Chapter 5. Defect passivation and enhanced UV emission in β-Ga_2O_3 via remote fluorine plasma treatment

In this chapter, we investigate the impact of fluorine doping on the native defects in β- Ga_2O_3 nanowires (NWs). These defects play a significant role in influencing the electronic and optical properties of Ga_2O_3 crystals. We explore the interaction between fluorine species (atoms and radicals) generated by SF_6 plasma dissociation and the native defects in Ga_2O_3 NWs. Our findings highlight the crucial role of F doping in modulating carrier dynamics and enhancing UV emission in β-Ga_2O_3, providing new insights for advancing deep UV optoelectronics in environmental applications.

Abstract

This study investigates the incorporation of fluorene (F) donors in β-Ga_2O_3 and its effects on luminescence, defect structure and carrier dynamics. Monoclinic β-Ga_2O_3 nanowires (NWs) are synthesized via chemical vapor deposition and subsequently doped with F using remote SF_6 plasma treatment, leveraging their nanoscale cross sections. Photoelectron spectroscopy reveals F incorporation at oxygen sites and the formation of strong Ga–F bonds without sulfur contamination, while the monoclinic crystal structure remains intact. The impact of F doping is assessed using hyperspectral cathodoluminescence (CL) mapping and time-resolved spectroscopy of individual NWs. The β-Ga_2O_3 NWs exhibit a strong characteristic UV peak at 3.40 eV, associated with self-trapped holes, and visible defect-related emissions. After F incorporation, an additional UV emission at 3.64 eV emerges, attributed to shallow F donor-deep acceptor pair recombination, while the defect-related emissions are strongly suppressed as F atoms occupy oxygen vacancies. Carrier lifetime increases from 9.2 ns to 17.0 ns with increasing F concentration along the nanowire. The work highlights the utility of F plasma

processing to passivate intrinsic defects in Ga_2O_3 and the influence of F donors on the UV emission of β-Ga_2O_3.

Keywords: β-Ga_2O_3 nanowires; fluorine doping; defect passivation; carrier dynamics; hyperspectral imaging

5.1. Introduction

Monoclinic β-Ga_2O_3 is currently attracting significant attention as an emerging semiconductor due to its exceptional properties, including a large bandgap of 4.9 eV, an extremely high breakdown field of ~ 8 MV/cm, high electron mobility and remarkable thermal stability. This unique combination of physical and material properties makes β-Ga_2O_3 a strong candidate for the development of the next generation optoelectronic devices, with potential applications in UV transparent electrodes, solar-blind photodetectors, field-effect transistors, deep UV emitters as well as spintronic and power electronics [1-3]. The ultra-high breakdown field of β-Ga_2O_3 and suitability for mass production makes β-Ga_2O_3 especially useful for the development of energy efficient, low-cost high-power devices, potentially exceeding the performance of the currently employed electronics that utilize SiC and GaN based technologies.

Doping electronic oxides such as Ga_2O_3 presents challenges such as compensation effects, solubility limitations and defect formation. These oxides typically exhibit conductivity asymmetry, favouring n-type behavior. While initial theoretical studies proposed that unintentional n-type doping in Ga_2O_3 could be linked to oxygen vacancies (V_O), Varley *et al.* [4] used hybrid density function theory (DFT) calculations to demonstrate that V_O acts as a deep donor and does not contribute to n-type conductivity. Furthermore, other studies reinforce the view that most native defects and their complexes have minimal impact on electrical conductivity [5, 6]. Dopants such as silicon, zinc, nitrogen, tin, chlorine, and fluorine have been explored as possible shallow donors in Ga_2O_3 [5, 7-10]. Group IV elements (Si, Ge, Sn) are expected to substitute Ga cation sites, while group VII elements (Cl, F) occupy O anion sites. The monoclinic structure of Ga_2O_3 contains two different Ga sites (tetrahedral $Ga_{(I)}$ and octahedral $Ga_{(II)}$) and three distinct tetrahedral oxygen sites (two three-fold coordinated $O_{(I)}$ and $O_{(II)}$, and one with four-fold coordinated ($O_{(III)}$). DFT calculations show that on the Ga sites, Si and Ge prefer the $Ga_{(I)}$ site and Sn favors the $Ga_{(II)}$ site, whereas on the O anion sites Cl and F occupy the $O_{(I)}$ site [11]. Studies have demonstrated that F doping significantly influences the electrical properties of β-Ga_2O_3-based devices. For instance, in β-Ga_2O_3 MOSFETs, Jeong et al. [12] reported that F doping enhances ohmic contact formation, leading to decreased specific resistivity and contact resistance. Additionally, F doping increases carrier concentration across the surface and bulk of the device. Another theoretical study reveals that F doping imparts n-type semiconductor properties to β-Ga_2O_3, evidenced by a Fermi level shift into the conduction band and a progressive narrowing of the band gap with increased F concentration [13]. These studies suggest that F doping can effectively tune the electrical properties of β-Ga_2O_3, potentially expanding its application in electronic and optoelectronic devices.

β-Ga_2O_3 exhibits luminescence across the UV–visible spectrum in both bulk and nanostructured forms [14, 15]. The optical emission bands, spanning from 1.8 eV to 3.8 eV, strongly depend on sample morphology, growth conditions and doping. These emission peaks are categorized into four distinct spectral regions: UV, blue (BL), green (GL), and red (RL) luminescence [15-17]. Notably, a near-band-edge (NBE) emission is absent in β-Ga_2O_3 due to the rapid formation of self-trapped holes (STHs), which radiatively recombine to produce an UV emission [18, 19]. In nominally undoped β-Ga_2O_3 crystals, UV emission dominates at low temperatures, whereas BL, GL and RL bands become prevalent at room and elevated temperatures due to the thermalization of self-trapped excitons [15, 16]. The visible peaks are associated with native defects, such as oxygen (V_O) and gallium (V_{Ga}) vacancies [14], as well as donor-acceptor pairs (DAPs) involving acceptors like V_{Ga} and V_{Ga}–V_O complexes [16].

This study investigates the effects of SF_6 plasma treatment on the doping of Ga_2O_3 nanowires (NWs) and elucidates the interactions between fluorine species (atoms, radicals generated by SF_6 plasma dissociation) and native defects in β-Ga_2O_3 NWs. We provide fundamental insights into fluorine passivation mechanisms in β-Ga_2O_3, showing that F can substitute oxygen atoms and occupy V_O sites, where it interacts with Ga dangling bonds. Additionally, due to their high electronegativity, fluorine anions on the Ga_2O_3 surface may attract hydrogen atoms, promoting the formation of intermolecular hydrogen F-OH bonds. Passivating oxygen vacancies by fluorine atom occupation and reducing the number of dangling Ga bonds can significantly improve Ga_2O_3 device performance by decreasing the density of carrier trap states.

5.2. Materials and methods

β-Ga_2O_3 NWs were synthesized on Au-coated Si(100) substrates via the chemical vapor deposition (CVD) method. A 5 nm Au layer was coated on Si(100) substrate using a sputter coated. The substrate and high-purity Ga (99.99%) source were placed in a quartz tube and heated to 850°C for 30 minutes at ~1 Torr pressure. A constant flow of Ar at 200 sccm and O_2 at 2 sccm, controlled by a mass flow controller (MFC), transported the Ga precursor to the substrate, facilitating the growth of Ga_2O_3 nanowires (NWs). F-doping was achieved by exposing the NWs to SF_6 gas using an inductively coupled plasma (ICP) system. During this process, the SF_6 gas flow was maintained at 30 sccm, while the RF power was set to 300 W to ionize the gas. The bias power was kept at zero to minimize etching effects. The SF_6 plasma treatment was conducted for 2 hours. Scheme 5.1 depicts the fabrication steps of F:Ga_2O_3 NWs.

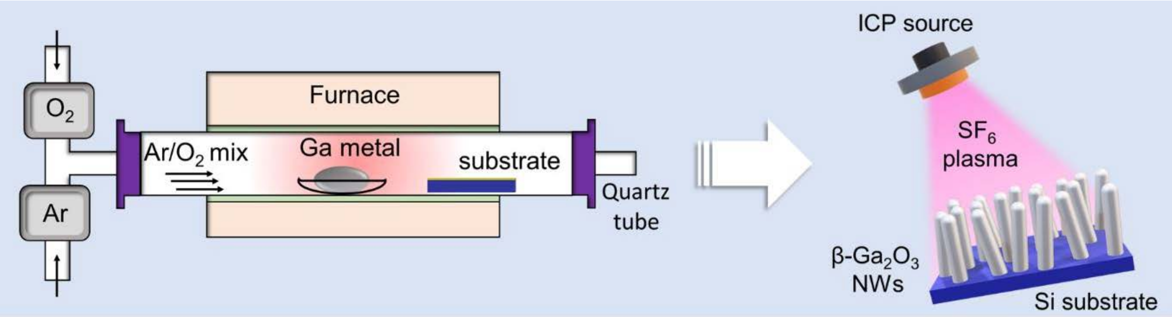

Scheme 6.1. Experimental method for growth of F:Ga_2O_3 NWs synthesized on Au-coated Si substrate.

Both untreated and F-doped Ga_2O_3 (F:Ga_2O_3) NWs were characterized using a range of analytical techniques. A Zeiss Supra 55VP field emission scanning electron microscope (SEM) equipped with an Oxford Instruments EDS was used for morphological and elemental analysis. The crystal structure was confirmed using a Bruker D8 Discovery X-ray diffractometer (XRD) with Cu Kα radiation, employing a 0.02° scanning step. X-ray photoelectron spectroscopy (XPS) was performed on the Soft X-ray Spectroscopy (SXS) beamline at the Australian Synchrotron. Cathodoluminescence (CL) spectroscopy was conducted using a FEI Quanta FEG 650 SEM (Thermo Fisher Scientific Inc., MA, USA). CL spectra were collected by a parabolic mirror and analyzed with a Delmic SPARC CL detector coupled with an Andor Newton charge-coupled device (CCD) camera. Hyperspectral CL maps were acquired with a 5 keV electron beam, a beam current of 85 pA and 100 ms acquisition time. For the time-resolved CL (TR-CL) measurements, an electrostatic beam blanker together with a 70 μm aperture was inserted to generate pulsed electron beam excitation with a pulse duration of approximately 90 ps [20].

5.3. Results and discussion

SEM images of the Ga_2O_3 NWs are presented in Fig. 5.1(a). The NWs are densely populated and uniformly distributed across an entire 10 × 10 mm^2 area of the substrate, exhibiting NW lengths of a few tens of microns and diameters ranging from 300 to 500 nm. EDS elemental mapping and spectra are shown in Fig. 5.1(b, c). Upon SF_6 plasma treatment, the EDS elemental mapping of single nanowires reveals that the F distribution is spatially correlated with that of Ga atoms, confirming successful F incorporation throughout the Ga_2O_3 NWs [Fig. 5.1(b)]. Additionally, the EDS spectra of the NWs show characteristic Ga and O X-ray peaks, along with an F peak following the SF_6 plasma treatment. The absence of Au is consistent with the growth model for a combined vapor–solid (VS) and vapor–liquid–solid (VLS) mechanism [21]. Moreover, upon SF_6 ionization inside the ICP chamber, SF_x^- ions and F radicals are produced and subsequently adsorbed by the Ga_2O_3 NWs. This process might result in formation of non-volatile GaF_x particles on the surface, while the vaporized SO_y species are exhausted. The reaction between the Ga_2O_3 NWs and SF_6 gas could be described by the following equation; $Ga_2O_3 + SF_6 = GaF_x(s) + SO_y(g)$ [22]. This explains the absence of sulfur (S) in the EDS results and the formation of S-free F:Ga_2O_3 NWs, consistent with other materials doped via SF_6 plasma treatment [23, 24]. Furthermore, since the SF_6 ICP was conducted at zero bias voltage, the diffusion of the F radicals across the NW sample depth wasn't completely uniformed as shown in Figure 5.5. The normalized EDS spectra reveal a progressive increase in the relative intensity ratio between the F Kα and Ga Lα X-ray peaks (I_F/I_{Ga}) from the root ($I_{F(root)}/I_{Ga(root)} = 3.3\%$) to the middle ($I_{F(middle)}/I_{Ga(middle)} = 4.7\%$) and the tip ($I_{F(tip)}/I_{Ga(tip)} = 8.9\%$). This indicates that the fluorine concentration is highest at the tip, followed by the middle, and lowest at the root of the NW.

Figure 5.1(d) presents the XRD patterns of Ga_2O_3 and F:Ga_2O_3 NWs, confirming the growth of high-quality monoclinic β-Ga_2O_3, consistent with previous reports [25]. No additional peaks corresponding to any impurity phases, such as GaF_3, are detected in the XRD pattern of F:Ga_2O_3 [26], indicating that F is primarily incorporated into the Ga_2O_3 lattice. Nevertheless, the possible GaF_x surface layer might be too thin to produce detectable XRD signals. While XRD peaks along the (002), (111), and (-311) planes are prominent, no preferred orientation can be discerned, indicating that the NWs grow randomly with respect to the substrate normal. The XRD patterns of the Ga_2O_3 and F:Ga_2O_3 NWs are nearly identical, with only slight variations in relative peak intensities, confirming that the F incorporation does not induce secondary phases and has a minimal impact on the crystalline quality of the NWs.

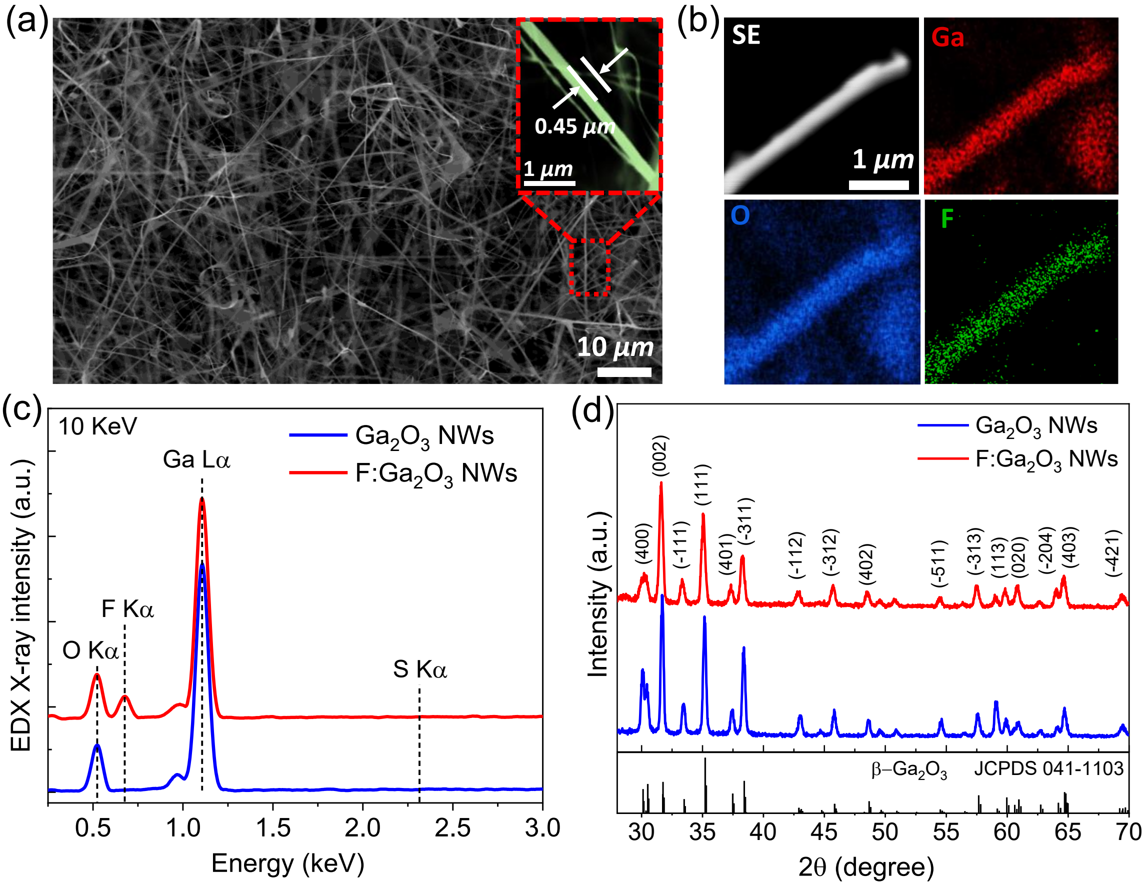

Figure 5.1. (a) SEM image of Ga_2O_3 NWs grown over an entire area of 10 ´ 10 mm^2, with an average NW diameter ranging from 300 to 500 nm. (b) SEM image and corresponding EDS elemental maps of Ga, O, and F for an individual F-doped NW, showing the incorporation of fluorine along the NW length. (c) EDS spectra of the NWs, showing the characteristic F Ka X-ray peak at 0.70 keV in F:Ga_2O_3 NWs, while the S Ka X-ray peak at 2.3 eV is completely absent. (d) XRD patterns of Ga_2O_3 and F:Ga_2O_3 NWs with all peaks indexed to the b-Ga_2O_3 monoclinic structure.

XPS measurements conducted on the Ga_2O_3 and F:Ga_2O_3 NWs confirm the incorporation of fluorine into Ga_2O_3 NWs. Survey spectra acquired at a photon energy hν = 1486.6 eV for

Ga_2O_3 and F:Ga_2O_3 NWs [Fig. 5.2(a)] show the characteristic photoelectron and Auger peaks for Ga and O, with an additional F 1s peak at 683.2 eV in the F:Ga_2O_3 spectrum, confirming successful fluorine doping. Importantly, no sulfur contamination is detected, as evidenced by the absence of S 2p (at ~ 164 eV) and S 2s (~ 225 eV) signals, corroborating the EDS results. Figure 5.2(b) shows the Ga 2p spectrum for Ga_2O_3 NWs, fitted with two doublet peaks at 1117.8 eV (Ga $2p_{3/2}$) and 1144.9 eV (Ga $2p_{1/2}$), with an energy separation of 27.1 eV, consistent with Ga–O bonds of β-Ga_2O_3 [27]. For F:Ga_2O_3 NWs [Fig. 5.2c], additional doublet peaks appear at 1120.8 eV and 1147.6 eV indicate the formation of Ga–F bonds. The emergence of F-related XPS peaks indicates the incorporation of fluorine atoms into the Ga_2O_3 NWs [28]. According to Liu et al. [29], the formation energy of interstitial fluorine atoms (F_i) is significantly higher than that of substitutional fluorine atoms (F_O). This suggests that the incorporated fluorine atoms into the Ga_2O_3 NWs are primarily substituting oxygen atoms or occupying oxygen vacancy (V_O) sites, rather than forming interstitial configurations. Due to the similar ionic radii of fluorine and oxygen, fluorine can integrate into the Ga_2O_3 lattice with minimal structural distortion [30]. Surface-sensitive XPS at hν = 120 eV further reveals heavy fluorination at the NW surface. Figure 5.6 presents the valence band (VB) spectra for Ga_2O_3 and the Ga 3d core level, corresponding to Ga-O bonding [31]. In F:Ga_2O_3 NWs, a new peak at 24.8 eV emerges, attributed to the formation of Ga–F bonds. The F doping also induces a notable shift in the VB onset from 3.2 eV to 2.5 eV, which is likely due to the formation of F_O shallow donors in the Ga_2O_3 NWs. This VB shift may also arise from to the passivation of surface states by fluorine [28]. The presence of F peaks at a photon energy of 1486.6 eV and 120 eV confirms the incorporation of fluorine into both the surface and sub-surface regions of the nanowires (NWs). These peaks correspond to sampling depths of 7.2 nm and 1.5 nm, respectively, indicating that fluorine is distributed across the outermost surface and extends into the near-surface layers of the NWs [32]. The O 1s core level spectra of Ga_2O_3 and F:Ga_2O_3

NWs are shown in Fig. 5.2(d, e). The O 1s spectrum is deconvoluted into two peaks at 530.6 eV [$O_{(I)}$] and 532.2 eV [$O_{(II)}$], attributed to Ga–O bonds and surface –OH groups, respectively [30]. The increased intensity of $O_{(II)}$ in F:Ga_2O_3 NWs indicates enhanced adsorption of –OH groups, likely due to the high electronegativity of fluorine, which can attract hydrogen, resulting in the formation of intermolecular F–HO hydrogen bonds [28]. The F 1s spectrum of F:Ga_2O_3 NWs, presented in Fig. 5.2(f), reveals two Gaussian-fitted components at 685.9 and 688.6 eV. The peak at 685.9 eV corresponds F–Ga bonds, while the higher-energy peak at 688.6 eV is attributed to F–HO interactions [30, 33].

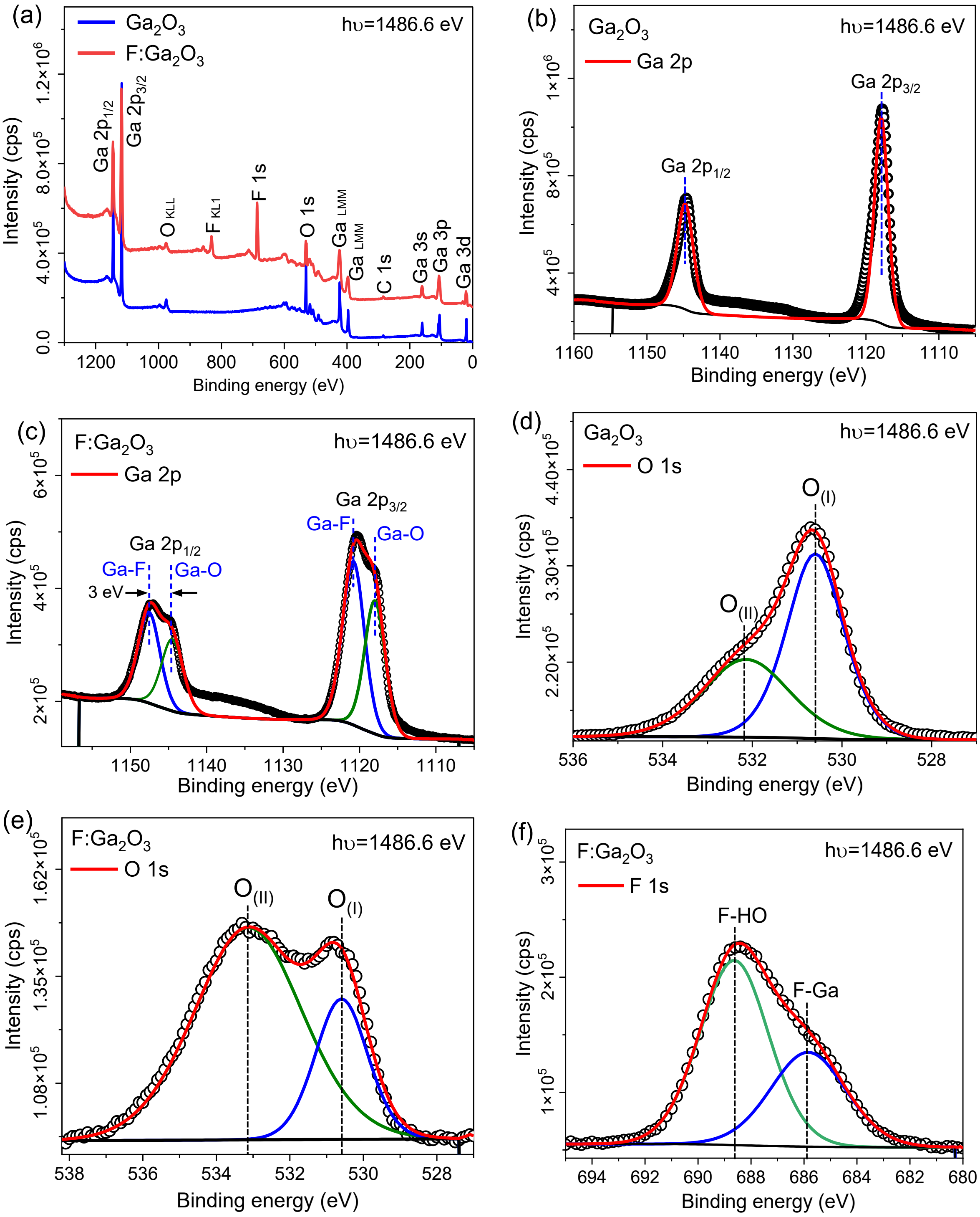

Figure 5.2. (a) XPS survey spectra of Ga_2O_3 and F:Ga_2O_3 NWs acquired at h*ν* = 1486.6 eV, showing a pronounced F 1s peak after the plasma doping, with no detectable sulfur signals. (b, c) Ga 2p core level spectra revealing the formation of Ga–F bonds. (d, e) O 1s spectra deconvoluted into two peaks assigned to O–Ga bonds [$O_{(I)}$] and oxygen–hydroxyl (O–OH) bonds [$O_{(II)}$]. The $O_{(II)}$ intensity increases significantly in F:Ga_2O_3 NWs I attributed to –OH adsorption, driven by the high electronegativity of F ions. (f) F 1s spectrum for F:Ga_2O_3, fitted into two peaks corresponding to F–Ga and F–HO bonds.

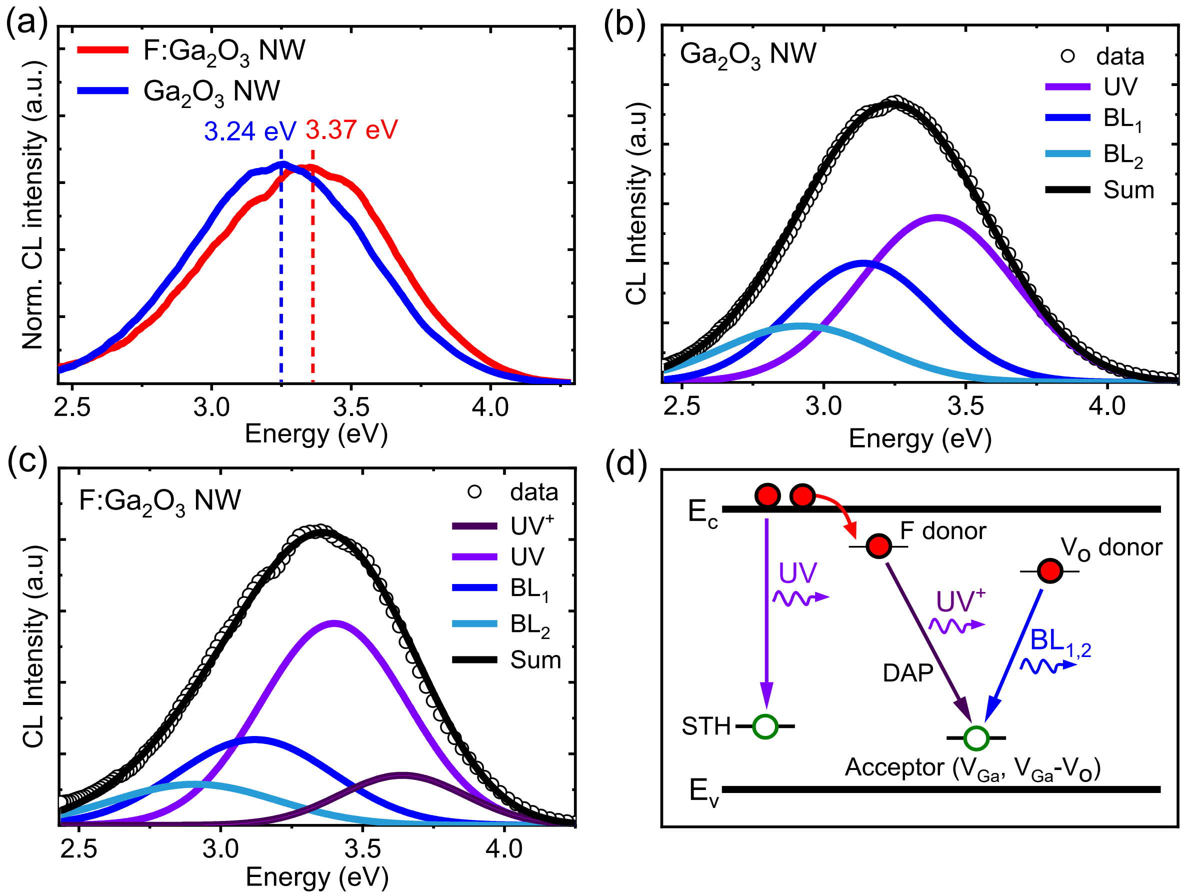

Figure 5.3. (a) Normalized CL spectra of Ga_2O_3 and F:Ga_2O_3 NWs acquired under identical excitation conditions (5 kV and 85 pA). The F doping induces a blue shift of 0.13 eV in the luminescence spectrum. (b, c) CL spectral deconvolution for Ga_2O_3 and F:Ga_2O_3, revealing three luminescence bands: UV at 3.40 eV, BL_1, and BL_2, and an additional higher-energy band at 3.64 eV (UV^+) emerging after F doping. Both BL_1 at 3.14 eV and BL_2 at 2.93 eV decrease in relative intensity in F:Ga_2O_3 NWs. (d) Schematic emission model for Ga_2O_3 and F:Ga_2O_3 NWs, showing radiative recombination through the STH (UV band), DAP transitions (BL_1 and BL_2 bands), and DAP involving F donors (UV^+ band).

The effects of fluorine incorporation on the luminescence properties of Ga_2O_3 are analyzed using hyperspectral CL imaging and spectroscopy analysis of individual NWs (Fig. 5.3a). The F doping induces a notable blue shift in the CL emission, shifting from 3.24 eV for undoped Ga_2O_3 to 3.37 eV for F:Ga_2O_3. This 130 meV shift is attributed to a new additional emission arising from F-related shallow donors, which can be analysed through Gaussian peak fitting as previously reported for β-Ga_2O_3 [34, 35]. In monoclinic β-Ga_2O_3, the STH and defect-related CL peaks overlap significantly as both emissions are inherently broad due to strong electron-photon coupling, necessitating spectral deconvolution to interpret the luminescence data meaningfully [15]. Applying this approach, the CL spectrum of Ga_2O_3 NWs is deconvoluted into three Gaussian peaks: UV, BL_1 and BL_2 [Figs. 5.3(b)]. In the fitting procedure, the STH peak is first fitted on the high-energy side at 3.40 eV using the peak position and FWHM consistent with the isolated STH emission in β-Ga_2O_3 [36]. The low-energy side of the luminescence spectrum is then fitted with two broad defect-related Gaussian peaks (BL_1 and BL_2) centred at 3.14 eV and 2.93 eV, respectively, each with an FWHM of approximately 0.64 eV. These values are consistent with previously reported CL data for β-Ga_2O_3 single crystals [34]. The two blue bands (BL_1 and BL_2) have been attributed to DAP radiative recombination channels involving deep V_O donors and deep acceptors, such as isolated V_{Ga} and V_O-V_{Ga} defect pairs [15, 16]. The relative intensity ratios of the three deconvoluted peaks are found to be BL_1/UV=0.72 and BL_2/UV=0.34. Notably, the luminescence intensity decreases by a factor of 3 after F doping, as shown in Figure 5.7. This quenching effect is likely attributed to changes in the surface recombination velocity in F-doped Ga_2O_3, which may alter the recombination dynamics and reduce radiative emission efficiency.

For the F:Ga_2O_3 NWs, similar deconvolution shows three similar deconvoluted Gaussian peaks, plus an additional high-energy UV peak (UV^+) at 3.64 eV. This UV^+ emission is consistent with DAP recombination involving F shallow donors and deep acceptors [37], as revealed by the XPS results showing the formation of substitutional F_O dopants post-doping. Indeed, the relative intensity ratios of BL_1/UV and BL_2/UV peaks in F:Ga_2O_3 NW decrease to 0.42 and 0.20, respectively, indicating a significant reduction in defect-related emission. This reduction indicates the passivation of native defects, such as V_O, after fluorine incorporation, which have been observed in previous studies [24, 28]. The passivation of V_O defects by F is significant as it may reduce background n-type conductivity associated with V_O-related donors as previously reported [38]. Figure 5.3(d) summarizes the CL emission pathways for Ga_2O_3 and F:Ga_2O_3 NWs. For undoped NWs, the emission channels include the radiative recombination through the STH state (UV band) and DAP transitions (BL_1 and BL_2 bands). A similar recombination model is applicable to F-doped NWs, with the addition of the UV^+ transition arising from shallow donor – deep acceptor DAP recombination involving F donors. Neither undoped nor F-doped NWs exhibit an NBE emission, indicating the absence of minority free holes in the VB, in agreement with the rapid self-trapping of holes in b-Ga_2O_3.

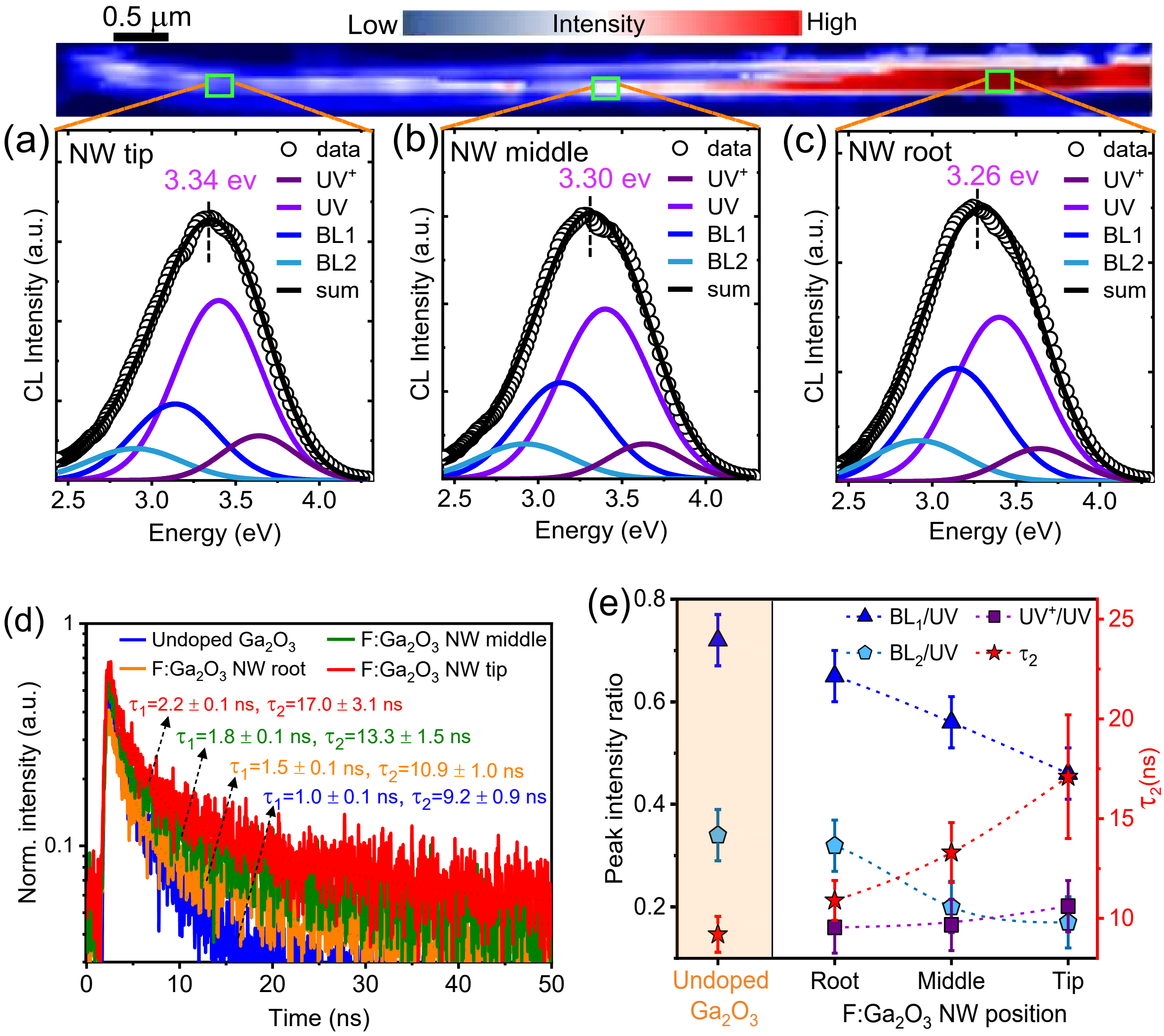

Figure 5.4. (a, b, c) CL spectra of a single F:Ga_2O_3 NW acquired from an 100 × 100 nm area at the tip, middle and root regions, based on the hyperspectral CL map of the NW displayed

above. (d) Corresponding TR-CL decay curves with the dashed lines representing bi-exponential decay fits. For the undoped NW, the decay times are τ_1 = 1.0 ± 0.1 ns and τ_2 = 9.2 ± 0.9 ns. After F doping, both decay times increase significantly, with τ_1 = 2.2 ± 0.1 ns and τ_2 = 17.0 ± 3.1 ns at the F:Ga_2O_3 NW tip. (e) Relative intensities of the defect-related BL and F-related UV$^+$ emissions compared to the intrinsic UV emission for undoped b-Ga_2O_3, and along the F:Ga_2O_3 NW length. The results reveal an anti-correlation between the defect emissions and UV$^+$ emission from the root to the tip of the F:Ga_2O_3 NW.

The influence of F doping on Ga_2O_3 is further investigated by hyperspectral CL mapping of individual NWs with a pixel size of 50 × 50 nm. In Fig 5.4 (a-c), CL spectra from three different regions along the NW, i.e. root, middle, and tip, averaged over an area of 100 × 100 nm for each region are selected to illustrate spectral changes within a single NW. A gradual reduction in BL_1 and BL_2 emissions, coupled with an increase in the UV$^+$ emission, is observed from the root to the tip, indicating a gradient in F doping concentration along the NW length. Notably, the CL peak gradually shifts from 3.34 eV at the tip to 3.26 eV at the root of the NW, indicating a suppression of defect-related emissions and the emergence of UV$^+$ emission associated with the higher F concentration in the tip region. This observation aligns with the variation in the relative intensity ratio between the F Kα and Ga Lα X-ray peaks (Figure 5.5), which demonstrates an increased fluorine concentration at the NW tip compared to the middle and root. It is also noteworthy that the overall CL emission intensity is higher at the NW root and gradually decreases along its length, as shown in the hyperspectral CL map in Fig. 5.4. This reduction in intensity reflects an increased density of non-radiative defects formed during the NW growth.

The impact of F doping on the carrier dynamics is further investigated using TR-CL measurements, as depicted in Fig. 5.4 (d). The CL emission decay curves are fitted using a bi-exponential function, represented by the dashed lines, defined as $I(t) = I_o + I_1 \exp\left(\frac{-t}{\tau_1}\right) + I_2 \exp\left(\frac{-t}{\tau_2}\right)$, where τ_1 and τ_1 are decay time constants, I_1 and I_2 represent the intensities of the decay components, and I_o denotes the background signal. The fast decay component τ_1, typically between 1 and 3 ns, is commonly observed in various Ga_2O_3 materials and has been attributed to surface recombination of carriers [39, 40]. The F doping is found to extend the charge carrier lifetime, affecting both the fast and slow decay components. For undoped NWs, the fast decay component has τ_1= 1.0 $\pm$ 0.1 ns, which increases to τ_1= 2.2 $\pm$ 0.1 ns at the NW tip where the F doping concentration is highest. The increase in τ_1 could be due to additional surface defects introduced by plasma treatment. Notably, the slow decay component, associated with the delayed recombination of carriers via STHs and defects, is extended from τ_2 = 9.2 $\pm$ 0.9 ns for undoped NWs to τ_2 = 17.0 $\pm$ 3.1 ns at the F-doped NW tip. These measurements suggest that the extended τ_2 component results from carrier recombination through the F donor state [Fig. 5.3(d)], which is competitive with and slower than the STH recombination channel [41]. Furthermore, the τ_2 lifetime decrease in the lower regions (middle and root) of the F-doped NW, correlating with a reduced number of donor states due to the lower F doping concentration. Fig. 5.4 (e) summarizes the relative intensities of defect-related and F-related emissions for Ga_2O_3 NW and along the F:Ga_2O_3 NW. The UV^+/UV ratio shows a slight increase from root to tip, consistent with a higher F concentration at the NW tip, which aligns with the expected dopant profile for plasma doping processes [42]. In contrast, both the BL_1/UV and BL_2/UV intensity ratios gradually decrease from 0.65 and 0.32 at the root to 0.46 and 0.17 at the tip, correlating with a decreasing F doping concentration. This indicates effective passivation of native defects by F ions during the remote plasma treatment. The higher F concentration towards the NW tip also results in extended carrier lifetimes, with the decay lifetime increasing from 10.9 $\pm$ 1.0 ns at the root to 17.0 ± 3.1 ns at the tip. These TR-CL findings highlight the effectiveness of SF_6 plasma processing in both passivating native defects and incorporating F shallow donors in Ga_2O_3, offering insights into the tunability of luminescence and carrier dynamics through F doping.

5.4. Conclusions

Ga_2O_3 NWs can be successfully doped with fluorine shallow donors using SF_6 remote plasma treatment. Fluorine is found to be incorporated along the entire length of the NWs, without any detectable sulfur contamination. Importantly, the NWs retain their monoclinic structure without deteriorating crystal quality after the plasma treatment, exhibiting the characteristic self-trapped hole emission. Photoemission spectroscopy reveals the formation of Ga–F bonds, accompanied by strong adsorption of –OH groups on the NW surface. The incorporation of fluorine effectively passivates native defects, as indicated by a marked reduction in defect-related luminescence. Moreover, a new UV emission band, located at 0.2 eV above the self-trapped hole emission, emerges post-treatment and is attributed to donor-acceptor-pair recombination involving F shallow donors and deep defect-related acceptors. This newly formed recombination channel leads to a significant increase in carrier lifetime, extending from 9.2 ± 0.9 ns in undoped Ga_2O_3 to 17.0 ± 3.1 ns in highly F-doped nanowires. These findings highlight the important role of F doping in modulating carrier dynamics and enhancing UV emission in β-Ga_2O_3, offering new insights for direct environmental application such as deep UV photodetector and gas sensors.

CRediT authorship contribution statement

Amar K. Salih: Methodology, Investigation, Formal analysis, Writing –original draft. Saskia Fiedler: Methodology, Investigation, Formal analysis. Curtis Irvine: Methodology, Investigation. Fatima Matar: Investigation, Validation. Matthew R. Phillips: Conceptualization, Writing – review & editing. Cuong Ton-That: Conceptualization, Methodology, Writing – review & editing.

Supplementary data

Supplementary data to this paper is available in the appendix: D

Acknowledgements

This research was partly conducted on the Soft X-ray Spectroscopy beamline at the Australian Synchrotron, Victoria, Australia. The work was supported by the Australian Research Council (ARC) Discovery Project funding scheme (Project DP210101146). The authors wish to thank Bruce Cowie, Anton Tadich, James Bishop and Herbert Yuan for their technical support.

5.5. References

[1] D. Guo, Q. Guo, Z. Chen, Z. Wu, P. Li, W. Tang, Review of Ga_2O_3-based optoelectronic devices, Materials Today Physics, 11 (2019) 100157.

[2] S. Pearton, J. Yang, P.H. Cary, F. Ren, J. Kim, M.J. Tadjer, M.A. Mastro, A review of Ga_2O_3 materials, processing, and devices, Applied Physics Reviews, 5 (2018).

[3] D. Kaur, S. Debata, D.P. Singh, M. Kumar, Strain effects on the optoelectronic performance of ultra-wide band gap polycrystalline β-Ga_2O_3 thin film grown on differently-oriented Silicon substrates for solar blind photodetector, Applied Surface Science, 616 (2023) 156446.

[4] J.B. Varley, J.R. Weber, A. Janotti, C.G. Van de Walle, Oxygen vacancies and donor impurities in β-Ga_2O_3, Applied physics letters, 97 (2010).

[5] M.D. McCluskey, Point defects in Ga_2O_3, Journal of Applied Physics, 127 (2020).

[6] A. Kyrtsos, M. Matsubara, E. Bellotti, Migration mechanisms and diffusion barriers of vacancies in Ga_2O_3, Physical Review B, 95 (2017) 245202.

[7] A.T. Neal, S. Mou, S. Rafique, H. Zhao, E. Ahmadi, J.S. Speck, K.T. Stevens, J.D. Blevins, D.B. Thomson, N. Moser, Donors and deep acceptors in β-Ga_2O_3, Applied Physics Letters, 113 (2018).

[8] S. Kim, H.-Y. Kim, Y. Kim, D.-W. Jeon, W.S. Hwang, J.-H. Park, High-performance normally-off Si-doped β-Ga_2O_3 deep ultraviolet phototransistor grown on N-doped β-Ga_2O_3, Applied Surface Science, 679 (2025) 161165.

[9] J. Yang, C. Fares, F. Ren, R. Sharma, E. Patrick, M.E. Law, S. Pearton, A. Kuramata, Effects of fluorine incorporation into β-Ga_2O_3, Journal of Applied Physics, 123 (2018).

[10] M.J. Tadjer, J.L. Lyons, N. Nepal, J.A. Freitas, A.D. Koehler, G.M. Foster, Review—Theory and characterization of doping and defects in β-Ga_2O_3, ECS Journal of Solid State Science and Technology, 8 (2019) Q3187-Q3194.

[11] R. Sharma, M.E. Law, F. Ren, A.Y. Polyakov, S.J. Pearton, Diffusion of dopants and impurities in β-Ga_2O_3, Journal of Vacuum Science & Technology A, 39 (2021).

[12] Y.J. Jeong, J.Y. Yang, C.H. Lee, R. Park, G. Lee, R.B.K. Chung, G. Yoo, Fluorine-based plasma treatment for hetero-epitaxial β-Ga_2O_3 MOSFETs, Applied Surface Science, 558 (2021) 149936.

[13] J. Yan, C. Qu, Electronic structure and optical properties of F-doped β-Ga_2O_3 from first principles calculations, Journal of Semiconductors, 37 (2016) 042002.

[14] H. Gao, S. Muralidharan, N. Pronin, M.R. Karim, S.M. White, T. Asel, G. Foster, S. Krishnamoorthy, S. Rajan, L.R. Cao, Optical signatures of deep level defects in Ga_2O_3, Applied Physics Letters, 112 (2018).

[15] T. Huynh, L. Lem, A. Kuramata, M. Phillips, C. Ton-That, Kinetics of charge carrier recombination in β-Ga_2O_3 crystals, Physical Review Materials, 2 (2018) 105203.

[16] T. Onuma, S. Fujioka, T. Yamaguchi, M. Higashiwaki, K. Sasaki, T. Masui, T. Honda, Correlation between blue luminescence intensity and resistivity in β-Ga_2O_3 single crystals, Applied Physics Letters, 103 (2013).

[17] T.T. Huynh, E. Chikoidze, C.P. Irvine, M. Zakria, Y. Dumont, F.H. Teherani, E.V. Sandana, P. Bove, D.J. Rogers, M.R. Phillips, C. Ton-That, Red luminescence in H-doped β-Ga_2O_3, Physical Review Materials, 4 (2020) 085201.

[18] S. Marcinkevičius, J.S. Speck, Ultrafast dynamics of hole self-localization in β-Ga_2O_3, Applied Physics Letters, 116 (2020).

[19] J.B. Varley, A. Janotti, C. Franchini, C.G. Van de Walle, Role of self-trapping in luminescence and p-type conductivity of wide-band-gap oxides, Physical Review B, 85 (2012) 081109.

[20] S. Meuret, M.S. Garcia, T. Coenen, E. Kieft, H. Zeijlemaker, M. Lätzel, S. Christiansen, S. Woo, Y. Ra, Z. Mi, Complementary cathodoluminescence lifetime imaging configurations in a scanning electron microscope, Ultramicroscopy, 197 (2019) 28-38.

[21] J. Du, J. Xing, C. Ge, H. Liu, P. Liu, H. Hao, J. Dong, Z. Zheng, H. Gao, Highly sensitive and ultrafast deep UV photodetector based on a β-Ga_2O_3 nanowire network grown by CVD, Journal of Physics D: Applied Physics, 49 (2016) 425105.

[22] H. Liang, Y. Chen, X. Xia, C. Zhang, R. Shen, Y. Liu, Y. Luo, G. Du, A preliminary study of SF_6 based inductively coupled plasma etching techniques for beta gallium trioxide thin film, Materials Science in Semiconductor Processing, 39 (2015) 582-586.

[23] W.-K. Wang, S.Y. Wang, Y.H. Zhang, S.-Y. Huang, Passivation effect on the surface characteristics and corrosion properties of yttrium oxide films undergoing SF_6 plasma treatment, Ceramics International, 48 (2022) 19824-19830.

[24] Y. Xu, B. Bo, X. Gao, Z. Qiao, Passivation effect on ZnO films by SF_6 plasma treatment, Crystals, 9 (2019) 236.

[25] M. Kumar, V. Kumar, R. Singh, Diameter tuning of β-Ga_2O_3 nanowires using chemical vapor deposition technique, Nanoscale Research Letters, 12 (2017) 184.

[26] J. Yang, W. Zhou, J. Hu, R. Jiang, G. Sun, J. Zhao, F. Wang, F. Fang, Y. Song, D. Sun, Universal Renaissance Strategy of Metal Fluoride in Secondary Ion Batteries Enabled by Liquid Metal Gallium, Advanced Materials, 35 (2023) 2301442.

[27] C.-C. Wang, B.-C. Lee, F.-S. Shieu, H.C. Shih, Characterization and photoluminescence of Sn-doped β-Ga_2O_3 nanowires formed by thermal evaporation, Chemical Physics Letters, 753 (2020) 137624.

[28] E. Polydorou, A. Zeniou, D. Tsikritzis, A. Soultati, I. Sakellis, S. Gardelis, T.A. Papadopoulos, J. Briscoe, L.C. Palilis, S. Kennou, Surface passivation effect by fluorine plasma treatment on ZnO for efficiency and lifetime improvement of inverted polymer solar cells, Journal of Materials Chemistry A, 4 (2016) 11844-11858.

[29] B. Liu, M. Gu, X. Liu, S. Huang, C. Ni, First-principles study of fluorine-doped zinc oxide, Applied Physics Letters, 97 (2010).

[30] W. Yu, J.G. Lee, Y.-H. Joo, B. Hou, D.-S. Um, C.-I. Kim, Etching characteristics and surface properties of fluorine-doped tin oxide thin films under CF_4-based plasma treatment, Applied Physics A, 128 (2022) 942.

[31] M. Grodzicki, Properties of bare and thin-film-covered gan (0001) surfaces, Coatings, 11 (2021) 145.

[32] S. Tanuma, C.J. Powell, D.R. Penn, Calculations of electron inelastic mean free paths. V. Data for 14 organic compounds over the 50–2000 eV range, Surface and interface analysis, 21 (1994) 165-176.

[33] C. Han, L. Mazzarella, Y. Zhao, G. Yang, P. Procel, M. Tijssen, A. Montes, L. Spitaleri, A. Gulino, X. Zhang, High-mobility hydrogenated fluorine-doped indium oxide film for passivating contacts c-Si solar cells, ACS applied materials & interfaces, 11 (2019) 45586-45595.

[34] C.P. Irvine, A. Stopic, M.T. Westerhausen, M.R. Phillips, C. Ton-That, Enhancement of excitonic and defect-related luminescence in neutron transmutation doped β-Ga_2O_3, Physical Review Materials, 6 (2022) 114603.

[35] K. Yamamura, L. Zhu, C.P. Irvine, J.A. Scott, M. Singh, A. Jallandhra, V. Bansal, M.R. Phillips, C. Ton-That, Defect Compensation in Nitrogen-Doped β-Ga_2O_3 Nanowires: Implications for Bipolar Nanoscale Devices, ACS Applied Nano Materials, 5 (2022) 12087-12094.

[36] S. Yamaoka, Y. Furukawa, M. Nakayama, Initial process of photoluminescence dynamics of self-trapped excitons in a β-Ga_2O_3 single crystal, Physical Review B, 95 (2017) 094304.

[37] T. Onuma, Y. Nakata, K. Sasaki, T. Masui, T. Yamaguchi, T. Honda, A. Kuramata, S. Yamakoshi, M. Higashiwaki, Modeling and interpretation of UV and blue luminescence intensity in β-Ga_2O_3 by silicon and nitrogen doping, Journal of Applied Physics, 124 (2018).

[38] S. Morimoto, H. Nishinaka, M. Yoshimoto, Growth and characterization of F-doped α-Ga_2O_3 thin films with low electrical resistivity, Thin Solid Films, 682 (2019) 18-23.

[39] D. Kaur, P. Vashishtha, G. Gupta, S. Sarkar, M. Kumar, Surface nanopatterning of amorphous gallium oxide thin film for enhanced solar-blind photodetection, Nanotechnology, 33 (2022) 375302.

[40] U. Varshney, A. Sharma, P. Vashishtha, L. Goswami, G. Gupta, Ga_2O_3/GaN heterointerface-based self-driven broad-band ultraviolet photodetectors with high responsivity, ACS Applied Electronic Materials, 4 (2022) 5641-5651.

[41] A. Othonos, M. Zervos, C. Christofides, Carrier dynamics in β-Ga_2O_3 nanowires, Journal of Applied Physics, 108 (2010).

[42] Z. Hu, Y. Lv, C. Zhao, Q. Feng, Z. Feng, K. Dang, X. Tian, Y. Zhang, J. Ning, H. Zhou, Beveled Fluoride Plasma Treatment for Vertical β-Ga_2O_3 Schottky Barrier Diode With High Reverse Blocking Voltage and Low Turn-On Voltage, IEEE Electron Device Letters, 41 (2020) 441-444.

5.6. Appendix D: Additional surface chemistry and cathodoluminescence data

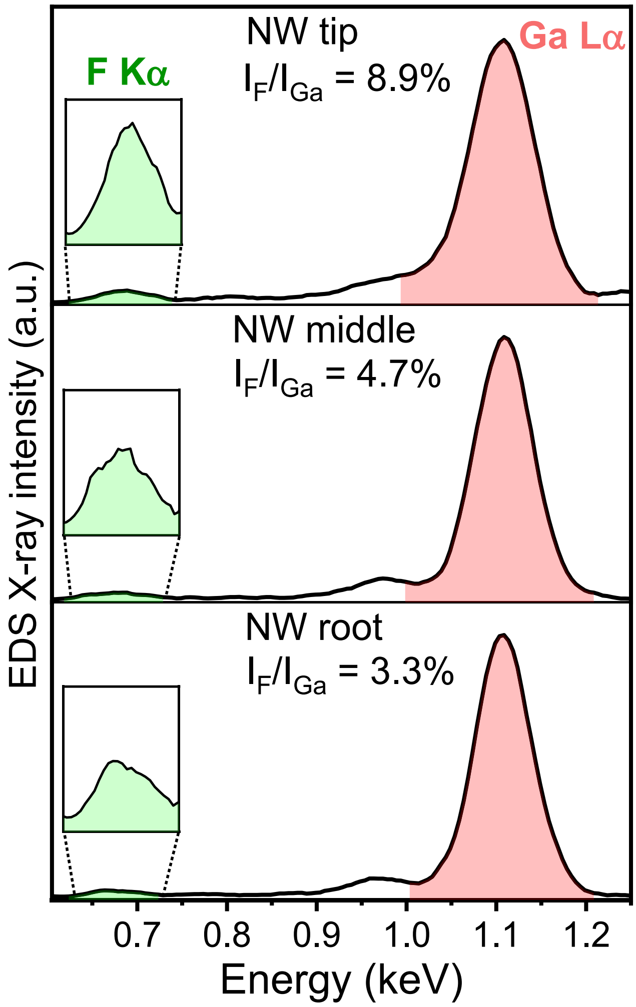

Figure 6.5. EDS spectra of a F:Ga_2O_3 NW reveal a variation in the relative intensity ratio between the F Kα and Ga Lα X-ray peaks along the NW length. The intensity ratio (I_F/I_{Ga}) increases from the root ($I_{F(root)}/I_{Ga(root)}$ = 3.3%) to the middle ($I_{F(middle)}/I_{Ga(middle)}$ = 4.7%) and the tip ($I_{F(tip)}/I_{Ga(tip)}$ = 8.9%). This indicates that the fluorine concentration is highest at the tip, followed by the middle, and lowest at the root of the NW.

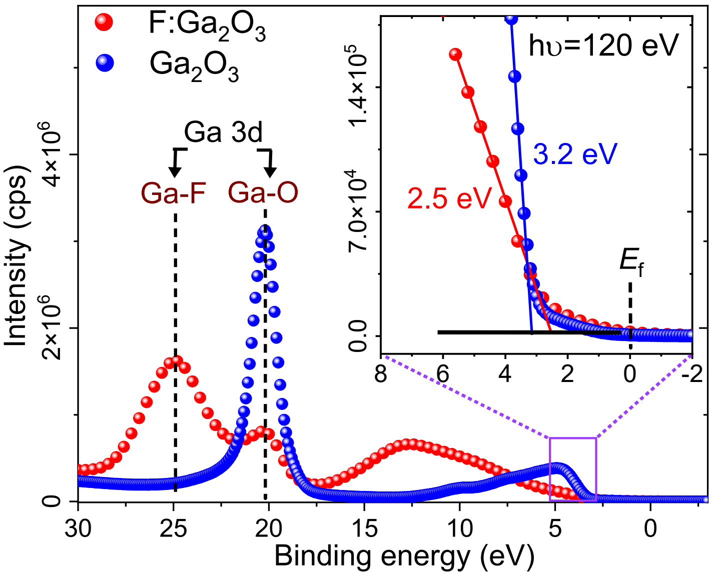

Figure 6.6. Surface-sensitive photoelectron spectroscopy analysis of Ga_2O_3 and F:Ga_2O_3 NWs using a photon energy of hν = 120 eV. The spectra reveals a shift in the VB edge from 3.2 eV in undoped Ga_2O_3 to 2.5 eV in F:Ga_2O_3, attributed to the incorporation of fluorine, which introduces shallow F_O donors. Additionally, a new peak emerges at 24.8 eV in the F:Ga_2O_3 NWs, likely due to the the hybridization of Ga 3*d* and F 2*s* surface states.

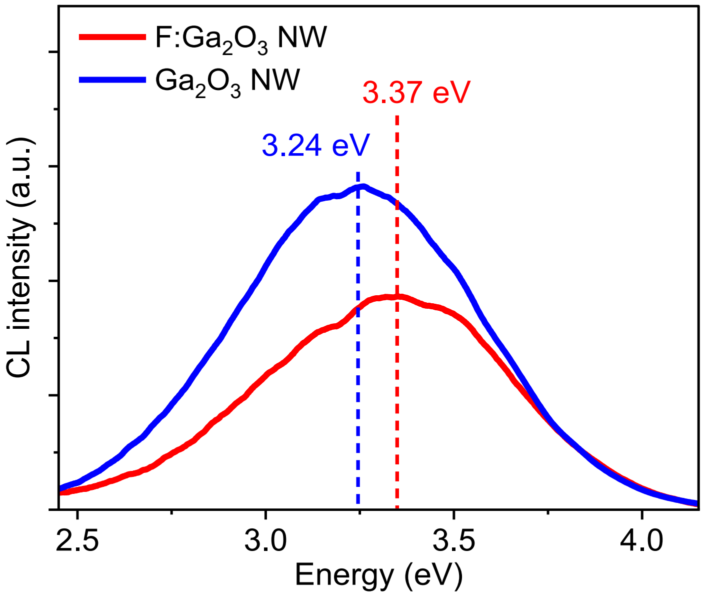

Figure 6.7. CL spectra of Ga_2O_3 and F:Ga_2O_3 NWs acquired under identical excitation conditions (5 kV, 85 pA). The F doping induces a blue shift of 0.13 eV in the luminescence spectrum, along with significant luminescence quenching.

Chapter 6. Conclusions

6.1. Summary

This thesis investigates the synthesis, modification, and application of metal oxide nanostructures, emphasizing their potential in advancing sustainable environmental technologies.

Firstly, this thesis demonstrates the development of ZnO-coated membranes tailored for efficient microalgae harvesting from pre-concentrated solutions. ZnO thin films were successfully deposited onto two types of porous substrates: stainless-steel and alumina membranes. These coatings significantly enhanced membrane hydrophilicity and filtration performance, albeit with notable differences in performance characteristics between the two substrates. Stainless-steel membranes exhibited promising results, demonstrating a two-fold improvement in clean water flux compared to their uncoated counterparts. However, after fouling, these membranes showed a flux decline with only 60% permeate flux recovery achievable following 30 minutes of UV exposure. In contrast, ZnO-coated alumina membranes demonstrated a substantial 50% increase in hydrophilicity, which effectively limited flux decline to a just 5% over three filtration cycles. Additionally, the alumina membranes achieved complete (100%) flux recovery after just 30 minutes of solar irradiation, clearly outperforming the SST membranes.

Secondly, this thesis also introduces a facile and cost-effective method for fabricating ZnO photoanodes enriched with oxygen vacancies (V_O). This innovative approach involves post-growth oxidation of metallic Zn films, producing randomly oriented ZnO nanorods with exceptional light absorption and charge transfer properties. These photoanodes achieve a remarkable photocurrent density of 1.14 mA/cm^2 at 1.23 V_{RHE} without doping or surface modification with other metals or metal oxides.

Lastly, this study investigates the effect of SF_6 plasma treatment in the electronic properties of β-Ga_2O_3 nanowires. It was found that SF_6 plasma treatment enables a uniform incorporation of fluorine onto β-Ga_2O_3 nanowires without sulfur contamination, preserving its monoclinic crystal structure and quality. In addition, the SF_6 plasma treatment passivates native defects in β-Ga_2O_3, reducing defect-related luminescence, and introduces a new UV emission band attributed to donor-acceptor-pair recombination. This process enhances carrier dynamics by increasing the carrier lifetime from 9.2 ± 0.9 ns to 17.0 ± 3.1 ns.

In conclusion, this thesis establishes a solid foundation for the use of ZnO and β-Ga_2O_3 nanostructures in addressing critical environmental challenges, including hydrogen evolution, photocatalytic degradation and its application in biomass harvesting for green fuel production, and enhancing the electronic properties of optoelectronic devices for environmental applications.

6.2. Future Work

Building upon the findings of this thesis, several avenues for future research are proposed:

Firstly, coating stainless steel membranes with ZnO thin films significantly enhances filtration performance; however, the observed 60% permeate recovery rate remains insufficient for efficient industrial applications. This limitation is primarily attributed to the large pore size of the membrane. To overcome this issue, employing stainless steel membranes with smaller pore sizes could help reduce internal fouling. Additionally, incorporating a backwashing step into the cleaning protocol is recommended to further improve the recovery rate, potentially approaching 100%. Furthermore, ZnO-coated alumina membranes demonstrated excellent filtration performance and complete permeate flux recovery when tested with *Scenedesmus sp.* microalgae. However, further evaluation using a broader range of microalgae species is recommended to confirm the general applicability of this approach. Long-term fouling assessments and a detailed cost analysis are also advised to better understand the economic feasibility of these membrane systems.

We also recommend conducting a comprehensive analysis of the degradation products of the algae and potential oxidation by-products to assess any environmental or health risks associated with this membrane system. Future studies could explore the use of sputtering deposition with alternative materials with lower health risks, such as titanium dioxide, and assess their stability relative to ZnO-based membranes developed in this thesis.

Secondly, although the fabricated ZnO photoanode exhibits a promising photocurrent density of 1.14 mA/cm^2 at 1.23 V_{RHE}, further modifications are necessary to enhance its photocatalytic performance for industrial-scale applications. This could be achieved by constructing heterostructures with other metal oxides, such as $ZnFe_2O_4$ or $BiVO_4$, to improve light absorption and charge separation. The integration of electrocatalysts such as Co–Pi is also recommended to enhance charge transfer efficiency and reduce the required bias potential. In addition, further evaluation through long-term stability testing, quantum efficiency measurements, and quantification of H_2 and O_2 production is essential to fully assess the practical viability of the photoanode.

Finally, the incorporation of fluorine into β-Ga_2O_3 NWs significantly enhances their optical properties by compensating for native defects. However, further investigation is needed to measure their electrical properties and assess optoelectronic device performance. Utilizing precise nanowire fabrication techniques, such as Molecular Beam Epitaxy (MBE), could enable the production of high-quality nanowires with suitable electrical contacts for these measurements and facilitate device fabrication.